Die approbierte Originalversion dieser Dissertation ist an der Hauptbibliothek der Technischen Universität Wien aufgestellt (http://www.ub.tuwien.ac.at).

The approved original version of this thesis is available at the main library of the Vienna University of Technology (http://www.ub.tuwien.ac.at/englweb/).

DISSERTATION

SIMULATION OF STRUCTURE AND MAGNETIC PROPERTIES OF NANOCLUSTERS

ausgeführt zum Zwecke der Erlangung des akademischen Grades
eines Doktors der technischen Wissenschaften

unter der Leitung von
Prof. Dr. Thomas Schrefl
Institut für Festkörperphysik E138

eingereicht an der Technischen Universität Wien
Fakultät für Physik

von

Florian Dorfbauer
Mat. Nr: 9855700
Gentzgasse 72/2/14
1180 Wien

Wien, am 25. Oktober 2006 ....

Kurzfassung

In dieser Arbeit wird ein Simulationsprogramm entwickelt, das basierend auf der Theorie der Molekulardynamik die Bildung von magnetischen Nanoclustern beschreibt. Da Metalle nicht durch einen einfachen Paarpotential-Ansatz beschrieben werden können, wird die Embedded-Atom-Methode verwendet, um den spezifischen Eigenschaften der zu untersuchenden Materialien Rechnung zu tragen. Zusammen mit einem Legierungsmodell von Johnson ermöglicht die Embedded-Atom-Methode Untersuchungen an Systemen, die aus verschiedensten Materialien zusammengesetzt sind. In der Simulation wird die Temperatur durch ein Nosé-Hoover Thermostat kontrolliert. Um das entwickelte Simulationswerkzeug zu testen, werden Kenngrößen wie beispielsweise die Gleichgewichtsgitterkonstante oder der thermische Ausdehnungskoeffizient für verschiedenste publizierte Potentiale berechnet. Weiters wird eine experimentell bestätigte Schalen-Kern-Formation simuliert. Die Berechnung des Anlassvorgangs ergibt eine klar definierte Segregation der Ag-Atome an die Oberfläche. Die Kristallebenen des Kerns weisen keine einheitliche Stapelfolge auf. Um die Kristallstruktur des Kerns zu bestimmen, wird ein automatisches Analysewerkzeug entwickelt. Unter den verwendeten Systemparametern weisen CoAg Kern-Schalen Formationen eine Mischung aus hexagonal dichtester Packung und flächenzentriert kubischer Struktur auf.

Verglichen mit den magnetischen Eigenschaften eines Festkörpers zeigen Nanopartikel signifikante Unterschiede. Das Verhältnis zwischen Atomen an der Oberfläche und im Inneren dieser Partikel beeinflußt die magnetischen Eigenschaften maßgeblich. Zusätzlich bestimmt die Morphologie der Partikel die effektive magnetokristalline Anisotropie. Die Facetierung von Partikeln, welche aus wenigen tausend Atomen bestehen, hängt von der Systemgröße ab und hat ihre direkte Ursache in der Minimierung der Oberflächenenergie. Diese Eigenschaft magnetischer Cluster wird in einem magnetischen Modell berücksichtigt. Eine langreichweitige Formulierung der Austauschenergie beschreibt die Abweichung der Austauschenergie von Atomen nahe der Oberfläche. Oberflächenatome besitzen weniger Nachbarn als Nichtoberflächenatome, deshalb weisen oberflächennahe Atome eine geringere Austauschenergie auf. Für die magnetokristalline Anisotropie von Oberflächenatomen und Nichtoberflächenatomen werden verschiedene Modelle verwendet. Die magnetokristalline Anisotropie von Nichtoberflächenatomen wird durch lokale Anisotropieachsen beschrieben. Diese Anisotropierichtungen sind von den Fluktuation der Nachbaratome abhängig. Der Einfluss der thermischen Fluktuationen aufgrund der Bewegungen der Atome wird untersucht. Die spezifische Formulierung des phononenabhängigen magnetischen Modells führt auf ein implizit gekoppeltes Phononen-Magnonen-System. Eine Berücksichtigung der zusätzlichen Fluktuationen aufgrund der variierenden Atompositionen bewirkt nur eine geringe Änderung der magnetischen Eigenschaften. Im Gegensatz dazu führt die Verwendung einer langreichweitigen Formulierung der Austauschenergie auf ein Koerzitivfeld, das um 20% kleiner ist als bei einem vergleichbaren Modell mit kurzreichweitiger Austauschenergieformulierung.

Abstract

The formation of magnetic nanoclusters is simulated using molecular dynamics simulations. In general, metals can not be described by a simple pair potential approach. Therefore, the embedded atom method is used to account for the specific properties of the investigated materials. In combination with an alloy model proposed by Johnson, the embedded atom method allows for investigations with multiple substituents making it a feasible tool to explore crystalline formations in magnetic materials. The temperature is adjusted and controlled by a Nosé-Hoover thermostat. To test the developed simulation tool, bulk material properties such as the equilibrium lattice constant or the thermal expansion coefficient are determined for different published potentials. Furthermore, the experimentally approved core-shell formation of CoAg is simulated. The calculation of the annealing process yields a clear segregation of the Ag atoms towards the surface. The crystal planes of the core do not show a unique stacking order. To investigate the layering of the core, an automated analysis tool is employed. CoAg core-shell formations exhibit an intermixture between hexagonal closed packed fractions and a face centered cubic structure in the considered parameter range.

Magnetically, nanoparticles behave differently as compared to bulk materials. The high surface-to-volume ratio of nanoclusters influences the magnetic properties drastically. Additionally, the morphology of a nanocluster influences the effective magnetocrystalline anisotropy. The facets of aggregates consisting of a few thousand atoms depend on the systems size and is a direct consequence of the surface energy minimization. A magnetic model is introduced to account for the peculiarities of nanoclusters. A long-range formulation of the exchange energy accounts for deviations in the exchange energy appearing for atoms close to the surface. Surface atoms exhibit less neighbors than non-surface atoms, leading to lower exchange energies. Therefore, the magnetocrystalline anisotropy is modeled differently for surface atoms and non-surface atoms. The magnetocrystalline anisotropy of non-surface atoms is described by using local anisotropy axes depending on the fluctuations of the neighboring atoms. Subsequently, thermal fluctuations arising from the motion of the atoms in the magnetic system are explored. The specific formulation of the phonon dependent magnetic model leads to an implicitly coupled phonon-magnon system. The additional fluctuations arising from the varying positions of the atoms do not significantly change the magnetic behavior. In contrast, using a long-range exchange formulation yields a coercive field 20% smaller as compared to a standard next neighbor exchange model.

Acknowledgement

Whenever I read a thesis, I read the acknowledgement first. It is the only page, that allows the author to write not only in a scientific way but to express gratefulness to people who accompanied her or him during the work, which is definitely more important than any figure or equation.

First of all I want to thank my supervisor Thomas Schrefl. His affable attitude and his motivating calls were always a help while working on this thesis. At the Royal Melbourne Institute of Technology, Ian Snook, Salvy Russo and Greg Grochola taught me how to play around with crowds of metallic atoms in an effective and helpful way. Ryan and Istvan introduced me to the more substantial things, such as Australian football rules. It was also a pleasure to work on magnetic nanoparticles with Roy Chantrell and Richard Evans from the University of York.

A very special Thank You! goes to Markus Kirschner. His knowledge in atomistic modeling was very constructive. He also found time to proof-read the manuscript. Franz Wenzl, Regina Blauensteiner and Dieter Suess also struggled through the manuscript and provided helpful comments.

Bedanken möchte ich mich auch bei meinen Eltern, die mir die Freiheit schenkten, mein Leben selbst zu gestalten.

This thesis was supported by the Austrian Science Fund (project number FWF Y132-N02).

CONTENTS

KURZFASSUNG 2
ABSTRACT 3
ACKNOWLEDGEMENT 4

CONTENTS 5

1 INTRODUCTION 8
1.1 Motivation 8

2 MOLECULAR DYNAMICS 10
2.1 Introduction 10
2.2 Mathematical Formulation 11
  2.2.1 Hamiltonian Mechanics in a Nutshell 12
  2.2.2 Thermodynamic Quantities in Simple Simulations 13
  2.2.3 Integration Methods 15
  2.2.4 Extended Hamiltonians 18
2.3 Potentials 22
  2.3.1 Lennard-Jones Potentials 23
  2.3.2 Embedded Atom Method 24
2.4 Selected Numerical Aspects and Data Structures 26
  2.4.1 Integration of Closed Loops 26
  2.4.2 Cut-off Radius and Representation of the Simulation 27
  2.4.3 Comparison Between Tabulated Potentials and Analytical Functions 29

3 EVALUATION OF DIFFERENT POTENTIALS: CALCULATION OF BULK PROPERTIES 31
3.1 Introduction 31
  3.1.1 The Original Potentials of Daw and Baskes 31
  3.1.2 Embedding Atom Potentials by Zhou et al. 32
  3.1.3 Modeling Alloys with the Embedded Atom Method 34
  3.1.4 Conclusion 37
3.2 Calculation of Bulk Properties 37
  3.2.1 Equilibrium Lattice Constant a_0 38
  3.2.2 Thermal Expansion Coefficient α 41
  3.2.3 Bulk Modulus B_0 42
  3.2.4 Sublimation Energy E_s 45
  3.2.5 Heat Capacity C_P 45
  3.2.6 Equilibrium Properties of FePt 46
3.3 Conclusion 49

4 STRUCTURE SIMULATION OF MAGNETIC NANOCLUSTERS 50
4.1 Introduction 50
4.2 Simulation Method 52
4.3 Analyzing Methods 53
  4.3.1 Radial Distribution Function 53
  4.3.2 Tesselation Method 54
4.4 The CoAg Core-Shell System 56
  4.4.1 Experimental Results 56
  4.4.2 Simulation of a Core-Shell Formation 56
  4.4.3 Results and Discussion 57
4.5 Summary and Outlook 62

5 MAGNETIC PROPERTIES OF NANOCLUSTERS 63
5.1 Introduction 63
5.2 Basics of Magnetism 64
  5.2.1 Energy Contributions in a Magnetic System 66
  5.2.2 Thermal Effects 71
  5.2.3 Integration Method 72
5.3 The Model System 73
5.4 Surface Anisotropy in Nanoclusters 75
  5.4.1 A First Test 75
  5.4.2 Surface Anisotropy and Saturation Polarization J_s 77
  5.4.3 Anisotropy in Nanoclusters and its Impact on the Coercive Field $\boldsymbol{H}_c$ 79
5.5 Influence of Long-Range Exchange on $\boldsymbol{H}_c$ 81
5.6 Thermal Effects 83
5.7 Summary and Outlook 85

6 APPENDIX 86
6.1 Scaling Properties and Reducing Units 86
  6.1.1 Physical Constants 86
  6.1.2 Scaling Equations for Molecular Dynamics Calculations 87
  6.1.3 Scaling of the Landau-Lifshitz-Gilbert Equation 89
6.2 Potential Parameters 89
  6.2.1 The Original Approach 90
  6.2.2 Zhou Potential 94
6.3 A Short Guide to FMD 96
  6.3.1 The Parameter File 97
  6.3.2 Starting a Simulation 100
  6.3.3 Analysis of Simulation Results 102

LIST OF FIGURES 104
LIST OF TABLES 109
REFERENCES 110

PRESENTATIONS AND PUBLICATIONS 116
10.1 Publications 116
10.2 Talks 117
10.3 Selected Poster Presentations 118

CURRICULUM VITAE 119

INTRODUCTION

1.1 Motivation

Ultra high density storage media with a low signal-to-noise ratio require small magnetic grains. For a given material its maximum areal density is ultimately limited by thermal stability. The energy barrier for thermally activated switching is given by the product $K_u V$, where K_u is the magnetocrystalline anisotropy constant and V is the volume of the magnetic grain. Therefore, reducing the grain size can be balanced by a large anisotropy. Chemically ordered FePt alloys have a magnetocrystalline anisotropy constant in the order of $7 \cdot 10^6$ J/m^3 which is more than ten times larger than that of currently used Co-based alloys. Such a high anisotropy will ensure thermal stability at an average grain size of 5 nm and below, leading to an areal storage density in the Tbit/in^2 regime [1]. Additionally, the magnetic properties of nanoparticles strongly depend on their morphology and the high surface-to-volume ratio. Moreover, the structural properties of nanoparticles strongly depend on their composition. Klemmer and co-workers [2] systematically studied the change of the lattice parameters with composition using X-ray diffraction. The results confirm that the magnetocrystalline anisotropy is correlated with the c/a ratio of the crystal phase. The maximum anisotropy occurs at the maximum tetragonality.

The current roadmap for magnetic storage at ultra-high densities is heat assisted magnetic recording on highly coercive magnetic nanoparticles [3]. A second increasingly important application area of magnetic nanoclusters is nanobiomagnetics [4]. Magnetic nanoparticles will be used for magnetic sensing and for magnetic sorting of biomolecules, proteins, and DNA or for the mechanical manipulation of biological cells. With decreasing size, structural details and the morphology of nanoclusters are primarily determining the overal magnetic properties. The design of magnetic devices and tools in information science and biotechnology requires a fundamental understanding of the magnetic properties of nanoclusters. Magnetic measurements and characterization on the single particle level require an enormous effort. Alternatively, computer simulation can provide a detailed understanding of structure-property relations in magnetic nanoclusters.

In this PhD thesis, a computational framework for investigations on nanocrystalline particles is developed. The objective is a simulation tool that is capable of calculating equilibrium structures of binary alloys and solving the equation of motion for atomic moments in the classical Heisenberg approximation. Furthermore, the simulation of atomic motion and magnetization dynamics should be performed simultaneously, in order to provide a tool to investigate different coupling mechanisms between the elastic system and the magnetic system of a nanocluster. In particular this novel feature of the software is used in chapter 5 of this thesis for the simulation of the effects of surface anisotropy and exchange on the dynamic magnetic properties of nanoparticles. For example, the influence of a change in the surface anisotropy due to thermal fluctuations can be directly computed and is seen in a shift of the thermal stability of magnetic nanoparticles [11].

Whereas software packages for molecular dynamic simulations based on the embedded atom method exist in the public domain [5,6,7], atomistic magnetization dynamics software is used within research groups only [9,10]. In order to combine molecular dynamics and magnetization dynamics it is necessary to have full access to the source code. Furthermore, the molecular dynamics code should be thoroughly understood before adding new features such as the coupling between the magnetization dynamics and the motion of the atoms. Therefore a new software package (cp Appendix 6.3) is developed. The quantum mechanical orign of the forces between the atoms and the ferromagnetic exchange between the atoms is not directly addressed with the simulation tools developed in this thesis. Rather, the interatomic potential, the Heisenberg exchange integral, or the local interface anisotropy are used as input for the simulation. Both, molecular dynamics and magnetization dynamics are based on equations of classical physics. The input parameters may either be taken from empirical studies and measurements or from ab-initio simulations delivering interatomic potentials and exchange integrals. By solving the equation of motion for the atoms and the equation of motion for the magnetic moments simultaneously, mutual interactions between structure and magnetic properties can be studied dynamically.

Chapter 2 of the thesis introduces molecular simulation and in particular discusses the embedded atom method for the simulation of binary alloys. To test the developed methods, bulk material parameters are extracted and compared to known experimental values in chapter 3. The formation of the nanocrystals is modeled using a molecular dynamics approach combined with the embedded atom method in chapter 4. A magnetic model which includes effects arising from morphology and structural composition of nanoclusters is proposed in chapter 5. Furthermore, a representative model system consisting of 1289 Co atoms is used to demonstrate the importance of including the motion of atoms and the specific shape of nanoparticles in magnetic simulations.

MOLECULAR DYNAMICS

In this chapter, the most important concepts necessary to perform molecular dynamics are discussed. Hamilton's formulation is introduced to describe an interacting particle system mathematically. Numerical methods for solving Newton's equations are discussed. Moreover, proper ways of extracting and introducing physical properties such as temperature and pressure are described. Finally, selected numerical aspects and their according implementations are presented.

2.1 Introduction

Molecular dynamics simulations belong to the modeling class of particle models. Particles in a wider sense can be atoms, molecules, dust-particles or even galaxies. Each particle is described by assigning properties such as mass, velocity, charge or a magnetic moment. The dynamics of the particles is modeled by using Newton's second law of motion, giving a direct proportionality between the forces acting on each particle and the rate of change of the momentum (i.e. acceleration) for each particle. Moreover, the direction of the acceleration is equivalent to the direction of the acting force. Knowing the initial values such as velocities and positions, the solution of Newton's equations delivers the dynamic evolution of the system. The forces are calculated by building the derivative of the total potential energy function. Therefore, it is the potential function representing the underlying physical situation.

While the potential function of two separated stars in the (ideally empty) universe is simply the gravitational energy, potential functions for more complex systems can be very hard to determine. Considering atomic structures such as complicated molecules, the calculation of the exact total potential energy function is difficult to determine. In principle it would be possible to use Schrödinger's equation and calculate the evolution of the system from first principles. This approach is numerically challenging and not efficient enough to simulate systems consisting of more than some ten atoms.

Using approximations is therefore the only way to describe large-scale systems on an atomic length scale.

Although solving Newton's equations of motion in an algorithmic way was well known in the last centuries, the development of the methods used in molecular dynamics (MD) simulations is strongly linked with the appearence of *"fast electronic computors"* [12], as stated in one of the first publications employing molecular dynamics numerically. Alder and Wainwright calculated the phase diagram of a hard-sphere system and found a phase transition from liquid to solid, which was very surprising at that time, since the used hard-sphere potential did not have an attractive part.

Rahman investigated liquid Argon by means of molecular dynamics [13]. He was using a Lennard-Jones type potential and, due to the chemical inertness of Argon, this approach delivered excellent results for that time. It should be noted that Argon can still be considered a favorite system to test MD codes since there are numerous results published and the system is sufficiently simple.

Verlet introduced an efficient method to organize a simulation: by keeping lists of neighbors for each atom, the efficiency of the evaluation of the according potential function was improved. He also introduced an integration scheme to solve Newton's equation of motion, which is still in use today [14]. Although this code is denoted as Verlet-Scheme, the origin of his proposed method can be attributed to at least two other persons: to Störmer and even to Delambre (1791) [15].

The basics of molecular dynamics simulations are well established, but research on the methodology of how to simulate different ensembles of atoms correctly is still an ongoing work. In order to compare the results from a simulation with analytical results from thermodynamics, different prerequisites concerning the various thermodynamic potentials have to be established for simulations as well. The modeling of these different ensembles is described in section 2.2.4.

Today, molecular dynamic simulation can be used for complex systems with various elaborate interactions. This is not only due to the fast increase in computation speed but also because of the miniaturization of potentially interesting systems which has rendered detailed investigations possible. Modern magnetic recording applications depend on magnetic grains of the size of some nanometers. Future biomedical applications, such as drug-delivery, will probably utilize small gold-capped magnetic particles to carry medication by means of magnetic fields. Today, these systems can be simulated easily. Their size is small enough to simulate the dynamics on appropriate length scales.

2.2 Mathematical Formulation

Numerous textbooks have been published on the topic of molecular dynamics (e.g. Ref. [16], [17], and [18]), each of them discussing the methodology and concepts used in molecular dynamics simulations. All of them approach the topic from a slightly different point of view. It is not intended to give a comprehensive introduction to all the different mathematical formulations, yet the main ideas used in molecular dynamics simulations will be presented.

2.2.1 Hamiltonian Mechanics in a Nutshell

Using the Hamiltonian mechanics which is a reformulation of the Lagrangian Dynamics, the so-called canonical equations of Hamilton pull together the Hamiltonian H, the generalized variables $\boldsymbol{x}_i$ and their conjugate momentum $\boldsymbol{p}_i$.

$$\dot{\boldsymbol{x}}_i = \nabla_{\boldsymbol{p}_i} H \tag{2.1}$$

$$\dot{\boldsymbol{p}}_i = -\nabla_{\boldsymbol{x}_i} H \tag{2.2}$$

Working with Cartesian coordinates, the generalized momentum describes the linear momentum. In contrast to the Lagrangian formulation which consists of second-order differential equations, Hamilton's equations are first-order and thus more convenient to handle.

Assuming a time-independent transformation of the generalized coordinates, the Hamilton function for a system of *N* degrees of freedom can be written as

$$H = T + V = \sum_{i=1}^{N} \frac{\boldsymbol{p}_i^2}{2m_i} + V(\boldsymbol{x}_1, \ldots, \boldsymbol{x}_N), \tag{2.3}$$

where T denotes the kinetic energy and V is the potential energy, respectively. $\boldsymbol{p}_i$ is the generalized momentum of particle i and m_i denotes the mass. Applying Hamilton's equations (Eq. 2.1 and Eq. 2.2) and using Cartesian coordinates (i.e. the generalized momentum equals the linear momentum $\boldsymbol{p}_i = m_i \boldsymbol{v}_i$), one gets:

$$\dot{\boldsymbol{x}}_i = \boldsymbol{v}_i, \tag{2.4}$$

$$m_i \dot{\boldsymbol{v}}_i = \boldsymbol{F}_i. \tag{2.5}$$

Here, $\boldsymbol{v}_i$ denotes the velocity of the i-th particle and $\boldsymbol{F}_i$ is the negative gradient of a potential function which is not explicitely time-dependent.

$$\boldsymbol{F}_i = -\nabla_{\boldsymbol{x}_i} V(\boldsymbol{x}_1, \ldots, \boldsymbol{x}_N). \tag{2.6}$$

Since $H = T + V$, the Hamilton function represents the total energy of the system. If H does not explicitly depend on time, the total energy of a system remains constant and the energy is a conserved quantity. Therefore, building the total derivation of H with respect to the time t yields

$$\frac{dH}{dt} = \sum_{i=1}^{N} m_i \boldsymbol{v}_i \dot{\boldsymbol{v}}_i + \frac{\partial V}{\partial t} + \sum_{i=1}^{N} \nabla_{\boldsymbol{x}_i} V \cdot \frac{\partial \boldsymbol{x}_i}{\partial t}$$

$$\frac{dH}{dt} = \left(\sum_{i=1}^{N} m_i \dot{\boldsymbol{v}}_i - \sum_{i=1}^{N} \boldsymbol{F}_i \right) \boldsymbol{v}_i. \tag{2.7}$$

Since $\boldsymbol{F}_i = m_i\dot{\boldsymbol{v}}_i$, Eq. 2.7 proves that the Hamiltonian function does not change with time, i.e. the total energy is constant. A molecular dynamics simulation should reproduce this behaviour.

Apart from the total energy, the linear momentum and the angular momentum are also constants of motion. In order to verify a simulation code, calculating constants of motion is a quick and practicable method.

2.2.2 Thermodynamic Quantities in Simple Simulations

Since a mechanically and thermally isolated system can not change its internal energy, solving Eq. 2.4 and Eq. 2.5 delivers an isokinetic simulation, also known as microcanonical ensemble. Unfortunately, isokinetic circumstances are hard to set up in real-life experiments. Instead, it is the temperature which can be adjusted easily on a macroscopic length-scale. Experimentally, the temperature can be adjusted by a heat-bath surrounding the system under investigation. Another quantity which is easily accessible in real life is the pressure. The pressure can be changed by mechanical devices which are limiting or expanding the volume of the experiment. Both associations are mimicked in molecular dynamic simulations to introduce temperature and pressure.

Before the temperature or the pressure can be altered, one has to extract these quantities from the simulation. The temperature can be calculated using the equipartition theorem, the pressure can be determined by using the Clausius virial equation.

Calculation of the Temperature

According to the thermodynamic equipartition theorem, temperature and kinetic energy are directly proportional:

$$\langle E_{\mathrm{kin}} \rangle = \frac{3N}{2} k_{\mathrm{B}} T . \tag{2.8}$$

N denotes the number of particles and k_{B} is Boltzmann's constant (cp. section 6.1). Considering a fixed system (i.e. a fixed center of mass), three degrees of freedom have to be substracted from $3N$, which is the total number of degrees of freedom.

Consequently the temperature can be calculated from Eq. 2.8:

$$T = \frac{1}{3Nk_{\mathrm{B}}} \left\langle \sum_{i=1}^{N} m_i \boldsymbol{v}_i^2 \right\rangle . \tag{2.9}$$

Calculation of the Pressure[1]

Using the Clausius virial function is the starting point for the derivation of the pressure in a molecular dynamics simulation:

$$W(\boldsymbol{x}_1, \ldots, \boldsymbol{x}_N) = \sum_{i=1}^{N} \boldsymbol{x}_i \cdot \boldsymbol{F}_i^{\text{tot}}. \tag{2.10}$$

Here, $\boldsymbol{F}_i^{\text{tot}}$ is the total force acting on atom i. It includes the interatomic forces and the forces originated from the walls of the simulation box. Calculating the statistical average of this function along a trajectory in space yields

$$\langle W \rangle = \lim_{t \to \infty} \frac{1}{t} \int_0^t d\tau \sum_{i=1}^{N} \boldsymbol{x}_i(t) \cdot m_i \ddot{\boldsymbol{x}}_i(t). \tag{2.11}$$

Solving the integral partially delivers

$$\langle W \rangle = -\lim_{t \to \infty} \frac{1}{t} \int_0^t d\tau \sum_{i=1}^{N} m_i \left| \dot{\boldsymbol{x}}_i(t) \right|^2. \tag{2.12}$$

The sum on the right-hand-side represents twice the kinetic energy of the system and can thus be related with the temperature (cp. Eq. 2.9):

$$\langle W \rangle = -3Nk_{\mathrm{B}}T. \tag{2.13}$$

Since the total force can be attributed to internal and external forces, Eq. 2.13 can be reformulated in terms of internal virial contributions and external contributions. Considering a simulation setup with particles located in a box with side lengths L_x, L_y and L_z, respectively, the force acting on the yz-plane of this box equals $-PL_yL_z$, assuming an isotropic external pressure. Accounting for all three dimensions, the external virial can be written as:

$$\langle W^{\text{ext}} \rangle = L_x(-PL_yL_z) + L_y(-PL_xL_z) + L_z(-PL_xL_y) = -3PV. \tag{2.14}$$

Combining Eq. 2.14 and Eq. 2.9 yields

$$\langle W \rangle = \langle W^{\text{ext}} \rangle + \langle W^{\text{int}} \rangle \tag{2.15}$$

$$-3Nk_{\mathrm{B}}T = -3PV + \left\langle \sum_{i=1}^{N} \boldsymbol{x}_i \cdot \boldsymbol{F}_i^{\text{int}} \right\rangle$$

and therefore a possibility to measure the pressure within a molecular dynamics simulation:

---

[1] The derivation of the pressure in the presented form has been taken from [19].

$$P = \frac{1}{V} N k_B T + \frac{1}{3V} \langle \sum_{i=1}^{N} \boldsymbol{x}_i \cdot \boldsymbol{F}_i^{\text{int}} \rangle . \tag{2.16}$$

This equation is called virial equation. In case of non-interacting particles (i.e. $\boldsymbol{F}_i^{\text{int}} = 0$), one gets the well-known equation of state of an ideal gas $PV = Nk_B T$.

Simple Thermostat

Considering Eq. 2.9, the simplest way to set up a desired temperature is to directly change the velocities. This can be done with a correction factor which sets up the desired temperature:

$$\gamma = \sqrt{\frac{E_{\text{kin}}^{\text{target}}}{E_{\text{kin}}^{\text{actual}}}} = \sqrt{\frac{T^{\text{target}}}{T^{\text{actual}}}} . \tag{2.17}$$

Multiplying every single velocity with γ transforms a system from T^{actual} to T^{target}. This is usually performed every few time-steps to allow the system to evolve during the scaling process. In terms of thermodynamics, this procedure does not comply with any known natural source of changing the temperature. Moreover, configurations produced with this attempt do not sample any known statistical mechanic ensemble und therefore it can not be used to extract any thermodynamic quantities. Anyhow, due to its simplicity and its numerical robustness this method is still used to equilibrate a system to reach the designated temperature of a simulation.

Variations of this method use different definitions of the scaling factor. The Berendson method [20] is implemented by using a time-step dependent value of λ, which causes a more gentle way to alter the velocities.

$$\lambda = \sqrt{1 + \frac{\Delta t}{\tau}\left(\frac{T^{\text{target}}}{T^{\text{actual}}} - 1\right)} \tag{2.18}$$

Here, the pertubations of the dynamics can be adjusted by the use of large values of the time constant τ. Anyhow, using this method does neither allow to adjust the temperature in a correct way nor does it deliver any known thermodynamic ensemble.

After a reasonable equilibration time the scaling mechanism can be switched off. Subsequently, the temperature will be close to the desired temperature. The system then represents a microcanonical ensemble with fluctuating temperature and pressure and a constant internal energy. Further adjustments on the temperature are not possible anymore.

2.2.3 Integration Methods

In order to solve Eq. 2.4 and Eq. 2.5 numerically, a discretization of time is necessary. The time period $[0, t_{\text{end}}]$ is therefore devided into I equal intervals. Then, the set of differential equations describing the evolution of the system is only evaluated at discrete points $n(t_{\text{end}}/I)$ in time.

As already mentioned, conservation of energy, angular momentum and linear momentum are prerequisites for a good computer simulation. In addition, the equations of interest are time reversible, thus an integration method should also maintain this feature.

Euler Algorithm

A very simple method to solve Eq. 2.4 and Eq. 2.5 is the Euler algorithm. A Taylor expansion delivers the new positions and the new velocities of the particles at the time $t + \Delta t$

$$\boldsymbol{x}(t+\Delta t) = \boldsymbol{x}(t) + \dot{\boldsymbol{x}}(t)\Delta t + \frac{1}{2}\ddot{\boldsymbol{x}}(t)\Delta t^2 + O(\Delta t^3) \qquad (2.19)$$

$$\boldsymbol{v}(t+\Delta t) = \boldsymbol{v}(t) + \dot{\boldsymbol{v}}(t)\Delta t + O(\Delta t^2) \qquad (2.20)$$

The new position $\boldsymbol{x}(t+\Delta t)$ can thus be calculated from the old position $\boldsymbol{x}(t)$, the velocity $\boldsymbol{v}(t)$, and the acceleration $\dot{\boldsymbol{v}}(t) = \ddot{\boldsymbol{x}}(t)$. The latter is evaluated by using Eq. 2.6 and $\boldsymbol{F}_i = m_i\dot{\boldsymbol{v}}_i$.

The Euler algorithm is an explicit integration scheme and very simple. Unfortunately, the total energy of the system is not conserved strictly. Moreover, it is not time reversible.

Verlet Algorithm

Expanding the position $\boldsymbol{x}$ at two different positions $t + \Delta t$ and $t - \Delta t$ yields

$$\boldsymbol{x}(t+\Delta t) = \boldsymbol{x}(t) + \dot{\boldsymbol{x}}(t)\Delta t + \frac{1}{2}\ddot{\boldsymbol{x}}(t)\Delta t^2 + \ldots$$

$$\boldsymbol{x}(t-\Delta t) = \boldsymbol{x}(t) - \dot{x}(t) + \frac{1}{2}\ddot{\boldsymbol{x}}(t)\Delta t^2 - \ldots .$$

Summation of these two equations leads to

$$\boldsymbol{x}(t+\Delta t) = 2\boldsymbol{x}(t) - \boldsymbol{x}(t-\Delta t) + \ddot{\boldsymbol{x}}(t)\Delta t^2 + O(\Delta t^4). \qquad (2.21)$$

Starting from the actual position and the positions of the system at time $t - \Delta t$, the new positions can be calculated. The accelerations $\ddot{\boldsymbol{x}}(t)$ are gathered by using Eq. 2.6 again. Since the velocities are not explicitly quoted in this scheme, a second-order differential scheme can be used to get these values:

$$\dot{\boldsymbol{x}}(t) = \frac{\boldsymbol{x}(t+\Delta t) - \boldsymbol{x}(t-\Delta t)}{2\Delta t} + O(\Delta t^2)$$

The Verlet algorithm [14] is time reversible and does not obtain any energy drift. Since the calculation of the new positions requires to store the actual position and one position from the past, the memory consumption of an implementation of this code is higher as compared to the Euler algorithm. Moreover, when starting the calculation, positions at time step $t - \Delta t$ have to be supplied with a different method, since no data for $t - \Delta t$ is available.

Leapfrog Algorithm

The lack of velocities within the main algorithm can be overcome by defining half step velocities:

$$\dot{\boldsymbol{x}}(t-\Delta t/2) = \frac{\boldsymbol{x}(t)-\boldsymbol{x}(t-\Delta t)}{\Delta t} \tag{2.22}$$

$$\dot{\boldsymbol{x}}(t+\Delta t/2) = \frac{\boldsymbol{x}(t+\Delta t)-\boldsymbol{x}(t)}{\Delta t} \tag{2.23}$$

From the last expression one gets an integration rule for the new positions utilizing the velocity at a semi-future point in time:

$$\boldsymbol{x}(t+\Delta t) = \boldsymbol{x}(t)+\Delta t\cdot\dot{\boldsymbol{x}}(t+\Delta t/2). \tag{2.24}$$

Rearranging Eq. 2.21 and utilizing Eq. 2.22 yields the velocities at the future half-step $t+\Delta t/2$:

$$\begin{aligned}\boldsymbol{x}(t+\Delta t)-\boldsymbol{x}(t) &= \boldsymbol{x}(t)-\boldsymbol{x}(t-\Delta t)+\ddot{\boldsymbol{x}}(t)\Delta t^2+O(\Delta t^4)\\ \dot{\boldsymbol{x}}(t+\Delta t/2)\Delta t &= \dot{\boldsymbol{x}}(t-\Delta t/2)\Delta t+\ddot{\boldsymbol{x}}(t)\Delta t^2+O(\Delta t^4)\end{aligned} \tag{2.25}$$

First, the accelerations are again calculated by building the gradient of the potential function, then the velocities at the time step $t+\Delta t/2$ are evaluated (Eq. 2.25) and finally the new positions can be obtained by using Eq. 2.24.

Compared to the Verlet algorithm, only the values of the actual positions are used to calculate the new position at time step $t+\Delta t$. A disadvantage of this scheme is, that the velocities are only known at half-time steps. This can be overcome by simply interpolating between the known half-time steps. Again, a special start-up sequence has to be implemented to get the inital velocities at $t_0-\Delta t/2$.

Velocity Verlet Algorithm

Since the Leapfrog algorithm does not supply the velocities at the time step $t+\Delta t$, which is necessary to calculate the kinetic energy, a different approach is used to solve this problem. Again, the starting point is a Taylor expansion, carried out for the position $\boldsymbol{x}(t+\Delta t)$. The velocities at this time step are calculated by adding a mean value of the actual and the future acceleration (Eq. 2.26). This will lead to a scheme where the velocities are known at the desired time step.

$$\boldsymbol{x}(t+\Delta t) = \boldsymbol{x}(t)+\dot{\boldsymbol{x}}(t)\Delta t+\frac{1}{2}\ddot{\boldsymbol{x}}(t)\Delta t^2+\ldots$$

$$\dot{\boldsymbol{x}}(t+\Delta t) = \dot{\boldsymbol{x}}(t)+\frac{\ddot{\boldsymbol{x}}(t)+\ddot{\boldsymbol{x}}(t+\Delta t)}{2}\Delta t \tag{2.26}$$

This algorithm can be implemented by calculating the new velocities at the half-step $t+\Delta(t/2)$ from the actual accelerations and the actual velocities. To obtain the new positions, the mid-point velocities are used (Eq. 2.27). The new accelerations are then evaluated at the new positions using the gradient of the potential at the position $\boldsymbol{x}(t+\Delta t)$. Finally, the new velocities at the time-step $t+\Delta t$ can be calculated by using the result from Eq. 2.27 and adding the new accelerations from Eq. 2.29.

$$\dot{\boldsymbol{x}}(t + \Delta(t/2)) = \dot{\boldsymbol{x}}(t) + \frac{\Delta t}{2}\ddot{\boldsymbol{x}}(t) \tag{2.27}$$

$$\boldsymbol{x}(t + \Delta t) = \boldsymbol{x}(t) + \dot{\boldsymbol{x}}(t + \Delta t/2)\Delta t \tag{2.28}$$

$$\ddot{\boldsymbol{x}}(t + \Delta t) = -\frac{1}{m}\nabla U(\boldsymbol{x}(t + \Delta t)) \tag{2.29}$$

$$\dot{\boldsymbol{x}}(t + \Delta t) = \dot{\boldsymbol{x}}(t + \Delta t/2) + \frac{\Delta t}{2}\ddot{\boldsymbol{x}}(t + \Delta t) \tag{2.30}$$

Since the velocities have to be stored at the half-time step during an integration step, the Velocity-Verlet algorithm needs an additional variable in the implementation. Anyhow, since the velocities are naturally known at each time step, this method is very feasible in practice. Moreover, the Velocity-Verlet-Scheme is often used for more elaborate integration schemes involving different thermodynamic ensembles.

2.2.4 Extended Hamiltonians

In order to simulate thermodynamic ensembles such as the canonical ensemble or the isothermal-isobaric ensemble correctly, the standard Hamiltonian has to be extended. This extension mimicks the underlying physical situation. In the case of a canonical ensemble (NVT) with a constant number of particles N, constant volume V and temperature T, the according extension to Eq. 2.3 is a representation of a heat bath. Apart from the Nosé-Hoover thermostat below, several other methods to control temperature and pressure have been published. To illustrate the ideas behind extended Hamiltonians, the Nosé-Hoover formalism is discussed in detail.

Nosé-Hoover Thermostat

Nosé [21] proposed an extended Hamiltionian with an additional degree of freedom featuring the heat bath.

$$H_{\text{Nosé}} = \sum_i \frac{\tilde{p}^2}{2m_i s^2} + V(\tilde{\boldsymbol{x}}_1, \ldots, \tilde{\boldsymbol{x}}_N) + \frac{\pi^2}{2Q} + \tilde{g}k_{\mathrm{B}}T\ln s \tag{2.31}$$

π is the the extended momentum of the heat bath and s its conjugate variable which can be interpreted as a position. Q represents the virtual mass assigned to the heat bath and $\tilde{g} = N_f + 1$ with N_f being the number of degrees of freedom of the real system. The extendend system is described in a virtual formulation of the variables which are related to real variables by the following transformations

$$\boldsymbol{x}_i = \tilde{\boldsymbol{x}}_i \qquad \boldsymbol{p}_i = \frac{\tilde{\boldsymbol{p}}_i}{s} \qquad t = \int_0^t \frac{\mathrm{d}\tilde{t}}{s} \tag{2.32}$$

Eq. 2.31 implies, that the system is described in a virtual time formulation [22]. That is to say that configurations are not available at evenly spaced times. Anyhow, as long as no correlation functions are calculated, where data is needed at the equidistant points in time, this issue does not matter. Applying Eq. 2.1 and Eq. 2.2 on the extended Hamiltonian yields

$$\frac{d\tilde{\boldsymbol{x}}_i}{d\tilde{t}} = \frac{\tilde{p}_i}{m_i s^2} \qquad \frac{ds}{d\tilde{t}} = \frac{\pi}{Q} \tag{2.33}$$

for the coordinates and

$$\frac{d\tilde{\boldsymbol{p}}_i}{d\tilde{t}} = -\frac{\partial}{\partial \tilde{\boldsymbol{x}}_i} V(\tilde{x}_1, \ldots, \tilde{x}_N) \qquad \frac{d\tilde{\pi}}{d\tilde{t}} = \sum_i \frac{\tilde{\boldsymbol{p}}_i^2}{m_i s^3} - \frac{\tilde{g} k_{\mathrm{B}} T}{s} \tag{2.34}$$

for the according momenta. Using the transformation rules given in Eq. 2.32 results in a real time formulation:

$$\begin{aligned} &\dot{\boldsymbol{x}}_i = \frac{\boldsymbol{p}_i}{m_i} \qquad \dot{s} = \frac{s^2 \pi}{Q} \\ &\dot{\boldsymbol{p}}_i = -\frac{\partial}{\partial \boldsymbol{x}_i} V(\boldsymbol{x}_1, \ldots, \boldsymbol{x}_N) - \boldsymbol{p}_i \frac{s\pi}{Q} \qquad \dot{\pi} = \frac{1}{s}\left(\sum_i \frac{\boldsymbol{p}_i^2}{m_i} - g k_{\mathrm{B}} T\right) - \frac{s\pi^2}{Q} \end{aligned} \tag{2.35}$$

Here, the time derivative is carried out in respect to the real time t (represented by a superior dot notation). Hoover [23] proposed another transformation of the variables, namely

$$\xi = \frac{s\pi}{Q} \qquad \eta = \ln s. \tag{2.36}$$

These transformations result in a decoupling of the coordinate s from the system and eliminate the variable π:

$$\begin{aligned} &\dot{\boldsymbol{x}}_i = \frac{\boldsymbol{p}_i}{m_i} \qquad \dot{\eta} = \xi \\ &\dot{\boldsymbol{p}}_i = -\frac{\partial}{\partial \boldsymbol{x}_i} V(\boldsymbol{x}_1, \ldots, \boldsymbol{x}_N) - \boldsymbol{p}_i \xi \qquad \dot{\xi} = \frac{1}{Q}\left(\sum_i \frac{\boldsymbol{p}_i^2}{m_i} - g k_{\mathrm{B}} T\right) \end{aligned} \tag{2.37}$$

This system of equations of motion is called Nosé-Hoover formulation. Compared to the original set of equations, here g represents the number of degrees of freedom of the system in order to get the correct temperature.

To solve Eq. 2.37, implicit [17] and explicit [24],[25] integration schemes have been published. In order to make the integration scheme comparable, the solution is given in the same form as presented in Eq. 2.27 - Eq. 2.30:

$$\dot{\boldsymbol{x}}(t+\Delta t/2) = \frac{1}{1+\xi(t)\frac{\Delta t}{2}}\left(\dot{\boldsymbol{x}}(t)+\frac{\Delta t}{2}\ddot{\boldsymbol{x}}(t)\right)$$

$$\boldsymbol{x}(t+\Delta t) = \boldsymbol{x}(t)+\dot{\boldsymbol{x}}(t+\Delta t/2)\Delta t \tag{2.38}$$

$$\xi(t+\Delta t) = \xi(t)+\frac{\Delta t}{Q}\left(\sum_i m_i(\dot{\boldsymbol{x}}(t+\Delta t/2))^2-gk_{\mathrm{B}}T\right) \tag{2.39}$$

$$\eta(t+\Delta t) = \eta(t)+\frac{\Delta t}{2}(\xi(t+\Delta t)+\xi(t)) \tag{2.40}$$

$$\ddot{\boldsymbol{x}}(t+\Delta t) = -\frac{1}{m}\nabla U(\boldsymbol{x}(t+\Delta t)) \tag{2.41}$$

$$\dot{\boldsymbol{x}}(t+\Delta t) = \dot{\boldsymbol{x}}(t+\Delta t/2)+\frac{\Delta t}{2}(\ddot{\boldsymbol{x}}(t+\Delta t)+\xi(t+\Delta t)m_i\dot{\boldsymbol{x}}(t+\Delta t/2)) \tag{2.42}$$

It should be noted that the Nosé-Hoover formulation represents a NVT-ensemble thermodynamically, the internal energy is now fluctuating and not any longer a constant of motion. However, Eq. 2.31 features a conserved quantity, an extended energy accounting for both, the internal degrees of freedom and the modeled heat bath.

$$E_{\mathrm{ext}} = \sum_i \frac{\boldsymbol{p}_i^2}{2m_i}+V(\boldsymbol{x}_1,\ldots,\boldsymbol{x}_N)+\frac{Q\xi^2}{2}+gk_{\mathrm{B}}T\eta \tag{2.43}$$

Discussion

The Nosé-Hoover method is commonly used to adjust the temperature in a molecular dynamics simulation. It samples canonical configurations. Therefore, results can be directly used to obtain thermodynamic quantities from the simulation. Anyhow, since the variable transformations change the structure of the equations of motion, the transformation is non-Hamiltonian. Recently, this issue has been solved by introducing the *Nosé-Poincaré* method [22]. This method does not need any non-Hamiltonian transformation, therefore the system is symplectic and time reversible. It was Nosé, who published an explicit symplectic time-integrator for the Nosé-Poincaré thermostat [26].

The introduction of a heat bath with associated fictional mass Q, momentum π and coordinate s allows for energy exchange. Consequently, not only the system being investigated needs time to equilibrate, also the heat bath has to be equilibrated. Generally, a different approach should be used to set up an initial temperature before extracting thermodynamical quantities from the simulation. In practice, this can be implemented by using two different thermostats, e.g. a velocity scaling method in the beginning of the simulation and a more elaborate method for the production period.

It should be noted that due to the introduction of a fictional degree of freedom, the dynamics of the system also change. Non-physical oscillations exhibiting a period of

$$t_0 = 2\pi\sqrt{\frac{Q}{2gk_BT}}$$

are introduced. Consequently, data collection can only be obtained by averaging over many of these periods. The fictional mass should be chosen in a way that t_0 is large compared to dynamic fluctuations of the system. An effective method to evaluate the choice of Q is to compare the distribution of temperatures with the expected canonical distribution of temperatures:

$$p(T) = \exp\left(-\frac{3N(T-T_{\text{act}})^2}{2T^2}\right). \tag{2.44}$$

A heat bath should be large compared to the system which it is equilibrated with. Modeling this heat bath with a single degree of freedom might therefore be a weak approach. Thus, a chaining of the thermostats has been proposed. That is to say, a second (or even more) degree(s) of freedom acts as a thermostat on the first degree of freedom. This can be extended to an arbitrary number of thermostats, called chaining of thermostats. Recently, Leimkuhler and co-workers [27] presented a symplectic integration scheme for both Nosé and Nosé-Poincaré chains.

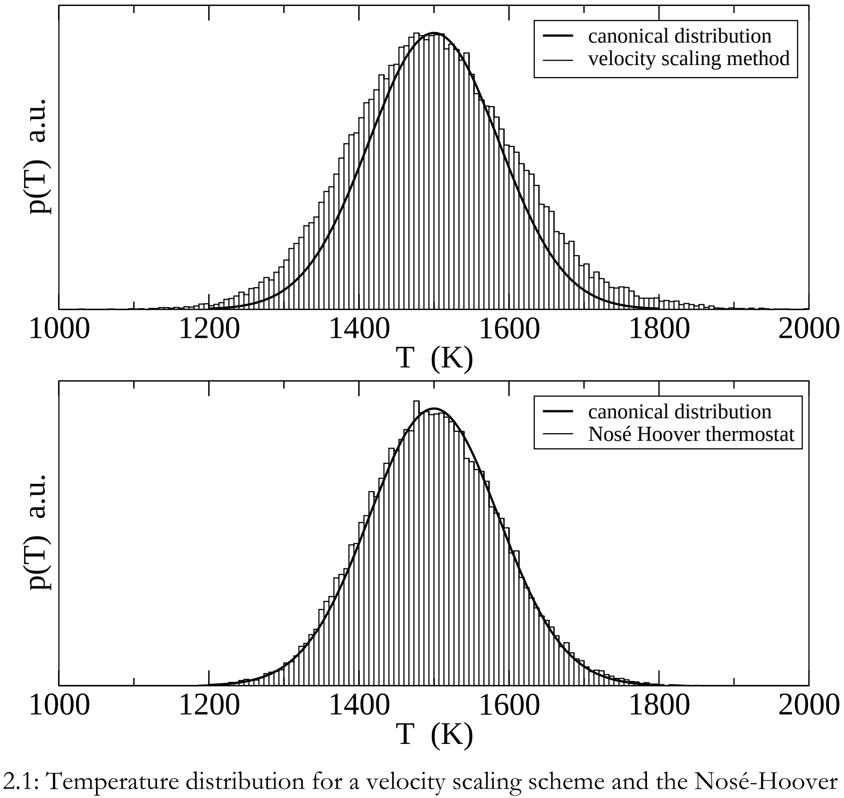

Figure 2.1: Temperature distribution for a velocity scaling scheme and the Nosé-Hoover method. Whereas the Nosé-Hoover scheme reproduces the canonical distribution well, the velocity scaling scheme does not reproduce the desired distribution. (simulated system: Ag, 100 atoms, total number of integration steps: $2\text{x}10^6$, $Q=10^6$, desired temperature: 1500K)

2.3 Potentials

Using appropriate integrators is only one part of a successful and correct simulation of a physical system. Interactions between particles are described by the potential function which is used to calculate the intra-particle forces. Thus, it is important to use potentials capable of reproducing real physical quantities.

However, describing a set of a relatively small number of atoms by means of classical mechanics might need some further justification. Interactions on atomic scales are generally described by the Schrödinger equation. Consequently the solution of the time-dependent Schrödinger equation should describe a system evolving in time. Unfortunately, solving a many-body Schrödinger equation for a large number of atoms is still a challenge to even the fastest computers available. Therefore approximations and simplifications are necessary. A comprehensive discussion about deriving molecular dynamics from first principle considerations can be found in [18].

In terms of quantum mechanics, one of the most powerful ideas is to separate the electronic and the nucleus' wave functions (Born-Oppenheimer approximation). Solving the electronic part of the problem provides a potential which can be subsequently used as potential in the second Schrödinger equation to calculate the motion of the nuclei. Due to the fact that the total mass of electrons is much smaller than the mass of the nuclei, this separation seems valid. This approach results in ab-inito molecular dynamics.

A further simplification can be made by using an effective potential describing the electronic system. This potential is then used to calculate the intra-atomic forces. This approach is used in the classical molecular dynamics approach.

Due to its historical importance, the Lennard-Jones potential will be discussed to illustrate the main features of a pair-potential and its usage in a molecular dynamics simulation. The focus of this thesis is predominantly set to metals, thus the embedded atom method has been chosen to model this class of materials. It is discussed in section 2.3.2.

2.3.1 Lennard-Jones Potentials

Introduced well before the invention of automatic computer devices, Lennard-Jones [28] proposed a potential function best known for describing the interaction between noble gas atoms. Due to its simplicity, the Lennard-Jones potential is appropriate to test a new molecular dynamics code. The potential consists of a repulsive and an attractive part, the repulsive part can be interpreted as being a representation of the Pauli-repulsion caused by overlapping electron wave functions exhibiting equal spins. The attractive part of the potential models mainly Van-der-Waals forces and permanent dipol-dipol-interactions. In its parameterized form it often appears as

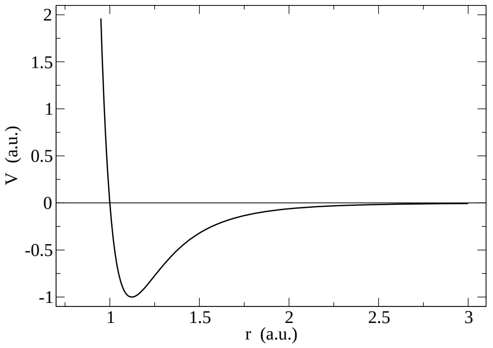

Figure 2.2: Lennard-Jones potential for $\sigma = 1$ and $\varepsilon = 1$. Note that on the abscissa the potential approaches zero rapidly. This legitimates the usage of a cut-off radius.

$$V_{\text{tot}}(\boldsymbol{x}_1, \dots, \boldsymbol{x}_N) = 2\varepsilon \sum_{i=1} \sum_{j \neq i} \left(\left(\frac{\sigma}{r^{ij}} \right)^{12} - \left(\frac{\sigma}{r^{ij}} \right)^{6} \right) \tag{2.45}$$

where r_{ij} is the distance between atom i and j, ε is the depth of the potential. A higher value of ε leads therefore to tighter bindings. σ describes the zero-crossing point of the potential; the minimum of the potential (i.e. zero force) can be found at $2^{1/6}\sigma$. Fig. 2.2 shows a Lennard-Jones potential for $\varepsilon = 1$ and $\sigma = 1$, respectively.

Building the gradient of this potential delivers the direction and the strength of the force (devided by m_k) acting on atom k:

$$\boldsymbol{f}^k = -\nabla_{\boldsymbol{x}_k} V_{\text{tot}} = -2\varepsilon \sum_{i=1} \sum_{j \neq i} \left(\frac{\partial}{\partial r^{ij}} \left(\frac{\sigma}{r^{ij}} \right)^{12} - \frac{\partial}{\partial r^{ij}} \left(\frac{\sigma}{r^{ij}} \right)^{6} \right) = \tag{2.46}$$

$$2\varepsilon \sum_{i=1} \sum_{j \neq i} \left(\frac{12\boldsymbol{r}^{ij}}{r^{ij^2}} \left(\frac{\sigma}{r^{ij}} \right)^{12} (\delta^{kj} - \delta^{ki}) - \frac{6\boldsymbol{r}^{ij}}{r^{ij^2}} \left(\frac{\sigma}{r^{ij}} \right)^{6} (\delta^{kj} - \delta^{ki}) \right) =$$

$$12\varepsilon \left(\sum_{i \neq k} \frac{2\boldsymbol{r}^{ik}}{r^{ik^2}} \left(\frac{\sigma}{r^{ik}} \right)^{12} - \sum_{k \neq j} \frac{2\boldsymbol{r}^{kj}}{r^{kj^2}} \left(\frac{\sigma}{r^{kj}} \right)^{12} - \sum_{i \neq k} \frac{\boldsymbol{r}^{ik}}{r^{ik^2}} \left(\frac{\sigma}{r^{ik}} \right)^{6} + \sum_{i \neq k} \frac{\boldsymbol{r}^{kj}}{r^{kj^2}} \left(\frac{\sigma}{r^{kj}} \right)^{6} \right) =$$

$$24\varepsilon \left(\sum_{k \neq i} \frac{\boldsymbol{r}^{ki}}{r^{ki^2}} \left(\frac{\sigma}{r^{ki}} \right)^{6} - \frac{2\boldsymbol{r}^{ki}}{r^{ki^2}} \left(\frac{\sigma}{r^{ki}} \right)^{12} \right) = 24\varepsilon \sum_{k \neq i} \frac{\boldsymbol{r}^{ki}}{r^{ki^2}} \left(\left(\frac{\sigma}{r^{ki}} \right)^{6} - 2 \left(\frac{\sigma}{r^{ki}} \right)^{12} \right)$$

2.3.2 Embedded Atom Method

Molecular dynamics simulations using empirical two-body potentials, like the Lennard-Jones potential type, are not suitable for applications involving chemical active materials or metals [29]. Although such simple approaches can deliver the correct ground-state energy, specific properties, such as the elastic constants of metals, can not be reproduced [30]. To overcome these problems more elaborate potentials were developed: Daw and Baskes introduced the embedded atom method [31], an approach based on the idea of quasiatoms [32]. A quasiatom is defined as a unit consisting of the ion and its electronic screening cloud. Considering this unit as impurity in an electronic system, the energy of this quasiatom only depends on the electron density of the host.

The main feature of the embedded atom method is based on the idea of quasiatoms: every single atom in a system is now considered as beeing an impurity in the host. The energy of the embedded atom i is now calculated via an embedding function F_i, dependent on the electronic density caused by the host at the position of the impurity:

$$V_i^{\mathrm{emb}} = F_i(\rho_i^{\mathrm{h}}) . \tag{2.47}$$

Here, the electronic density ρ_i^{h} is just the sum over all electron density functions of all other atoms:

$$\rho_i^{\mathrm{h}} = \sum_{j \neq i} \rho_j^{\mathrm{a}}(r_{ij}) \tag{2.48}$$

Combining the embedding potential with a pair potential

$$V_i^{\mathrm{pair}} = \frac{1}{2} \sum_{j, j \neq i} \phi_{ij}(r_{ij}) \tag{2.49}$$

yields the total embedding atom potential function:

$$V = \sum_i V_i^{\mathrm{emb}} + \sum_i V_i^{\mathrm{pair}} \tag{2.50}$$

Although these potentials exhibit features of many-body interactions, their mathematical form is still simple to implement.

In practice, the embedding function F_i is fitted to obtain reasonable bulk material parameters such as the lattice constants, elastic constants or vacancy free energies. For the electron density function ρ_i^{atom} only electron orbitals outside the screening regime of an atom have to be considered. They can be either calculated by a simple Hartree-Fock approximation [18] or other functional shapes are fitted to the desired density [33]. A comprehensive analytical investigation on the nature of the embedded atom method can be found in Ref. [34].

Building the gradient of the total potential function with respect to the particle position $\boldsymbol{x}_k$ yields the force on this particle.

$$\begin{aligned} \boldsymbol{F}^k &= -\nabla_{\boldsymbol{x}_k} V_{\text{tot}} \\ \boldsymbol{F}^k &= -\nabla_{\boldsymbol{x}_k} \sum_i f^i(\rho^{\text{h},\,i}) - \nabla_{\boldsymbol{x}_k} \frac{1}{2} \sum_i \sum_{j,\,j \neq i} \phi^{ij}(r^{ij}) \end{aligned} \tag{2.51}$$

with r^{ij} being the distance between particle i and j:

$$r^{ij} = \left| r^j - r^i \right| .$$

To evaluate Eq. 2.51 the two terms on the right-hand-side are evaluated separately:

$$\begin{aligned} &-\nabla_{\boldsymbol{x}_k} \frac{1}{2} \sum_i \sum_{j,\,j \neq i} \phi^{ij}(r^{ij}) = -\frac{1}{2} \sum_i \sum_{j,\,j \neq i} \frac{\partial}{\partial r^{ij}} \phi^{ij}(r^{ij}) \frac{\boldsymbol{r}^{ij}}{r^{ij}} (\delta^{kj} - \delta^{ki}) = \quad . \\ &-\frac{1}{2} \sum_i \sum_{j,\,j \neq i} \frac{\partial}{\partial r^{ij}} \phi^{ij}(r^{ij}) \frac{\boldsymbol{r}^{ij}}{r^{ij}} \delta^{kj} + \frac{1}{2} \sum_i \sum_{j,\,j \neq i} \frac{\partial}{\partial r^{ij}} \phi^{ij}(r^{ij}) \frac{\boldsymbol{r}^{ij}}{r^{ij}} \delta^{ki} = \\ &-\frac{1}{2} \sum_{i,\,i \neq k} \frac{\partial}{\partial r^{ik}} \phi^{ik}(r^{ik}) \frac{\boldsymbol{r}^{ik}}{r^{ik}} + \frac{1}{2} \sum_{j,\,j \neq k} \frac{\partial}{\partial r^{kj}} \phi^{kj}(r^{kj}) \frac{\boldsymbol{r}^{kj}}{r^{kj}} = \\ &-\sum_{i,\,i \neq k} \frac{\partial}{\partial r^{ik}} \phi^{ik}(r^{ik}) \frac{\boldsymbol{r}^{ik}}{r^{ik}} \end{aligned} \tag{2.52}$$

$$\begin{aligned} -\nabla_{\boldsymbol{x}_k} \sum_i f^i(\rho^{\text{h},\,i}) &= -\nabla_{\boldsymbol{x}_k} \sum_i f^i\left(\sum_{j,\,j \neq i} \rho^j(r^{ij}) \right) = \\ &-\sum_i \frac{\partial}{\partial \rho^{\text{h},\,i}} f^i(\rho^{\text{h},\,i}) \sum_{j,\,j \neq i} \frac{\partial}{\partial r^{ij}} \rho^j(r^{ij}) \frac{\boldsymbol{r}^{ij}}{r^{ij}} (\delta^{kj} - \delta^{ki}) \\ &= -\sum_{i,\,i \neq k} \frac{\partial}{\partial \rho^{\text{h},\,i}} f^i(\rho^{\text{h},\,i}) \frac{\partial}{\partial r^{ik}} \rho^k(r^{ik}) \frac{\boldsymbol{r}^{ik}}{r^{ik}} + \frac{\partial}{\partial \rho^{\text{h},\,k}} f^k(\rho^{\text{h},\,k}) \sum_{j,\,j \neq k} \frac{\partial}{\partial r^{ij}} \rho^j(r^{kj}) \frac{\boldsymbol{r}^{kj}}{r^{kj}} \\ &= -\sum_{i,\,i \neq k} \left(\frac{\partial}{\partial \rho^{\text{h},\,i}} f^i(\rho^{\text{h},\,i}) \frac{\partial}{\partial r^{ik}} \rho^k(r^{ik}) + \frac{\partial}{\partial \rho^{\text{h},\,k}} f^k(\rho^{\text{h},\,k}) \frac{\partial}{\partial r^{ik}} \rho^i(r^{ik}) \right) \frac{\boldsymbol{r}^{ik}}{r^{ik}} \end{aligned} \tag{2.53}$$

Since both, the derivative of the embedding function and the density function, can be tabulated, this form is especially useful in numeric calculations. Combining Eq. 2.52 and Eq. 2.53 yields the force on the particle k:

$$\begin{aligned} \boldsymbol{F}^k = -\sum_{i,\,i \neq k} \Bigg(&\frac{\partial}{\partial r^{ik}} \phi^{ik}(r^{ik}) + \frac{\partial}{\partial \rho^{\text{h},\,i}} f^i(\rho^{\text{h},\,i}) \frac{\partial}{\partial r^{ik}} \rho^k(r^{ik}) + \\ &\frac{\partial}{\partial \rho^{\text{h},\,k}} \left(f^k(\rho^{\text{h},\,k}) \frac{\partial}{\partial r^{ik}} \rho^i(r^{ik}) \right) \Bigg) \frac{\boldsymbol{r}^{ik}}{r^{ik}} \end{aligned} \tag{2.54}$$

In practice, potential functions are either published as columns of numbers or in parameterized form. Numerically it is more efficient to store the potential functions and density functions as pre-computed values with a subsequent interpolation scheme after the look-up process than to evaluate the potential functions.

2.4 Selected Numerical Aspects and Data Structures

Normally, molecular dynamics simulations are performed with time-independent potentials. Thus, using a decent integration scheme and a reasonable potential should obtain physical properties such as the conservation of the total energy or the conservation of the total momentum. The extraction of these quantities after a simulation run is therefore an excellent method to evaluate the quality of a given code.

2.4.1 Integration of Closed Loops

In order to prove the calculation of the forces from building the gradient of the potential function, a random configuration of atoms is used and their respective positions in space is kept fix. Additionally, another atom is used, which is now moved along a closed path through this cloud of atoms. Since the performed work on a closed path in a conservative energy landscape yields zero, line-integrating the force on a closed track should also result in zero work. To get a decent accuracy, $\Delta \boldsymbol{x}$ was chosen to be as small as $0.1 \cdot 10^{-13}\mathrm{m}$. Although no special integration algorithm has been used, the work at the inital position after a full loop was in the order of 10^{-4} relative to full scale.

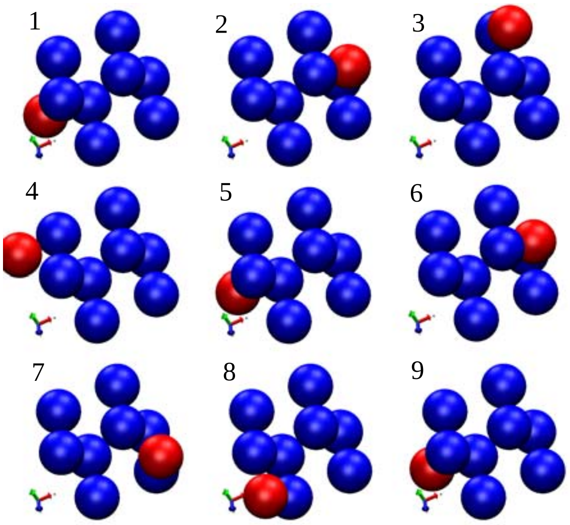

Figure 2.3: Method to test, whether a used potential is conservative or not. The blue spheres represent a configuration of atoms at fixed postitions whereas the red sphere follows a closed loop. Integrating the calculated forces along the closed loop should yield zero work when reaching the initial position again. State 1, 5 and 9 clearly show that no work has been performed on a closed loop, which indicates that the potential function is conservative. The graph below depicts three different closed loops through the configuration of the blue spheres generating the potential landscape. An embedded atom potential for Co was used for this calculation.

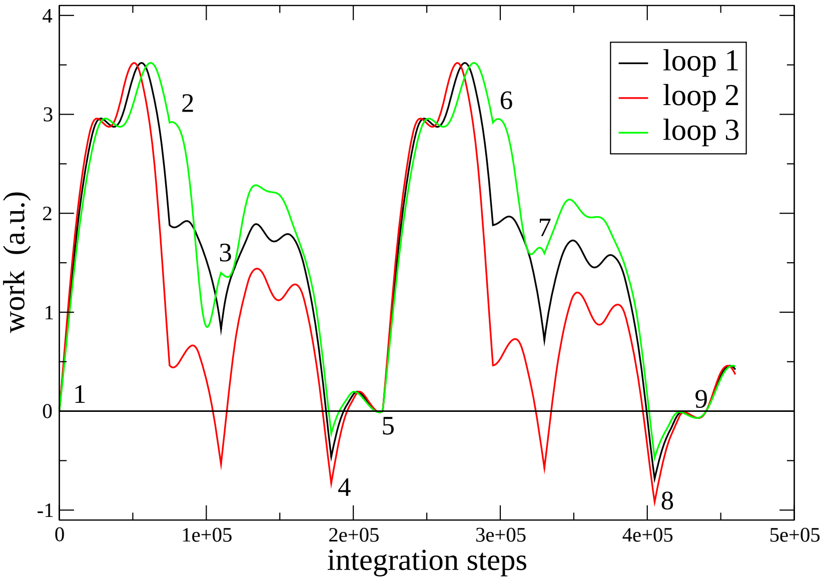

2.4.2 Cut-off Radius and Representation of the Simulation

In general molecular dynamics is numerically challenging. Apart from the integration scheme, the evaluation of the forces is very time-consuming (Eq. 2.54). In principle, the distance between each particle has to be calculated to evaluate a single force. For large-scale calculations, calculating the N^2 distances and the appropriate forces slows down the simulation.

Luckily, interatomic forces are in general short-ranged. That is to say, atoms with a larger distance do not contribute significantly to the total force on the considered atom. Therefore, defining a cut-off radius around each atom reduces the number of significant atoms to a constant number, independent on the total number of atoms of the system. It should be noted, that it is important to use potential functions exhibiting a smooth crossover from non-zero values to zero for distances larger than the cut-off radius, since it is not the potential function itself but the derivative of the function being used to calculate the force. A step at the cut-off radius would therefore lead to irregularities in the simulation results.

Anyhow, using a cut-off radius does only reduce the number of force evaluations - the number of distance calculations remains constant. Especially at low temperatures the neighborhood of an atom does not change significantly with time. In other words, the determination of the neighboring atoms within the cut-off radius at each timestep can be reduced to a determination of the neighborhood every few time-steps. The neighbors of an atom are therefore stored in special lists, the distances to this neighborhood-atoms are updated *every* time-step. This approach is called neighbor list scheme and is very effective for small scale simulations ($N \leq 10^3$).

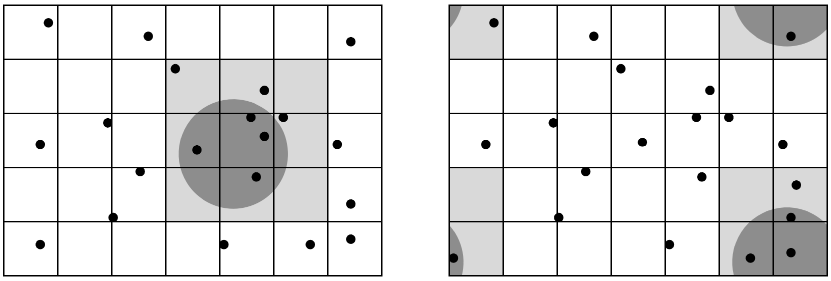

Figure 2.4: Linked-cell geometry (two-dimensional). The left picture represents a 7x5 cell geometry. Each cell has to have at least a side length of r_{cut}. Thus, only neighboring cells have to be considered while finding relevant atoms. On the right, the minimum image convention is depicted, i.e. an atom in the corner cell interacts with cells from the opposite border. Each cell has 8 (2D) and 26 (3D) neighbor cells, respectively.

Another possibility is to split the simulation regime into pieces exhibiting a typical length of r_{cut}. If stored in a decent data structure, it is only necessary to consider the neighbors of a cell (cp. Fig. 2.4). The individual cells are at least r_{cut} in size. Therefore, almost only relevant atoms will be found in the immediate neighbor cells. In order to design this process effectively, a linked list algorithm is used to access atoms of different cells.

Due to it special design, the linked-cell scheme does have some limitations. Since each cell has to be at least r_{cut} in size and no cell can have itself as neighbor, the minimum simulation volume is $3 \times 3 \times 3 \times r_{\text{cut}}^3$. Using a smaller number of cells results in atoms interacting with themselves. On the other hand, a reduction of the cell size to values smaller than r_{cut} yields unsteady potential functions at the cell boundary. Both situations are unphysical.

Due to the special way of storing the atoms, additional computation is necessary. Migrating atoms need special treatment, since they can leave their initial cell. They have to be moved to a different cell. It is the overhead-calculation which makes the linked-cell scheme better suited for large scale simulations ($N > 10^3$). Linked cell schemes are also well suited to be implemented on parallel computers.

Fig. 2.5 shows a comparison between both ways to handle the geometry. Whereas the simulation time per particle is independent on the total number of atoms for the linked cell scheme, the simulation time per particle rises when calculated with the neighborlist method.

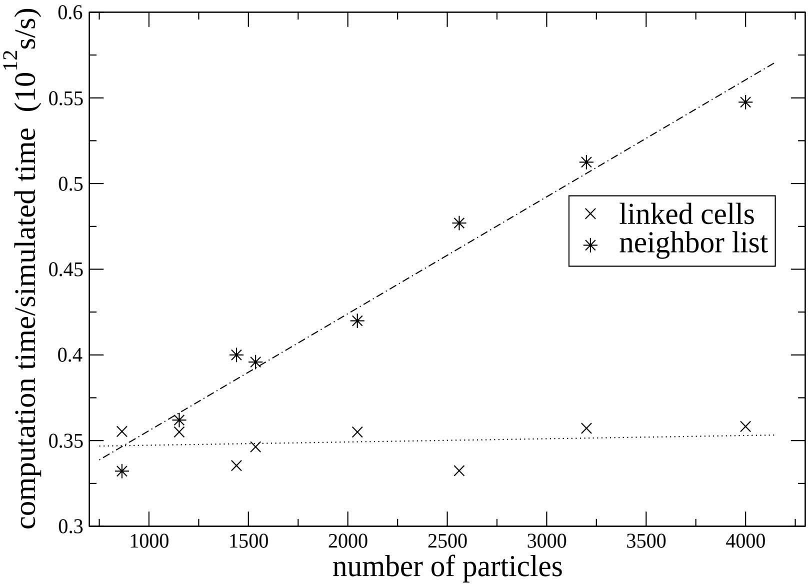

Figure 2.5: Comparison between an algorithm using the linked-cells method and the neighbor list algorithm. The linked-cells computation time per particle is independent on the total number of particles simulated. When performing calculations with only some hundreds of atoms involved, the neighbor list algorithm is faster due to additional overhead computation. The unit on the ordinate represents a measure between reality and simulation: Unity would represent a real-time capability of a simulation in a one-processor per particle approach.

2.4.3 Comparison Between Tabulated Potentials and Analytical Functions

Using the embedded atom method, the calculation of the individual forces acting on the atoms involves the derivatives of the pair potential function $\phi(r)$, the electron density $\rho(r)$ and the derivative of the embedding function $F(\rho)$. Usually, these functions are given in a parameterized form, for example as cubic spline functions (cp. section 6.1). If given in an analytical form, implementing this parameterized function including the necessary derivatives yields the best numerical accuracy possible.

Since the evaluation of these parameterized functions has to be performed every time step, complex functions are slowing down a molecular dynamics simulation drastically. A different way to evaluate these functions is to store pre-computed values for the expected input values. In the case of the pair potential and the electron function it is sufficient to store values up to the cut-off radius as upper limit and half of the nearest neighbor distance as lower limit. The embedding function should be evaluated within an intervall of $\rho = 0$ and several multiples of the equilibrium electron density. A reasonable number of supporting points should be computed (>5000).

In order to evaluate a tabulated function at a desired distance or electron density, a simple lookup-algorithm in combination with a first-order interpolation scheme is sufficient. Second-order interpolation schemes can improve the accuracy as compared to an analytical implementation further. Anyhow, considering the reproducibility of experimental quantities, a second order scheme does not yield a significant improvement.

EVALUATION OF DIFFERENT POTENTIALS: CALCULATION OF BULK PROPERTIES

The embedded atom method used in this work requires three functions: the electronic density, a pair potential and an embedding energy function, which depends on the local electron density. Although it is possible to use first-principle calculations to obtain such potentials, this approach is rather complex. Fitting a potential to various experimental findings is an alternative way. As this approach involves numerical optimization of many parameters it is also very time-consuming. Fortunately, parameterized potentials have been published in the last years. In the following, the concepts and the particular parameterization of those potentials are introduced. Furthermore, test methods to calculate bulk properties are presented and the different potential schemes are evaluated by comparing the results with experimental findings.

3.1 Introduction

Using well developed potentials in molecular dynamics simulation is the key to obtain reasonable results. Knowing the peculiarities of published potentials and their construction is helpful when evaluating these potentials. Two particular attempts to design an embedded atom potential are discussed: the initial approach of Daw and Baskes [30] and a more contemporary method presented by Zhou and co-workers [41]. Moreover, a discussion about creating appropriate pair potentials to simulate alloys is given.

3.1.1 The Original Potentials of Daw and Baskes

Daw and Baskes introduced the embedded atom method (Refs. [30,31]) and published their potential functions for Ni and Pd, respectively. An ab-inito approach is used to determine the electron densities. They refer to calculations performed by Clementi [101], who was using a single-determinant Hartree-Fock approximation to calculate the electron density of different elements. Since the exact ground-state is not known for an atom in the bulk (for Nickel it can be [Ar].3d^8.4s^2, [Ar].3d^9.4s^1 or [Ar].3d^{10}), a mixing procedure between s-like and d-like contributions was proposed.

$$\rho^{\mathrm{a}}(r) = N_{\mathrm{s}}\rho^{\mathrm{a}}_{\mathrm{s}}(r) + (N - N_{\mathrm{s}})\rho^{\mathrm{a}}_{\mathrm{d}}(r) \tag{3.1}$$

Here, $\rho^{\mathrm{a}}_{\mathrm{s}}$ represents the electrons in the s-state, whereas $\rho^{\mathrm{a}}_{\mathrm{d}}$ represents a density function of d-electrons. The number N_{s} gives the fraction of s-like density of the total atomic density, while the integer number N corresponds to the total number of electrons of both electrons in the 3s-state and 4d-state (for Ni).

The electron densities $\rho^{\mathrm{a}}_{\mathrm{s}}$ and $\rho^{\mathrm{a}}_{\mathrm{d}}$ can be calculated by the following equations:

$$\rho^{\mathrm{a}}_{\mathrm{s,d}}(r) = \left|\sum_i C_i R_i(r)\right|^2 / 4\pi, \tag{3.2}$$

$$R_i(r) = \frac{(2\xi_i)^{(n_i + 1/2)}}{[(2n_i)!]^{1/2}} r^{n_i - 1} e^{-\xi_i r} \quad . \tag{3.3}$$

The parameters C_i, ξ_i and n_i can be found in Ref. [101]. Parameters for Nickel from different authors are listed in section 6.2.1.

Beside the mixing rule for 4s- and 3d-electrons, the electron density function is a result from first-principle calculation. In contrast, the pair potential function $\phi(r)$ is modeled by a repulsive electrostatic interaction between atoms. It is constructed assuming a Coloumb potential (cp. section 6.2.1 and Ref. [30])

$$\phi(r) = \frac{Z(r)Z(r)}{r}, \tag{3.4}$$

with $Z(r)$ being the effective distance-dependent charge distribution of a screened atom. Daw and Baskes are using experimental values to fit the pair potential $\phi(r)$ and the embedding function $F(\rho)$. For example, the lattice constant, sublimation energy and elastic constants are used. The numerical representation of $Z(r)$ is given as a set of spline knots and results entirely from a fitting procedure to reproduce experimental values. The pair potential is normally short ranged (approaches zero within few nearest-neighbor distances). This is a benefit for numerical calculations, since only few neighbors have to be taken into account when calculating Eq. 2.49.

The embedding function $F(\rho)$ is also represented by a set of spline knots. Again, data to construct the function $Z(r)$ and the embedding function $F(\rho)$ can be found in section 6.2.1. Additionally, the embedding function, the pair potential and the electron density for Nickel is given as graph.

3.1.2 Embedding Atom Potentials by Zhou et al.

Zhou and co-workers [41] have published a complete set of embedded atom potentials for Cu, Ag, Au, Ni, Pd, Pt, Al, Pb, Fe, Mo, Ta, W, Mg, Co, Ti, and Zr, respectively. Those potentials are well-tested (with one exception - see Ref. [97] and section 6.2) and are suited for simulations incorporating multiple constituents. Recently, they investigated the interface formation between the different layers of a giant-magneto resistive device and compared them with 3D-atomic-probe experiments [41]. Furthermore, simulations of the growth of such multilayers have been published [42,8]. They also extended their potentials to cover metal-oxide systems to investigate tunneling magneto-resistive devices [40].

Contrary to the approach given by Daw and Baskes, where the pair potential is exclusively repulsive, a modified Morse-potential function was used to fit the pair potential.

$$\phi(r) = \frac{A\exp\left[-\alpha\left(\frac{r}{r_e}-1\right)\right]}{1+\left(\frac{r}{r_e}-\kappa\right)^{20}} - \frac{B\exp\left[-\beta\left(\frac{r}{r_e}-1\right)\right]}{1+\left(\frac{r}{r_e}-\lambda\right)^{20}} \tag{3.5}$$

Due to the specially constructed denominator, the potential is forced to very small values at larger distances r, which is again a benefit in simulations, as long as the cut-off radius is chosen efficiently large.

The electron density function $\rho(r)$ is given by

$$\rho(r) = \frac{f_e\exp\left[-\beta\left(\frac{r}{r_e}-1\right)\right]}{1+\left(\frac{r}{r_e}-\lambda\right)^{20}}. \tag{3.6}$$

Apart from the coefficient f_e, $\rho(r)$ is equal to the second term in Eq. 3.5. Again, the denominator forces Eq. 3.6 to values near zero for large distances. It should be noted that there is no link to ab-initio calculations with this approach. However, the functional shape of $\rho(r)$ is similar to the initially proposed electron density function.

The embedding energy function is given by three cubic equations for three different intervals: below, around and above the equilibrium electron density.

$$F(\rho) = \sum_{i=0}^{3} F_{ni}\left(\frac{\rho}{\rho_n}-1\right)^i \qquad \rho < \rho_n,\ \rho_n = 0.85\rho_e \tag{3.7}$$

$$F(\rho) = \sum_{i=0}^{3} F_{i}\left(\frac{\rho}{\rho_n}-1\right)^i \qquad \rho_n \le \rho < \rho_0,\ \rho_0 = 1.15\rho_e \tag{3.8}$$

$$F(\rho) = F_e\left[1-\ln\left(\frac{\rho}{\rho_e}\right)^{\eta}\right]\left(\frac{\rho}{\rho_e}\right)^{\eta} \qquad \rho_0 \le \rho \tag{3.9}$$

Here ρ_e denotes the equilibrium electron density. Sets of parameters to construct potentials for the elements Ag, Au, Co, Fe, Ni and Pt are given in section 6.2.2.

3.1.3 Modeling Alloys with the Embedded Atom Method

All three functions necessary to perform simulations utilizing EAM potentials are specific to a pure element, therefore there is no obvious extension to handle simulations involving more than one sort of atoms. Anyhow, the physical origin of the embedding function $F(\rho)$ lies in assuming a change of energy per atom, which depends on the electron density at the position of the considered atom without specifying the source of this density. That is to say, an atom experiencing a certain amount of ρ^{h} should exhibit the same embedding energy, no matter whether ρ^{h} is constructed from monoatomic sources or it is a superposition of electron densities arising from different atoms. Together with the restriction to consider only pair interactions, the accordant embedding function can therefore be used in alloys as well.

Abrahamson investigated different approaches to describe the interatomic potentials of binary noble-gas systems [36], which was later extended to potential functions for almost all elements [37]. Building the geometric mean $\phi^{\mathrm{AB}} = \sqrt{\phi^{\mathrm{A}}\phi^{\mathrm{B}}}$ of the potential functions ϕ^{A} and ϕ^{B} was found to give the best results. The symbols A and B refer to the two different elements which interatomic potential should be described. Using this approach in combination with Eq. 3.4 delivers

$$\phi^{\mathrm{AB}}(r) = \frac{Z^{\mathrm{A}}(r)Z^{B}(r)}{r}. \tag{3.10}$$

This method was used by Foiles and co-workers. They have developed a potential set for the fcc-elements Cu, Ag, Au, Ni, Pd and Pt by fitting the underlying effective charge functions [102] to describe any combination of the mentioned elements.

However, the method of calculating the pair potential using Eq. 3.10 works only well for monoatomic pair functions exhibiting positive values, i.e. which are repulsive for all distances. Using pair potentials which are attractive (i.e. negative) for a dedicated distance range can result in an imaginary potential and is thus not physical.

Apart from this problem, the total energy of a system described by Eq. 2.50 is invariant by the following concurrent transformations [38]:

$$\begin{aligned} &\rho^{\mathrm{a}}(r) \to s\rho^{\mathrm{a}}(r) \\ &F(\rho^{\mathrm{h}}) \to F\left(\frac{\rho^{\mathrm{h}}}{s}\right) \end{aligned} \tag{3.11}$$

and

$$\begin{aligned} &F(\rho^{\mathrm{h}}) \to F(\rho^{\mathrm{h}}) + g\rho^{\mathrm{h}} \\ &\phi(r) \to \phi(r) - 2g\rho^{\mathrm{a}}(r). \end{aligned} \tag{3.12}$$

Eq. 3.11 and Eq. 3.12 do not alter the total energy, thus g and s can be used as additional fitting parameters, when designing a monoatomic potential. What is useful in a monoatomic case, causes problems in a binary model. The scaling of the electron density function in Eq. 3.11 prevents a sensible construction of ρ^{h}, since in an alloy model ρ^{h} would then be a superposition of possibly differently scaled atomic electron densities (cp. Eq. 2.48). Moreover, transforming a single monoatomic potential yields a change in the binary pair potential (Eq. 3.10). Thus, the proposed interatomic potential ϕ^{AB} (Eq. 3.10) is not invariant by the transformation rules given above. Apart from these obvious problems, a comparison of different potentials for a single element is difficult due to the arbitrariness introduced by Eq. 3.11 and Eq. 3.12.

Johnson [39] proposed a transformation law for given monoatomic potentials to make them comparable buy claiming a vanishing first derivative of the embedding function at the equilibrium electron density,

$$\frac{\partial F}{\partial \rho}(\rho_{\mathrm{e}}^{\mathrm{h}}) = 0 . \tag{3.13}$$

Here, the equilibrium electron density is defined as being the superposition of all relevant atomic electron densities (i.e. contributions of atoms i within the cut-off radius):

$$\rho_{\mathrm{e}}^{\mathrm{h}} = \sum_{r < r_{\mathrm{cut}}} \rho_i^{\mathrm{a}}(r) \ . \tag{3.14}$$

Using Eq. 3.12 in combination with the condition given in Eq. 3.13 yields

$$g = -\frac{\partial F}{\partial \rho}(\rho_{\mathrm{e}}^{\mathrm{h}})$$

and thus

$$F^{\mathrm{norm}}(\rho^{\mathrm{h}}) = F(\rho^{\mathrm{h}}) - \frac{\partial F}{\partial \rho}(\rho_{\mathrm{e}}^{\mathrm{h}})\rho_{\mathrm{e}}^{\mathrm{h}} \tag{3.15}$$

Here, $F^{\mathrm{norm}}(\rho)$ denotes the new, transformed embedding function. The term “normalized potential” is commonly used in the literature when referring to this transformation scheme. All the potential functions discussed in section 3.1.2 are normalized and therefore applicable for comparisons with other normalized potential functions.

As a consequence, the pair potential is also changed (Eq. 3.12). If the system is in its equilibrated state, i.e. every atom experiences a host electron density of $\rho_{\mathrm{e}}^{\mathrm{h}}$, the pair potential is then the only driving force, since the terms involving the derivative of the embedding function in Eq. 2.54 vanish. $\phi(r)$ represents then an effective pair potential.

As already mentioned, constructing a pair potential for alloys by using the geometric mean of the monoatomic pair potentials breaks the invariance of the total energy function of the system. To overcome this problem, Johnson [39] has proposed a new way of constructing the necessary potential for alloy calculations:

$$\phi^{\mathrm{AB}}(r) = \frac{1}{2}\left[\frac{\rho^{\mathrm{a,\,B}}(r)}{\rho^{\mathrm{a,\,A}}(r)}\phi^{\mathrm{AA}}(r) + \frac{\rho^{\mathrm{a,\,A}}(r)}{\rho^{\mathrm{a,\,B}}(r)}\phi^{\mathrm{BB}}(r)\right]. \tag{3.16}$$

According to Eq. 2.50, the energy of a system consisting of atom A and B is given as (see also Ref. [39]):

$$\begin{aligned} E^{\mathrm{tot}} = {} & \sum_{i^{\mathrm{A}}} F^{\mathrm{A}}(\rho_i^{\mathrm{h}}) + \sum_{i^{\mathrm{B}}} F^{\mathrm{B}}(\rho_i^{\mathrm{h}}) + \frac{1}{2}\sum_{i^{\mathrm{A}},j^{\mathrm{A}}} \phi^{\mathrm{AA}}(r_{ij}) + \frac{1}{2}\sum_{i^{\mathrm{B}},j^{\mathrm{B}}} \phi^{\mathrm{BB}}(r_{ij}) + \\ & \frac{1}{2}\sum_{i^{\mathrm{A}},j^{\mathrm{B}}} \phi^{\mathrm{AB}}(r_{ij}) + \frac{1}{2}\sum_{i^{\mathrm{B}},j^{\mathrm{A}}} \phi^{\mathrm{BA}}(r_{ij}) \end{aligned} \tag{3.17}$$

If using the proposed alloy potential (Eq. 3.16), the total energy should be invariant by the following set of transformations:

$$\varphi^{\mathrm{AA}}(r) = \phi^{\mathrm{AA}}(r) - 2g^{\mathrm{A}}\rho^{\mathrm{a,A}}(r) \qquad G^{\mathrm{A}}(\rho^{\mathrm{h}}) = F^{\mathrm{A}}(\rho^{\mathrm{h}}) + g^{\mathrm{A}}\rho_{\mathrm{e}}^{\mathrm{h}} \tag{3.18}$$

$$\varphi^{\mathrm{BB}}(r) = \phi^{\mathrm{BB}}(r) - 2g^{\mathrm{B}}\rho^{\mathrm{a,B}}(r) \qquad G^{\mathrm{B}}(\rho^{\mathrm{h}}) = F^{\mathrm{B}}(\rho^{\mathrm{h}}) + g^{\mathrm{B}}\rho_{\mathrm{e}}^{\mathrm{h}} \tag{3.19}$$

$$\varphi^{\mathrm{AB}}(r) = \phi^{\mathrm{AB}}(r) - 2g^{\mathrm{A}}\rho^{\mathrm{a,A}}(r) - 2g^{\mathrm{B}}\rho^{\mathrm{a,B}}(r). \tag{3.20}$$

Applying the transformed potential functions yields an invariant total energy E^{tot}.

$$\begin{aligned} E^{\mathrm{tot}} = {} & \sum_{i^{\mathrm{A}}}\{F^{\mathrm{A}}\rho_i^{\mathrm{h}} - g^{\mathrm{A}}\rho_{i,\mathrm{e}}^{\mathrm{h}}\} + \sum_{i^{\mathrm{B}}}\{F^{\mathrm{B}}\rho_i^{\mathrm{h}} - g^{\mathrm{B}}\rho_{i,\mathrm{e}}^{\mathrm{h}}\} + \\ & \frac{1}{2}\sum_{i^{\mathrm{A}},j^{\mathrm{A}}}\{\phi^{\mathrm{AA}}(r_{ij}) + 2g^{\mathrm{A}}\rho^{\mathrm{a,\,A}}(r_{ij})\} + \frac{1}{2}\sum_{i^{\mathrm{B}},j^{\mathrm{B}}}\{\phi^{\mathrm{BB}}(r_{ij}) + 2g^{\mathrm{B}}\rho^{\mathrm{a,\,B}}(r_{ij})\} + \\ & \frac{1}{2}\sum_{i^{\mathrm{A}},j^{\mathrm{B}}}\{\phi^{\mathrm{AB}}(r_{ij}) + 2g^{\mathrm{A}}\rho_i^{\mathrm{a,A}}(r_{ij}) + 2g^{\mathrm{B}}\rho_i^{\mathrm{a,B}}(r_{ij})\} + \\ & \frac{1}{2}\sum_{i^{\mathrm{B}},j^{\mathrm{A}}}\{\phi^{\mathrm{BA}}(r_{ij}) + 2g^{\mathrm{A}}\rho_i^{\mathrm{a,A}}(r_{ij}) + 2g^{\mathrm{B}}\rho_i^{\mathrm{a,B}}(r_{ij})\} \end{aligned} \tag{3.21}$$

Assuming a symmetric alloy potential $\phi^{\mathrm{AB}} = \phi^{\mathrm{BA}}$ and using Eq. 3.14 proves the invariance of the total energy, i.e. Eq. 3.21 and Eq. 3.17 are identical. Therefore, Johnson's alloy potential is invariant under the given transformations.

However, since the electron function appears in Johnson's function, the functional shape of Eq. 3.16 can still be changed by choosing different scaling factors in Eq. 3.11. It is for this reason that constructing a pair potential for alloys is again a fitting task to experimental or ab-inito data for the alloy potential. If not available, a starting point for the scaling of the electron density function is to normalize them to deliver $\rho_{\mathrm{e}}^{\mathrm{h}} = 1$ and subsequently changing one of the scaling parameters of the electron density function.

3.1.4 Conclusion

It should be noted, that the scaling possibilities offered by the formulation of the embedded atom method loosens the link to the initially published underlying first-principle calculations for the electron density. If reviewed critically that early approach of calculating the electron density function by using Hartree-Fock wave-functions of free atoms [101] already comprised a weak degree of freedom to adjust the electron density: Since it is not exactly known which electronic state the system exhibits in a bulk system, the amount of 4s-state density and 3d-state density has to be adjusted in order to reproduce experimental values. Thus, using adjustable functions for the electron density generally is also a valid method. Aside from that, the fitting procedures used for the embedding function $F(\rho)$ rely on experimental values, which bears much more inaccuracy than the calculation of the electron density can show.

Constructing transformation-invariant pair potentials for alloys by using monoatomic potentials is possible. Since the electron density function can still be chosen arbitrarily, additional fitting is necessary. Thus, using well-tested published potentials for alloys is a convenient way to avoid the difficulties discussed above.

3.2 Calculation of Bulk Properties

A canonical ensemble in equilibrium is characterized by the minimum of the free energy:

$$F = E - TS \tag{3.22}$$

where F is the free energy, E the internal energy, T the temperature and S is the entropy. The temperature and the internal energy are well known in molecular dynamics simulation. It is the entropy which is not easily accessible. A possibility to obtain values for the entropy is to use a quasiharmonic approximation [44]. Here, a quadratic expansion is used to approximate the potential energy around the equilibrium lattice constant. The free energy F can then be written as the potential energy at the lattice constant and contributions from the vibrational modes of the solid.

$$F = E_0(a) + k_B T \sum_{\mathrm{k}, j} \ln 2\left(\sinh \frac{h\omega_j(\mathrm{k})}{4\pi k_B T}\right) \tag{3.23}$$

The second term in this expression contains contributions from the phonon frequencies ω_j. A method to calculate this quantities can be found in Ref. [45]. Minimizing Eq. 3.23 with respect to a at a given temperature yields the equilibrium lattice constant.

Morris and Ho [43] presented a different method to determine the entropy of a system using the correlation matrices of the coordinates. An upper bound of the entropy can then be expressed using determinants of the correlation matrix. Numerically, this approach is also challenging, since it involves the calculation of high dimensional determinants.

Anyhow, to calculate special properties like the lattice constant a_0 or the thermal expansion coefficient, other methods are employable. The pressure P of a simulated system can be monitored by utilizing Eq. 2.16. Since the pressure within a solid in an equilibrated state should be zero, the equilibrium lattice constant a_0 can be determined by finding a system volume V_0 which results in a vanishing value of P.

3.2.1 Equilibrium Lattice Constant a_0

The lattice constant a_0 is an easily extractable quantity in a molecular dynamics simulation. By setting up a simulation with constant volume and constant temperature, the resulting pressure can be plotted with respect to the volume. Using several different volumes at a given temperature, the condition $P(V) = 0$ is then used to identify the equilibrium volume. That is to say, the system is at its equilibrium volume when no internal pressure is measurable.

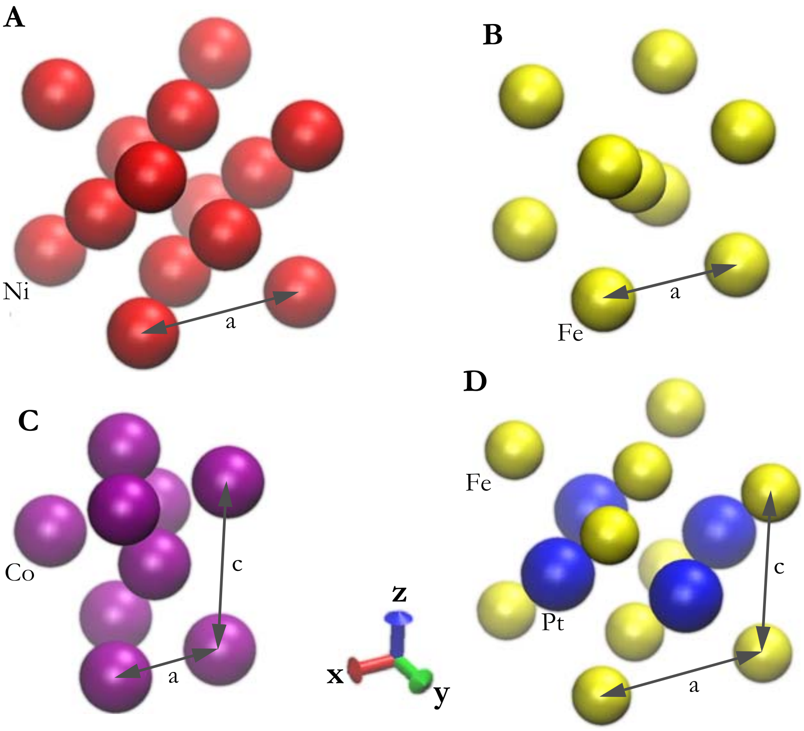

Figure 3.1: Four different crystal structures for the elements Nickel (A), Iron (B), Cobalt (C) and the alloy Iron-Platinum (D). The arrows indicate the lattice constant a and c.
At room temperature, Ni appears in the face-centered cubic structure (space group: Fm$\bar{3}$m, Pearson symbol: cF4, Strukturbericht designation: A1), Fe can be found in the body-centered cubic structure (Im$\bar{3}$m, cI2, A2), Co appears in hexagonal closed-packed form (P6_3/mmc, hP2, A3) and one of the possibilities for FePt is a face-centered tetragonal structure (P4/mmm, tP2, L1_0).

The elements of interest in this thesis are metals which appear in different crystal structures. Molecular dynamics simulations have to be set up in the corresponding crystal structure, since the underlying potentials have been fitted to these structures. In most cases the crystal is built by emulating the primitive cell. Anyhow, the simulation of a bulk system demands a sequel which can be periodically arranged. Comprehensive data for this purpose is available on the Internet [46,47]. Fig. 3.1 shows four different and commonly used structures in the molecular dynamics' coordinate system. Fig. 3.2 gives the pressure as a function of the primitive cell's volume of Nickel at $T = 10$ K. Several different potentials have been used. The intersection of the curve with the abscissa delivers an equilibrium volume of the cubic primitive cell. The lattice constant for a cubic crystal can then be calculated by using

$$a_0 = \sqrt[3]{4V_0}. \tag{3.24}$$

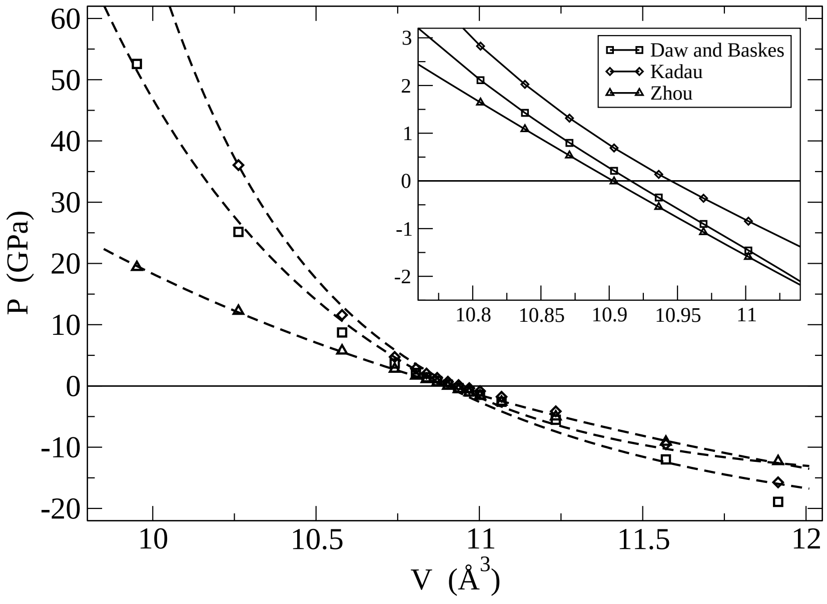

Figure 3.2: Comparison of the functional shape of $P(V)$ for three different potentials for Nickel (cp. section 6.2). Each symbol represents a NVT-MD simulation at a given volume and a constant temperature (10K). The inset shows the relevant scope of volumes where the pressure vanishes. Whereas the differences around V_0 between the three different potentials are comparably small, at smaller volumes (higher pressures) a significant discrepancy can be observed.

A total number of $N = 4000$ atoms has been used, the time-step in these simulations was $\Delta t = 1$ fs. A rough temperature setup was achieved by employing a velocity-scaling method during the first 2 ps of the simulation. After that, a Nosé-Hoover thermostat was utilized to equilibrate the system. The total simulation time was 140 ps, the pressure was determined by calculating the mean value during the last 60 ps. The cut-off radius was adjusted according to the different potentials used.

Using the first published embedded atom potential for Nickel (Daw and Baskes) delivers a_0 =3.521 Å, the modified version of this potential (Kadau) yields a_0 =3.524 Å and the potential published by Zhou et al. leads to a_0 =3.520 Å. All values are very close to the values used for the fitting procedure of the respective potentials.

It should be noted, that the method described above can be applied only to systems with a cubic structure. Since the pressure in a non-cubic crystal behaves anisotropically, the pressure tensor $P_{\alpha\beta}$ has to be employed to determine the equilibrium structure. The stress tensor is defined as

$$P_{\alpha\beta} = \frac{1}{V}\langle \sum_{i=1}^{N} m_i \dot{x}_{i\alpha}\dot{x}_{i\beta}\rangle + \frac{1}{V}\langle \sum_{i=1}^{N}\sum_{j<i}^{N} F_{ij\alpha}x_{ij\beta}\rangle \tag{3.25}$$

This matrix is linked with the ordinary expression for the pressure (Eq. 2.16) via the relation

$$P = \frac{1}{3}Tr(P_{\alpha\alpha}). \tag{3.26}$$

In case of Cobalt, the volume of the system is then not only a single parameter but it carries two other parameters, since Cobalt exhibits two lattice parameters a and c. That is to say, for a given lattice constant a_{Co} several lattice constants c_{Co} have to be calculated. Each simulation yields the pressures P_{xx}, P_{yy} and P_{zz}, which can be interpreted as the partial pressure at the according face of the volume. All three terms should be zero to deduce equilibrium, presumed to have small non-diagonal pressures.

Table 3.1: Equilibrium lattice constants for various elements in different crystal structures. The potentials used for these calculations are given in section 6.2.2. The values used for fitting are well reproduced.

element	crystal structure	a_0, sim. [Å]	a_0, fit [Å]	deviation [Å]
Ag	fcc	4.0900	4.0896	$0.3\cdot10^{-3}$
Au	fcc	4.0803	4.0896	$0.4\cdot10^{-3}$
Co	hcp	a = 2.5060 c = 4.0822	a=2.5060 n.a.	-
Fe	bcc	2.8690	2.8660	$3.0\cdot10^{-3}$
Ni	fcc	3.5210	3.5196	$1.4\cdot10^{-3}$
Pt	fcc	3.9200	3.9201	$0.1\cdot10^{-3}$

Table 3.1 lists the equilibrium lattice constant for Ag, Au, Co, Fe, Ni and Pt bulk at a constant temperature of 10 K. Although the values used for fitting are well reproduced, there is a mismatch with experimental data at this temperature. Interestingly, all known potentials are constructed using the *experimental* lattice constant at room temperature. This *experimental* lattice constant can only be reproduced when performing a simulation at very low temperatures. As a consequence, at higher temperatures the simulated lattice constants are estimated slightly too high. A solution for this problem would be to use the low-temperature lattice constants to fit the potentials.

3.2.2 Thermal Expansion Coefficient α

Most materials tend to expand with raising temperatures. A measure of this expansion is the linear thermal coefficient, which is defined as

$$\alpha = \frac{1}{a_{T=273K}} \frac{\Delta a(T)}{\Delta T} . \tag{3.27}$$

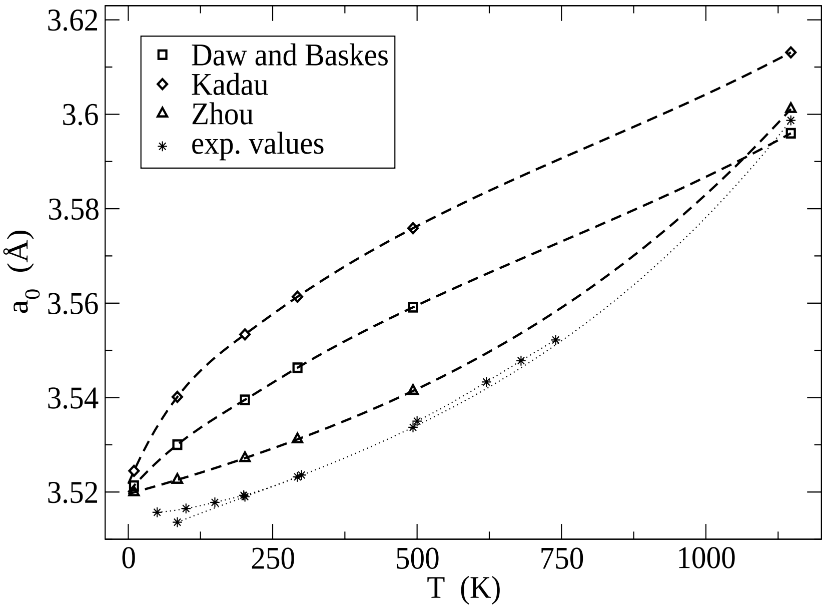

Figure 3.3: Lattice constant a as a function of the temperature for Nickel. In general, the potential proposed by Zhou et al. reproduces the experimental findings best. Anyhow, compared to experimental data, all three simulations tend to overestimate the lattice constant. The experimental data have been taken from Ref. [48].

To calculate the thermal expansion coefficient by means of molecular dynamics simulation, the equilibrium lattice constant has to be calculated at several different temperatures around $T=273$ K. Together with Eq. 3.27 these lattice constants are then used to calculate $\alpha_{T=273K}$ (cp. Table 3.2)

.

Table 3.2: Experimental and simulated linear thermal expansion coefficient for Nickel

	exp. value [49]	simul. value
α $[10^{-6}\ \mathrm{K}^{-1}]$	12.5	12.4

The thermal expansion does not depend linearly on the temperature, but can be approximated using Grüneisen's theory. In the case of ferromagnetic materials, this method is only valid for temperatures much smaller than the Curie-temperature. Below the Curie-temperature, the thermal expansion is mainly driven by the anharmonicity of the potential. When approaching T_c, the loss of magnetization is responsible for a further expansion of the volume. This additional increase in volume is reflected by a strong deviation from Grüneisen's formula (cp. Ref. [49]). Using molecular dynamics, this deviation can not be reproduced, since the current model does not include structural effects based on magnetism. Anyhow, the simulated thermal expansions coefficient for $T = 273$ K agrees well with experiments, since obvious magnetic effects can only be expected at temperatures around $T = 325$ K ([49]).

3.2.3 Bulk Modulus B_0

As a general rule, the bulk modulus B_0 is used in fitting algorithms to obtain embedded atom potentials. It is defined as:

$$B = -V\left(\frac{\partial P}{\partial V}\right)_T . \tag{3.28}$$

Since the pressure is known in molecular dynamics simulations, it is an easily available quantity. However, a different approach is being presented hereinafter[1]. In contrast to the Virial-equation, the pressure can also be defined by the thermodynamic relation

$$P = -\left(\frac{\partial E}{\partial V}\right)_S = -\left(\frac{\partial F}{\partial V}\right)_T . \tag{3.29}$$

Again, neither the entropy S can be held constant, nor is the free energy F known. However, if one performs MD calculations in the near-zero temperature regime, the free energy F can be approximated by the internal energy E. By the way, this approximation can be used to evaluate the pressure calculation within a code by comparing both methods to calculate the pressure.

Assuming a linear dependence of B on the pressure yields

---

[1] Parts of this derivation have been taken from Ref [50].

$$B = B_0 + B_0'P, \tag{3.30}$$

where B_0 denotes the bulk modulus at $P = 0$. Furthermore, B_0' is the derivative of B at zero pressure. This value is found to be nearly constant experimentally.
Combining Eq. 3.29 and Eq. 3.30 and integration from V_0 to V_1 delivers

$$\int_{V_0}^{V_1} \frac{dV}{V} = -\int_{P_0}^{P_1} \frac{dP}{B_0 + B_0'P}$$

$$\ln V_1 - \ln V_0 = -\frac{\ln(B_0 + B_0'P_1) + \ln(B_0)}{B_0'}. \tag{3.31}$$

P_0 represents the pressure at V_0 and is therefore zero per definition. Redefining $V_1 = V$ and $P_1 = P$ and reducing Eq. 3.31 results in an equation for the pressure:

$$P(V) = \frac{B_0}{B_0'}\left(\left(\frac{V_0}{V}\right)^{B_0'} - 1\right). \tag{3.32}$$

Since only the low-temperature regime is considered, the internal energy may be written as

$$E = E_0 - \int P(V)dV. \tag{3.33}$$

Integration of Eq. 3.32 yields

$$E(V) = E_0 + \frac{B_0 V}{B_0'}\left(\frac{(V_0/V)^{B_0'}}{B_0' - 1} + 1\right) - \frac{B_0 V_0}{B_0' - 1}. \tag{3.34}$$

The derivation of this equation of state was attributed to Francis Birch [51]. Since Eq. 3.34 contains three quantities at once, it is particularly useful to fit the energy with this expression to obtain V_0, B_0 and E_0. From V_0 the lattice constant of a given structure can again be calculated and compared with the method described in section 3.2.1. Fig. 3.4 depicts the dependence of the energy on the volume of the simulation for three different Nickel potentials. Additionally, a fit to Eq. 3.34 is given in the plot.

.

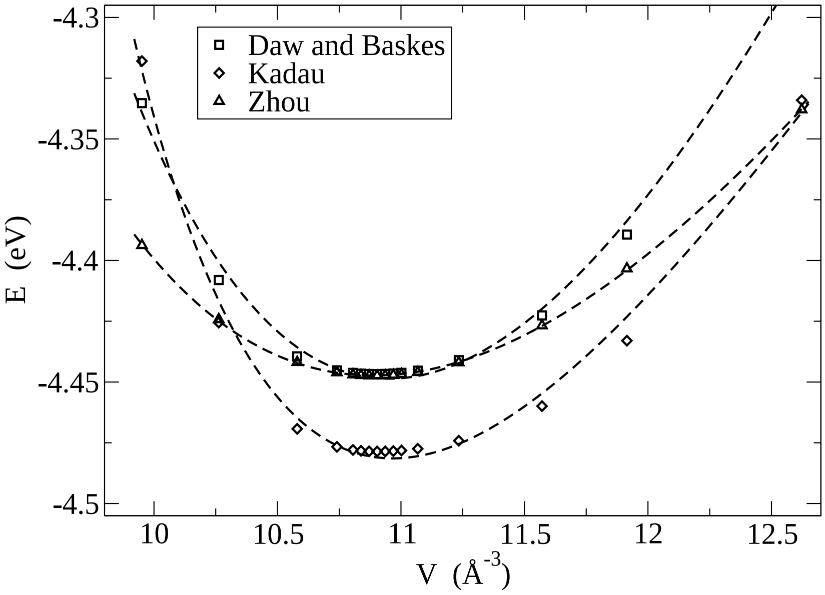

Figure 3.4: Energy per atom in dependence of the volume of the system. The temperature in these simulations was $T = 10$ K. Again, three different potentials were used. The dashed lines are fitting curves corresponding to Eq. 3.34.

Table 3.3 lists calculated values of the bulk modulus for different elements (Zhou potentials). Additionally, a different potential for Nickel was tested (denoted by Ni* in the table). Potentials published by Zhou generally delivered adequate values for the bulk modulus. Therefore, subsequent simulations were performed using these potentials.

Table 3.3: Simulated and experimental bulk moduli for various elements (potentials taken from [40]). The second value for Ni* was calculated using the proposed potential by Daw and Baskes and exhibits a strong deviation as compared to experimental values.

	B sim. [GPa]	B exp. [GPa]	dev. [%]
Ag	101	100	1.
Au	166	220	25.
Fe	166	170	3.
Ni	168	180	6.
Ni*	338	180	88.
Pt	282	230	23.

3.2.4 Sublimation Energy E_s

The sublimation energy E_s is defined as the energy an atom experiences in its equilibrium bulk structure in comparison to the free vacuum state. Once more, this quantity can be obtained by using Eq. 3.34. Table 3.4 compares experimental values with simulated energies. The results are consistent with experimental data

.

Table 3.4: Comparison between simulated sublimation energies and experimental results (potentials taken from [40]). Ni* denotes an alternative potential (cp. Tab. 3.3).

	E_S sim. [eV]	E_S exp. [eV]	dev. [eV]
Ag	-2.85	-2.96	0.11
Au	-3.93	-3.78	-0.15
Fe	-4.29	-4.28	-0.01
Ni	-4.45	-4.44	-0.01
Ni*	-4.45	-4.44	-0.01
Pt	-5.77	-5.86	0.09

3.2.5 Heat Capacity C_P

Materials show the ability to store heat when the temperature is increased. The heat capacity quantifies this ability. In experiments, the pressure of the system can be easily fixed while changing the temperature. In contrast, fixing the volume of a system is simple in simulations. Unfortunately, the heat capacity depends on these side conditions while changing the temperature, therefore two different definitions exist: C_P, which is the heat capacity obtained at a constant pressure and C_V, denoting the heat capacity at constant volume.

The definition of the C_P is given by

$$C_P = \left(\frac{\partial H}{\partial T}\right)_P , \qquad (3.35)$$

where H is the enthalpy of the system:

$$H = U + PV . \qquad (3.36)$$

Calculating a bulk system at several different temperatures at its equilibrium lattice constant (i.e. $P = 0$) is therefore a possibility to calculate C_P by means of molecular dynamics simulations. In this

special case, H reduces to the internal energy. Fig. 3.5 shows how the sublimation energy depends on the temperature. Extracting the slope of these functions yields the heat capacity C_P.
Simulation results can be found in Table 3.5. It should be noted, that again the potentials published by Zhou yield the best results.

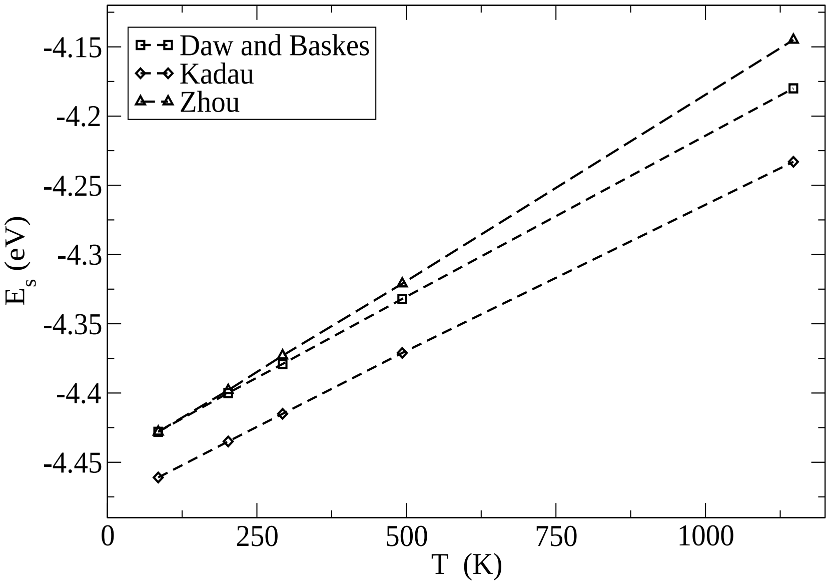

Figure 3.5: Sublimation energy of Ni for different potentials as a function of the temperature. E_s depends linearly on the temperature.

Table 3.5: Comparison of the experimental value of the heat capacity C_P for Nickel with the results obtained from different published embedded atom method potentials (cp. section 6.2).

	exp. value	Zhou	Kadau	Daw and Bases
C_P J/mol K	26.1	25.6	21.6	22.6

3.2.6 Equilibrium Properties of FePt

As discussed in section 3.1.3, the embedded atom method can be used to model alloys, presumed to use the respective potentials. Ultra-high density recording media consist of alloyed materials which are perfectly fitted to be described by the EAM. One of the most promising candidates for future recording applications is Iron-Platinum. FePt exhibits a complex phase diagram (Fig. 3.6) showing the

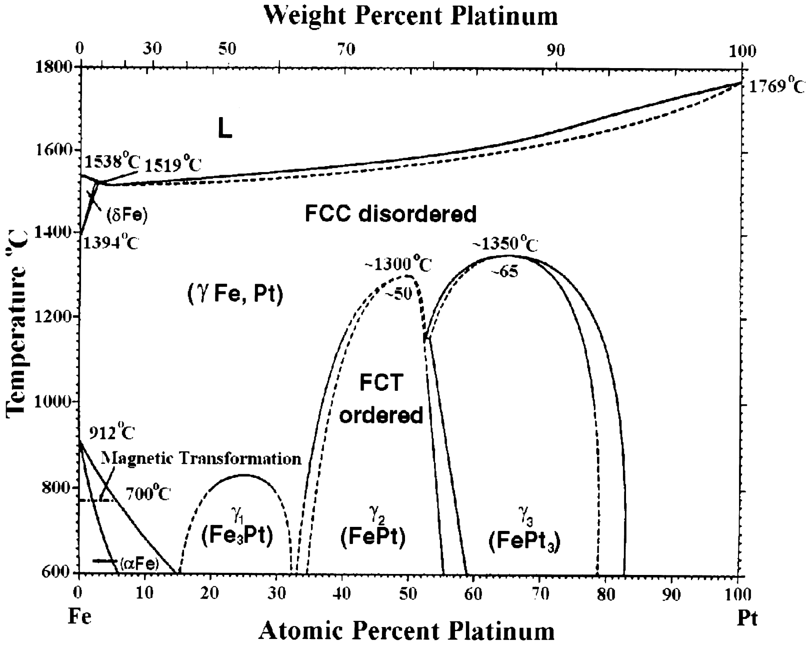

Figure 3.6: Phase diagram of FePt, taken from Ref. [52].

possibility of a phase transition from chemically disorderd face-centered cubic phase (fcc) to a chemically ordered face-centered tetragonal phase (fct, $L1_0$). Experimentally, self assembled arrays of monodisperse FePt nanoparticles can be prepared by solution phase chemical synthesis [53]. Sputtering techniques can be employed to prepare thin films of FePt [54] or nanoparticles [55].

Both methods yield FePt in a disordered fcc phase after preparation. The magnetically more interesting crystal phase is the chemically ordered fct phase, exhibiting a magnetocrystalline anisotropy of $K_u \cong 7 \cdot 10^6$ J/m^3. Thermal stability of a recording media depends on the product $K_u V$, with V being the volume of a magnetic grain. Thus, an increase of the areal storage density (smaller volumes) can be achieved by using materials with a high magnetocrystalline anisotropy. The maximum value of K_u was found to correspond to a maximum of tetragonality, i.e. a small c/a ratio [2].

The transition from the disordered fcc phase to an ordered fct phase is obtained by a thermal annealing process. Experimentally, after annealing the system at a temperature of about $T = 873$ K which is applied for several hours, the system can be found in the fct phase. Unfortunately, the experimental time scale makes a direct simulation by means of molecular dynamics impossible. Anyhow, molecular dynamics simulations permits the calculation of the equilibrium lattice constants of both, the disordered fcc phase and the ordered tetragonal phase.

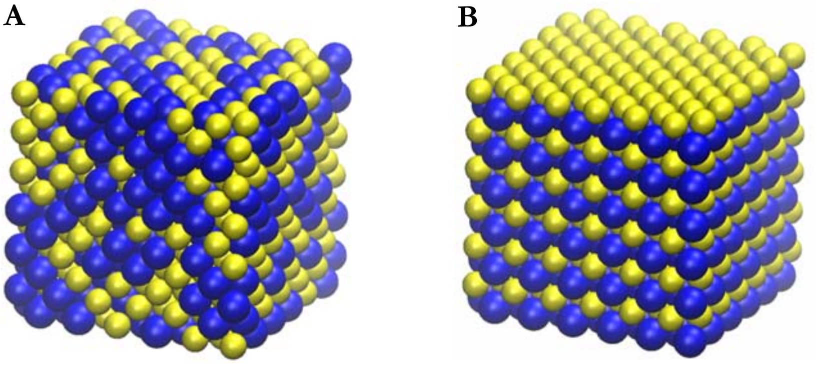

Figure 3.7: Atomic configuration for $Fe_{50}Pt_{50}$ in the disordered fcc phase (A) and the ordered face-centered tetragonal phase (B). The yellow spheres represent Fe, whereas the blue spheres depict Pt.

The calculation of the equilibrium lattice constants a and c of the ordered fct phase again involves variations of two parameters, as proposed for the equilibrium constants of Co. The lattice constants determined in this ways are listed in Table 3.6. In case of an ordered system, the ratio c/a is close to the experimental value. Comparing absolute values of c and a does not yield a satisfactory result. While the experimental lattice constant of the disordered phase was determined at room temperature, the simulation has been performed in the low temperature limit (T =10 K). This can be an explanation for the obvious deviation. However, the main feature comprised by the $L1_0$ phase of FePt could be reproduced: the c/a ratio is significantly smaller than unity.

Table 3.6: Comparison between experimental equilibrium lattice constants and simulation results for $Fe_{50}Pt_{50}$. The value indicating the tetragonality for the fct phase agrees well with experiments.

	a_{sim} [Å]	c_{sim} [Å]	a_{exp} [Å]	c_{exp} [Å]	c/a_{sim}	c/a_{exp}
fcc disordered[a]	3.686	N/A	3.841	N/A		
fct ordered[b]	3.751	3.606	3.87	3.73	0.961	0.964

a. exp. values taken from Ref. [48]
b. values taken from Ref. [2]

Additionally, the sublimation energy has been determined for both structures. The absolute energy difference between the two phases is small compared to the changes in the element specific sublimation energies. However, the mean sublimation energy of the $L1_0$-$Fe_{50}Pt_{50}$ system is slightly lower, indicating a preference for this phase as expected (cp. Table 3.7).

Table 3.7: Sublimation energies for Fe and Pt in a fcc disordered alloy and a fct configuration. Although Fe exhibits a lower sublimation energy in the disordered phase, the mean sublimation energy per atom in the fct phase is lower compared to the fcc phase.

	$E_{s,Fe}$ [eV]	$E_{s,Pt}$ [eV]	$E_{s,mean}$ [eV]
fcc disordered	-4.603	-6.149	-5.376
fct ordered	-4.471	-6.355	-5.413

3.3 Conclusion

The embedded atom method is well suited to describe bulk properties of metals. For the simulation of pure bulk materials sufficiently accurate potentials have been published. Compared to the test calculation necessary for benchmarking a potential, the fitting procedure to build a new EAM potential is much more complex.

In principle, the calculation of alloys can be achieved by combining monoatomic potentials. Although some of the potential degrees of freedom can be eliminated by normalizing the monoatomic descriptions, the pair potential function describing A-B interactions is not unique. For the most accurate results, specific fitting routines to create an alloy potential should therefore be performed. However, the used alloy model proposed by Johnson yields satisfying results. Anyhow, it is supposable to scale the monoatomic electron density function to get better accuracy. Since this scaling mechanism does not break the transformation invariance of Johnson's alloy model, it is a way to fit the pair potentials of an alloy model separately after the monoatomic functions have been determined.

STRUCTURE SIMULATION OF MAGNETIC NANOCLUSTERS

Detailed studies of the structure of magnetic nanoclusters are crucial for understanding their magnetic properties. Molecular dynamics simulations are used to investigate the formation of nanostructured materials. Special analyzing methods are introduced and employed to understand the resulting structures and their specific differences as compared to bulk properties. The developed methods are applied to a representative core-shell system (Co_xAg_{1-x}) and the simulation results are compared to experimental findings.

4.1 Introduction

Today, high density magnetic data storage on hard discs is based on granular magnetic media. The ongoing run for the highest areal storage density in magnetic recording industry results in magnetic structures becoming smaller and smaller. Obviously, the size of the magnetic grains is the key feature to achieve higher storage densities. However, the size of such particles is restricted by the superparamagnetic limit, marking a minimum volume per grain to store data magnetically. The long-time stability of recorded data depends on both, the magnetocrystalline anisotropy of the used material and the according volume of the grain. Therefore, using ultra-small particles requires a large magnetocrystalline anisotropy. Promising materials for this purpose are magnetic alloys in the $L1_0$ phase (FePt, CoPt, FePd). Long-term stability in magnetic storage applications means a stable magnetization of about 10 years. The minimum stable grain size can then be calculated by

$$D_g = \sqrt[3]{\frac{60 k_B T}{K_u}} . \tag{4.1}$$

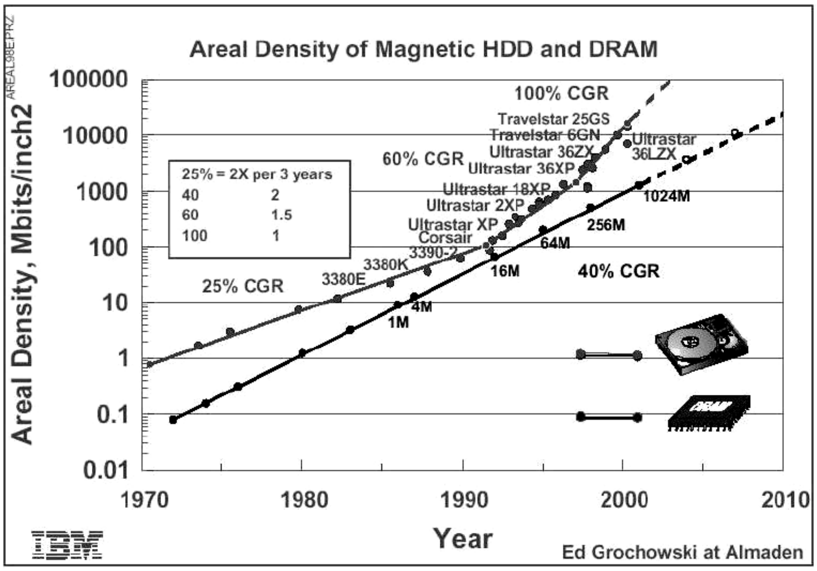

Figure 4.1: Development of the storage density for hard-disk and solid-state memory. Today, hard disks with 100 GBit/in² are produced. The ambition of an areal storage density of 1 TB/in² requires the use of novel materials and recording techniques (image taken from www.hgst.com).

Here T denotes the temperature and K_u is the uniaxial magnetocrystalline anisotropy. In case of FePt grains, the minimum stable grain diameter is 2.8-3.3 nm, making it a promising future candidate for ultra-high magnetic storage densities [1]. An atomic cluster with a size of only 2.8 nm consists of about 1000 atoms. Such clusters exhibit properties strongly deviating from the respective bulk properties. The high surface-to-volume ratio and the specific shape of such clusters influence the magnetic behavior. Material modeling has to take account of these size dependent effects. Therefore, such systems can not be described properly by continuum modeling techniques.

Not only the magnetic recording industry is interested in ultra-small particles. By using biocompatible magnetic systems, also a possibility for drug delivery is conceivable: attaching magnetic particles to drugs allows the specific local delivery of a given medication by magnetic fields. Biocompatibility includes prevention of the magnetic particles from coalescence, which would cause thromboses in the body. Naturally, due to the target application in the human body, preventing oxidation of such particles is also a necessity. On the useable length scales, oxidized materials such as Co, or Fe significantly change the magnetic properties which is of course unfavorable. Therefore, capping layers are used, which ideally do not alter the magnetic behavior and do not harm humans being treated by this method. Currently, FeAu particles are discussed as possible candidates for this purpose. Au is especially suited, because of it is “chemical inertness” and its “functionality with enzymes” [56]. Experimentally, the reverse micelle reaction is used to prepare FeAu particles [57,58]. The particle size can be controlled to create clusters from 5 nm to 30 nm.

Below, a simulation setup and the according analyzing methods to investigate different features of nanoclusters are described. Simulation results of the formation of a core-shell (Co_xAg_{1-x}) system are discussed and the differences in the crystal structure formation of small Co-particles are presented.

4.2 Simulation Method

In experiments, atomic clusters can be prepared in different ways. Whereas complex chemical processes are hard to simulate, the gas-phase formation of clusters can easily be mimicked by means of molecular dynamics simulations. In contrast to the simulation of a bulk, where the minimum image convention is used to emulate a bulk material by using images of the simulation geometry on the boundaries, cluster simulations have to be performed differently. The simulation box has to be large enough to prevent individual atoms to interact with surface atoms on the other side of the formation.

Ideally, the center of mass of the initial configuration should be in the center of the simulation box. The initial velocity distribution should yield a zero center of mass motion of the cluster. This prevents a collective motion of the cluster towards the simulation box' boundaries. Presumed to have a proper implementation of the minimum image convention, the motion of the aggregate atoms does not alter the simulation results, but it is more convenient for further geometric analyses to find the cluster in the middle of the simulation box.

The formation of the clusters is initiated by elevating the temperature to values high enough to touch at least the liquid phase of the investigated material. Subsequently, the temperature is lowered and the resulting geometry is analyzed. Although the center-of-mass motion and the rotation of the cluster can easily be suppressed by using appropriate distributions of the initial velocities, the final relative orientation of the crystallized cluster is arbitrary. Unfortunately, only the resulting crystal structure is of interest. For example, the magnetocrystalline anisotropy is related with the crystal structure, and its mathematical description assumes to have a material aligned in a global coordinate system. In case of a uniaxial anisotropy, one of the three axes of the coordinate system is at the same time the direction of the easy axis. In this respect, knowing and changing the resulting orientation of a cluster simulation is important.

To overcome this problem, two slightly different approaches have been implemented. If the final shape of a system is already known, some atoms have been chosen to act like anchors for the rest of the system. Those atoms were fixed in space, but did act like normal atoms, i.e. they contributed to the total potential energy of the system. Even if this method harms several physical laws, it perfectly suits the purpose to fix a known geometry in space while applying high temperatures. The method is adequate to simulate known geometries and investigate their mechanical stability in dependence of the temperature. While fixing some atoms is a quick and yet unphysical way, a better method is to determine the orientation of the particles after the calculation process.

The used analysis methods are described in detail in the next chapter.

4.3 Analyzing Methods

4.3.1 Radial Distribution Function

An important quantity when performing simulation analysis is the radial distribution function (RDF). It can be interpreted as the probability to find i's neighbor atom j in a distance r_{ij}. $g(r)$ is defined as

$$g(r) = \frac{\langle N(r, r + \Delta r)\rangle}{\langle V(r, r + \Delta r)\rangle}. \tag{4.2}$$

$\langle N(r, r + \Delta r)\rangle$ denotes the number of atoms within the volume shell between r and Δr, the denominator represents the volume of this shell. To increase the accuracy of the radial distribution function, more than one atom can be used to calculate $g(r)$. In case of multiple atoms, the definition given above has to be weighted with the number of considered atoms.
The radial distribution function can be easily compared with experimental findings. It is linked with the structure factor $S(\boldsymbol{k})$ by the following equation:

$$S(\boldsymbol{k}) = 1 + n\int(g(\boldsymbol{r}) - 1)e^{i(\boldsymbol{k} \cdot \boldsymbol{r})}d\boldsymbol{r}. \tag{4.3}$$

Here, $\boldsymbol{k}$ is the reciprocal lattice vector and n denotes the atomic density [59]. Experimentally $S(\boldsymbol{k})$ can be measured by electron scattering or neutron scattering. An example radial distribution function for fcc Ni and hcp Co at different temperatures is given in Fig. 4.2.

An advantage of the radial distribution function is that intuitive graphs can be produced. Information about the crystal structure is obtained by comparing them with RDFs from known structures. A drawback of this method is its dependence on the number of used atoms for calculation. That is to say, RDF functions of only a few hundred atoms can only deliver approximate mean values of the crystal structure.

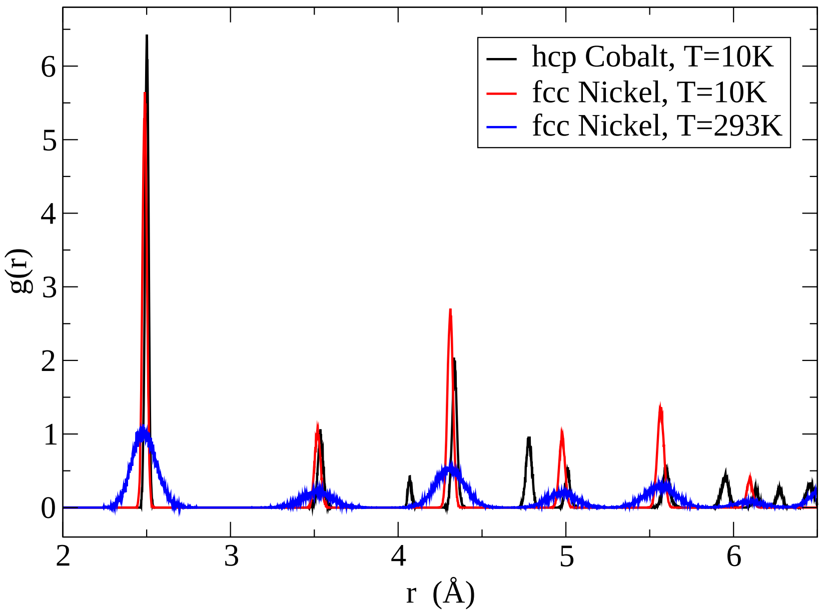

Figure 4.2: Radial distribution function for the crystal structure hcp (Co) and fcc (Ni) at a temperature of $T = 10$ K ($N = 4000$). Additionally, $g(r)$ for Ni was plotted at an elevated temperature ($T = 293$ K). In the low-temperature case, the relative position of atoms is well defined, whereas the peaks are broadened at higher temperatures, indicating stronger fluctuations of the positions. The resulting functional shape of the radial distribution function is specific to the underlying crystal structure. Thus, $g(r)$ can be used to determine the crystal structure of a simulation.

4.3.2 Tesselation Method

Usually, the output of a molecular dynamics simulation of a crystallized material are snapshots of the positions of the atoms. As long as the material is simulated below the melting temperature and periodic boundary conditions are used, it is likely that the atoms still remain near their initial positions. The crystal structure of such simulations can be easily determined by simply displaying the results with appropriate software [60,61].

The calculation of the formation of atoms building a cluster does not necessarily result in crystal structures known from their bulk configuration. Size dependent configurations can occur. Together with the unknown relative orientation of the final cluster a visual determination of the resulting structure is impossible. Even if the crystal axes were known, a mapping of the resulting positions onto assumed structures is difficult due to possible stacking faults.

Consequently, a method has to be employed which should be capable of determining the structure of clusters by local analysis. That means, the neighborhood of an atom is explored and evaluated. Patterns of possible atomic configurations are then quested leading to the identification of fractions similar to known bulk structures. This concept brings up the question about a precise definition of the local neighborhood of an atom. What comes first to one's mind is a simple next neighbor analysis by choosing a radius which defines surrounding atoms j as neighbors of atom i. In combination with an evaluation of the angles between atoms and a subsequent analysis scheme, this approach can deliver sufficient information to determine the structure of a cluster in detail.

A better and more precise definition of the neighborhood can be achieved by accomplishing a Voronoi tesselation of the given positions in space (cp. Fig. 4.3). Neighbors are defined as atoms which are sharing an edge (2D) or a facet (3D) in the tessellated graph, respectively. Thus, this method provides a good definition of the neighborhood of each atom. Furthermore, surface atoms can be recognized easily since surface atoms exhibit one opened facet (i.e. a facet with infinite area).

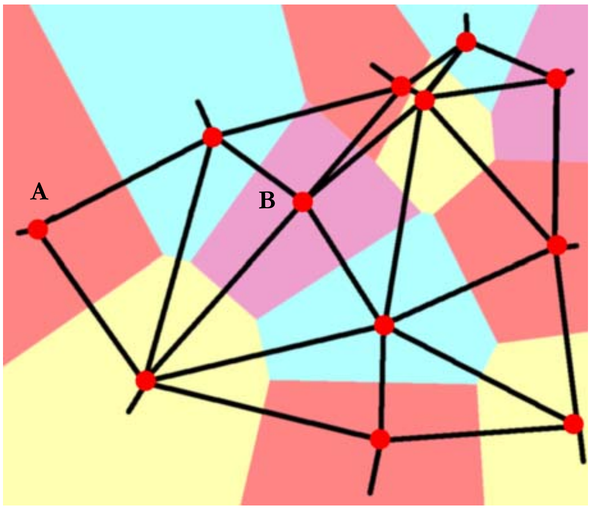

Figure 4.3: Voronoi tesselation of randomly distributed points in two dimensions. Points sharing an edge are neighbors per definition. Therefore, position A and B are not neighbors because they do not share a common edge.

Efficient free software is available to perform a Voronoi tesselation. In this work, parts of the software package Qhull [65] have been used and modified to fit the demands.

O'Malley has used a tesselation scheme to analyze the crystallization of atoms described by a hard sphere potential [66]. O'Malley and Snook investigated the nucleation process of a hard sphere potential system by means of a modified Voronoi tesselation [67]. The sharp definition of the neighborhood of an atom is especially helpful when working with geometry formations which are beyond the periodic structures of bulk materials. The application of the Voronoi tesselation for geometry analysis purposes is described on the basis of a specific nanocrystalline formation in Section 4.4.3.

4.4 The CoAg Core-Shell System

4.4.1 Experimental Results

CoAg is a highly investigated alloy system due to its specific formation process. CoAg nanoclusters can form a core-shell system with Co building the core and Ag segregating towards the surface, forming a capping layer for Co. Experimentally, the preparation of such clusters is performed by using laser vaporization with a gas phase condensation source (low energy cluster beam deposition - LECBD). Recently, Dupuis et al. [68] investigated the magnetic properties of single CoM (M= Ag, Pt) clusters by means of the microSQUID technique [69]. The clusters were embedded in different materials (Nb and MgO). The geometry of the resulting clusters was investigated by high resolution transmission electron microscopy (HRTEM). The mean diameter of the investigated clusters was between 3 nm and 4 nm. The shape of the prepared core-shell system exhibited the morphology of a truncated octahedron. The crystal structure of those particles was identified to be face-centered cubic.

The magnetic properties of experimentally investigated nanoclusters strongly depend on the embedding matrix used. Pure Co nanoparticles exhibit an interfacial alloying of some monolayers, when being embedded in a Nb matrix. This interfacial alloy is magnetically “dead”, i.e. it does not contribute to the effective magnetic volume [70]. In contrast, if Co is protected by a shell of Ag, the effective magnetic volume does not depend on the embedding matrix. Consequently, the blocking temperature of CoAg is higher (30K) as compared to CoNb (12K).

4.4.2 Simulation of a Core-Shell Formation

The embedded atom method can describe the bulk properties of Co and Ag and provides a well established theory to describe alloys. Therefore the formation of a core-shell system should yield similar results as compared to experimental measurements. Due to the fact that the experimentally necessary matrix (Nb) does not contribute to the magnetic properties (as long as Co is covered with Ag), it was not included in the simulation setup. However, in experiments the matrix is needed to fix the nanoclusters in space, whereas simulated clusters are not exposed to gravitation. Thus, fixing an atom in terms of molecular dynamics means removing the center of mass motion of the cluster. Starting from a completely random distribution of Co and Ag atoms, the clusters were heated up and subsequently cooled down. The initial temperature was set to 1300 K which was decreased in 20 K steps towards 100 K. At each temperature step $6x10^4$ integration steps (time step = 1 fs) were performed. The size of the resulting particles was 2.8 nm (864 atoms) in diameter. During the simulated annealing process, a clear segregation of the Ag atoms towards the surface of the Co-core was obtained.

4.4.3 Results and Discussion

Calculation of the Formation Process

Simulations were made at different Co-Ag ratios with a constant total number of atoms (864). After the annealing process, the clusters exhibited a shape similar to a truncated octaheadron. Annealing always resulted in a clear Co core and a Ag shell.

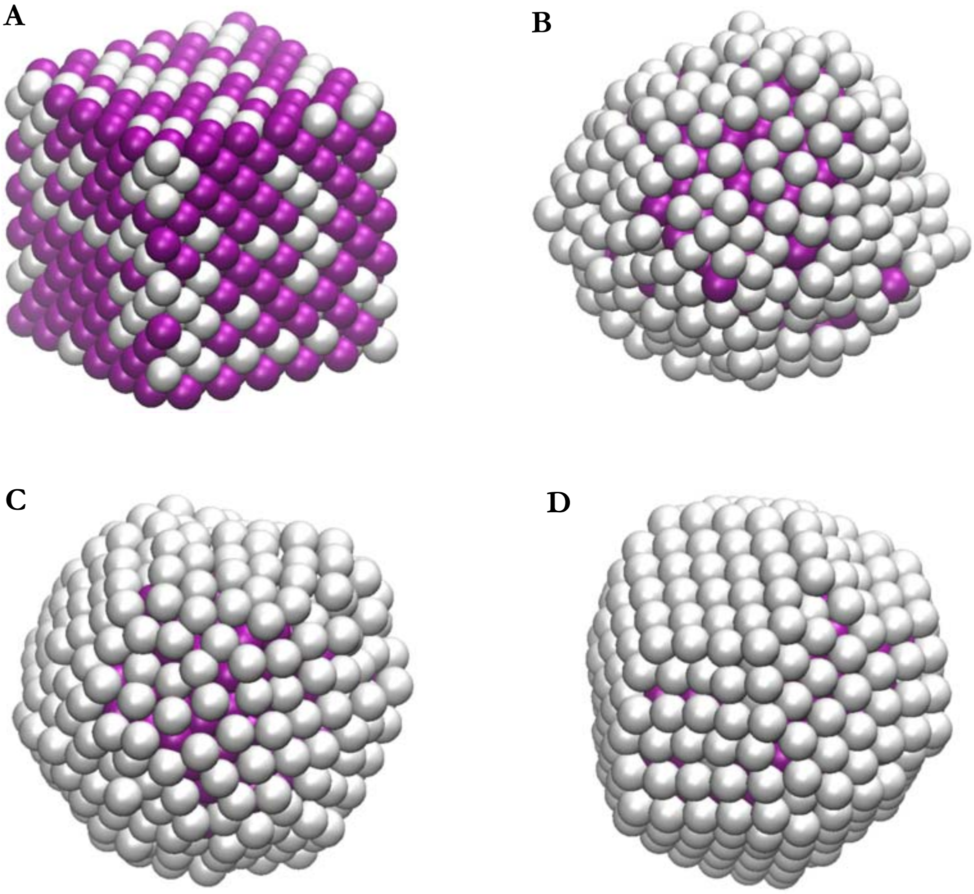

Figure 4.4: Snapshots taken during the simulation of the formation of a $Co_{65}Ag_{35}$ cluster, consisting of 864 atoms in total. (A) depicts the initial configuration with Co and Ag atoms randomly distributed on a fcc grid. (B,C) are snapshots at $T=1100$ K and 600 K, respectively. (D) displays the final configuration.

The segregation of Ag can be explained with the lower surface energy of silver (1.2 J/m^2) compared to cobalt (2.6 J/m^2) [68] and was found for similar systems as well [71]. Fig. 4.4 shows the initial configuration and three snapshots taken at $T=1100$ K, 600 K and 100 K for a $Co_{65}Ag_{35}$ system.

It should be noted that the segregation process occurs very rapidly after heating the particle. After a simulation time of 1 ns only few Ag atoms could be found within the Co core.

For a system consisting of a total number of 864 atoms, a relative concentration of at least 25% Ag atoms is necessary to cover the Co core completely with a monolayer Ag. Higher ratios of Ag yield a non-uniform coverage with a second monolayer of Ag. These second monolayers grow on the facets of the truncated octahedron.

Determining the atomic concentration in dependence of the distance from the center of the cluster yields a sharp transition from the Co-core to the Ag-shell (cp. Fig. 4.5). Not a single Ag atom could be found within the Co core.

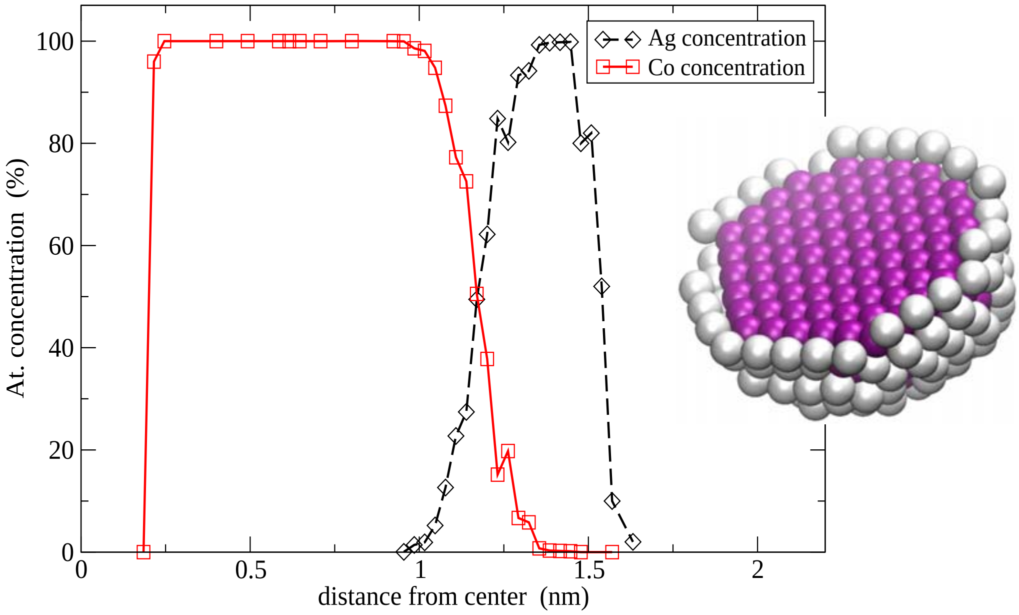

Figure 4.5: Atomic concentration of a CoAg cluster, measured from the center. A sharp transition between the Co core and the Ag shell occurs at 1.2 nm from the center. The inset on the right shows a $Co_{70}Ag_{30}$ cluster sliced along a (111)-plane.

Crystal Structure

In order to determine the crystal structure of the Co core, the stacking order has been investigated. As discussed previously, this can be either performed by calculating the radial distribution function of the resulting geometry or by using the more elaborate Voronoi tesselation scheme.

Fig. 4.6 shows the radial distribution function $g(r)$ of the atoms forming the Co core. Experimentally, CoAg core-shell systems were found to exhibit a clear fcc Co core, whereas the simulation shows the existence of peaks in the radial distribution function, which can be attributed to a partial hcp stacking order within the core. The appearance of a typical hcp peak at 4.1 Å and 4.8 Å is clearly visible. These peaks are missing in the fcc RDF of fcc bulk cobalt. Compared to the hcp bulk RDF, the ratio between the peaks at 4.8 Å and 5.0 Å of the Co-core is 1:1, whereas the peaks in the bulk hcp RDF exhibit a ratio of 2.5:1. This indicates a partial hcp-like structure in the calculated core-shell systems.

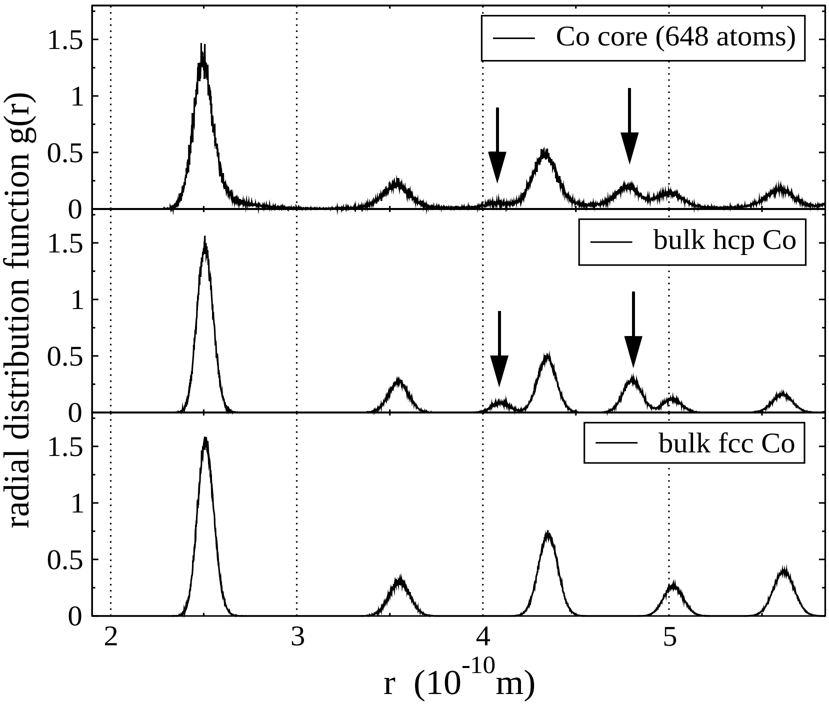

Figure 4.6: Calculated radial distribution function of the core of a $Co_{75}Ag_{25}$ cluster at 100K. Compared to the RDF of fcc Co, two additional peaks at 4.1 Å and 4.8 Å arise (see arrows). This is a clear indication for partial hcp stacking in the core.

The information provided by comparing the radial distribution function with known structures can only deliver mean values of the underlying structure. Applying a Voronoi tesselation yields a definition of the individual neighborhood of each atom, independent on the relative orientation of the cluster. After the tesselation of the cluster structure, a subsequent analysis including the detection of individual crystal planes has to be performed. Furthermore, a rotation of the particle towards a detected crystal axis is necessary to display the initially arbitrary orientated system from a known perspective. The tool used to perform all these tasks is described in section 6.3.3.

The analysis of the relative position of neighboring planes again yields a mix between the hcp and the fcc structure (cp. Fig. 4.7). Five planes exhibit an ABA stacking order, whereas four planes can be identified to exhibit an ABC stacking order. Whereas a fcc structure shows an ABC stacking order and a hcp structure exhibits an ABA stacking scheme, the cobalt core of the investigated core-shell systems did not show a unique stacking.

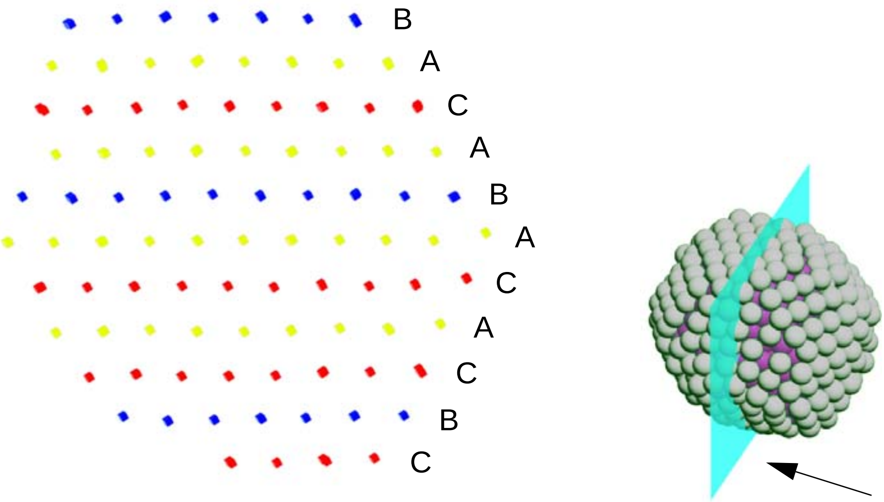

Figure 4.7: Left: Stacking order of the Co core (without the Ag shell) of a $Co_{70}Ag_{30}$ cluster. Right: The arrow indicates the line of sight with respect to the depiction on the left side. Whereas each plane A, B and C itself are perfect (111)-planes, the vertical stacking order does neither follow the fcc-stacking ABC nor does it follow a plain hcp-stacking AB.

The planes itself are almost perfect (111)-planes, only minor in-plane stacking faults occur. Fig. 4.8 depicts the individual crystal planes of a $Co_{65}Ag_{25}$ cluster. The center plane is given as inset. Although no clear stacking order can be determined along the splitting axis in Fig. 4.8 (cp also Fig. 4.7), in-plane stacking faults are rare.

Experimentally, the crystalline structure of the core of CoAg clusters was determined to be fcc [70]. Due to the fact that clusters in an experimental setup are prepared by a gas-phase adsorption method, the relaxation times and the atomic coalescence of such processes differ from the simulation setup presented in this work. Moreover, the initial temperature used in the simulations (1300K) is below the melting point of Co (1768K), which may result in an imperfect arrangement of the core. Thus, a direct comparison of a gas-phase-adsorption method and the results presented here is not valid. Nevertheless, the theoretical approach to simulate an annealing process with a relatively low initial temperature reveals the possibility of coexisting fcc- and hcp-like crystal phases.

Apart from the differences of the experimental setup with respect to the simulation process, the internal structure of nanocrystals may depend on the size of the system. The size of the simulated CoAg systems (D = 2.8 nm) was smaller than the experimentally investigated systems (D = 4.4 nm). The number of Co atoms was $N = 500$ in the simulation setup, whereas the experimentally determined Co count was $N = 1000$. A simulation of a large CoAg system ($N = 4000$) did show less stacking faults as compared to a system with $N = 864$. Unfortunately, simulating the annealing process at preferably small temperature steps and long time scales is numerically very time consuming. Thus, a systematic investigation of the dependence of the stacking fault density with respect to the system size could not be performed within a reasonable time.

The coexistence of both, hcp-like and fcc-like stacking may result in a different magnetic behavior compared to plain fcc cores. Lu and co-workers investigated the influence of stacking faults in perpendicular recording media [72,73]. To achieve a maximum magnetocrystalline anisotropy, a hcp stacking order is preferred. Chantrell et al. presented a micromagnetic model, relating the stacking fault density in perpendicular CoPt recording media to the effective reduction of the magnetocrystalline anisotropy [74]. The effective anisotropy decreases linearly with the amount of stacking faults. Moreover, the stacking fault density in CoPt increases with the amount of Pt.

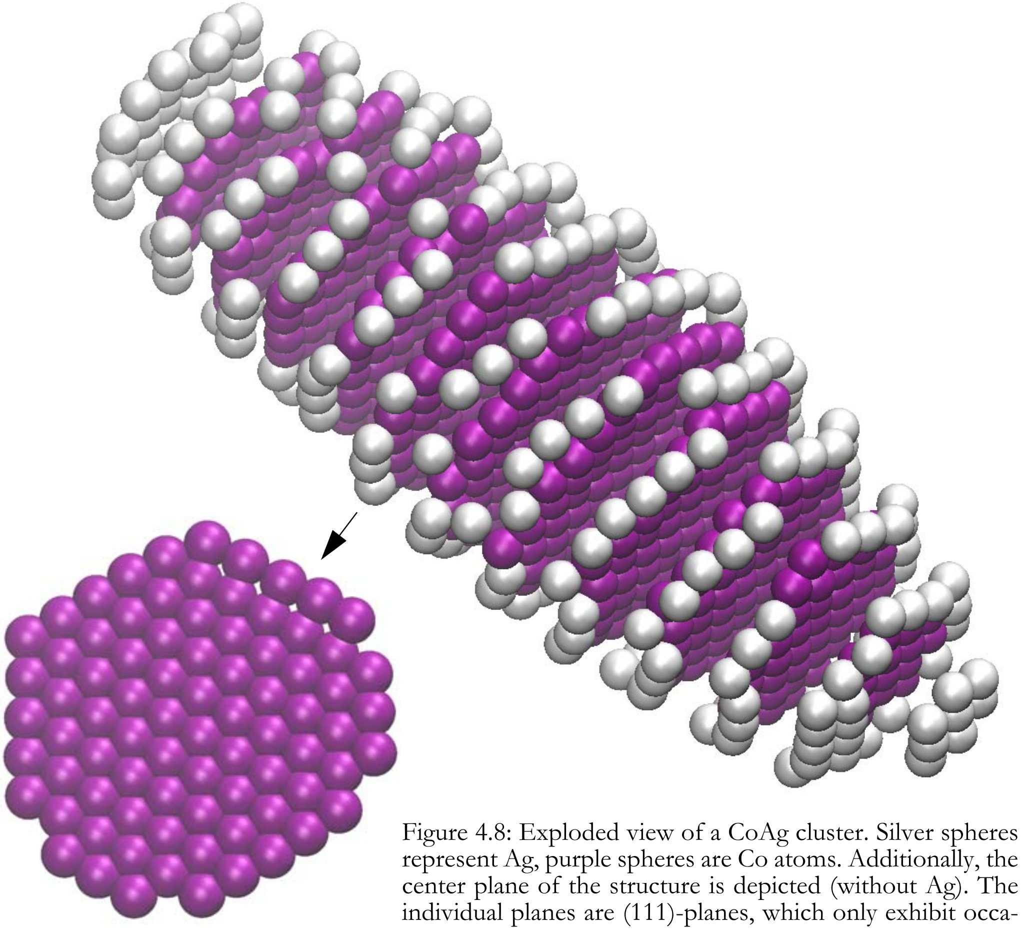

Figure 4.8: Exploded view of a CoAg cluster. Silver spheres represent Ag, purple spheres are Co atoms. Additionally, the center plane of the structure is depicted (without Ag). The individual planes are (111)-planes, which only exhibit occasional in-plane stacking faults.

Shape of CoAg Nanoparticles

Apart from the crystal structure, the shape of nanocrystalline particles is of special interest. The minimization of the surface energy of a given assembly of atoms yields specific shapes of the cluster. Wulff introduced a construction scheme describing the equilibrium shape of crystal structures by minimizing the free surface energy at a constant volume [75]. Herring presented thermodynamic studies based on Wulff's construction scheme [76]. Experimentally, nanoclusters of Gold atoms were the first materials which confirmed the predicted faceted morphology [77,78].

CoAg shows a shape similar to a truncated octahedron. A truncated octahedron exists of 36 edges and 24 apexes formed by 6 square facets and 8 hexagons. The simulation results in the same number of facets. Since the formation of a perfect truncated octahedron depends on an exact count of atoms, some facets covered by Ag exhibited in-facet stacking faults.

4.5 Summary and Outlook

Molecular dynamic simulations using the embedded atom method have been successfully used to calculate the crystal structure of binary magnetic nanoclusters. The peculiarities of such systems, including stacking faults and interfacial contribution to the magnetic anisotropy, have to be taken into account for the design of future applications of such clusters. MD studies can provide quantitative inputs for multi-scale magnetic simulations. Structural properties derived from the MD simulations can be used as input for magnetic simulations on a mesoscopic length scale.

MAGNETIC PROPERTIES OF NANOCLUSTERS

Nanoclusters behave differently as compared with the respective bulk material magnetic manner. The high surface-to-volume ratio substantially determines the magnetic properties. Thus, magnetic modeling of nanoparticles has to account for surface induced effects. Moreover, the fluctuation of the positions of the atoms are implicitly included in the magnetic description. This includes a fluctuation dependence of the magnetocrystalline anisotropy and a distance dependent formulation of the exchange interaction. The proposed models are tested and discussed on the basis of a standard model consisting of 1289 Co atoms showing the morphology of a truncated octahedron.

5.1 Introduction

In this chapter, a molecular dynamics approach is combined with an atomistic magnetic model. The introduced magnetic model is subsequently applied to a modeled nanocluster.

In section 5.2, the basics of magnetic modeling are discussed. The Landau-Lifshitz-Gilbert (LLG) equation is introduced, the energy contributions of an atomistic magnetic model are described and specific models to account for the fluctuation of the atoms are introduced. Moreover, the stochastic LLG equation and an integration method are presented.

In order to test the magnetic model, a representative nanocluster consisting of 1289 Co atoms is described (Section 5.3). Subsequently, simulations based on this standard geometry are carried out. The proposed magnetic models which implicitly couple the motion of the atoms with the magnetic model are investigated to evaluate their relevance. Effects arising from the surface anisotropy and magnetocrystalline anisotropy are presented in section 5.4. The influence of a long-range exchange formulation will be presented in section 5.5 and thermal effects are discussed in section 5.6.

5.2 Basics of Magnetism

The origin of magnetism in matter can be attributed to the quantum mechanical operators of the orbital momentum $\hat{\boldsymbol{L}}$ and the spin momentum $\hat{\boldsymbol{S}}$ [63]. Due to a quenching of the orbital momentum, $\hat{\boldsymbol{L}}$ can be neglected in most ferromagnetic materials [79], leaving $\hat{\boldsymbol{S}}$ as the main quantum mechanical operator to describe magnetic properties. $\hat{\boldsymbol{S}}$ can be related with the magnetic moment

$$\boldsymbol{m} = g_{\mathrm{L}}\mu_{\mathrm{B}}\frac{\hat{S}}{\hbar}. \tag{5.1}$$

Here, $g_{\mathrm{L}} = -2.0023$ is the Landé g-factor and μ_{B} denotes Bohr's magneton (cp. section 6.1.1). In Heisenberg's point of view, the states of a quantum mechanical system are time independent, but the mean value of an observable A is evolving in time, as described by the equation:

$$\frac{d}{dt}\langle A\rangle = \frac{1}{\mathrm{i}\hbar}\langle[A,H]\rangle + \langle\frac{\partial A}{\partial t}\rangle. \tag{5.2}$$

Here, H denotes the Hamiltonian of the system. The observable of interest is the magnetic moment $\boldsymbol{m}$, which is not explicitly time dependent. Thus, Eq. 5.2 can be written as

$$\frac{d}{dt}\langle\boldsymbol{m}\rangle = \frac{1}{\mathrm{i}\hbar}\langle[\boldsymbol{m},H]\rangle. \tag{5.3}$$

The Hamiltonian of this system is defined by the energy of the magnetic moment in a magnetic field $\boldsymbol{B}$:

$$H = -\boldsymbol{m}\cdot\boldsymbol{B} \tag{5.4}$$

After defining the gyromagnetic ratio $\tilde{\gamma} = (g_{\mathrm{L}}\mu_{\mathrm{B}})/\hbar$, the x-component of the commutator in Eq. 5.3 can be written as:

$$[m_x, H] = -\tilde{\gamma}^2[\hat{S}_x, \hat{S}_x B_x + \hat{S}_y B_y + \hat{S}_z B_z] = -\tilde{\gamma}^2(B_y[\hat{S}_x, \hat{S}_y] + B_z[\hat{S}_x, \hat{S}_z]) \tag{5.5}$$

Using the following commutator rule and Einstein's summation convention

$$[\hat{S}_i, \hat{S}_j] = \varepsilon_{ijk}\mathrm{i}\hbar\hat{S}_k \tag{5.6}$$

and performing a cyclic permutation of this result yields

$$[m_x, H] = -\tilde{\gamma}^2 i\hbar(\hat{S}_z B_y + \hat{S}_y B_z) \tag{5.7}$$

$$[m_y, H] = -\tilde{\gamma}^2 i\hbar(\hat{S}_x B_z + \hat{S}_z B_x) \tag{5.8}$$

$$[m_z, H] = -\tilde{\gamma}^2 i\hbar(\hat{S}_y B_x + \hat{S}_z B_y) \tag{5.9}$$

Using equations Eq. 5.1 and Eq. 5.3, we can obtain

$$\frac{d}{dt}\langle\boldsymbol{m}\rangle = -\tilde{\gamma}(\langle\boldsymbol{m}\rangle\times\boldsymbol{B}). \tag{5.10}$$

The next simplification includes the replacement of the expectation value $\langle \boldsymbol{m} \rangle$ by a classical magnetization $\boldsymbol{m}_{\text{at}}$. If each atom has a total angular momentum of $\hbar S$, the magnetic moment of an atom is given by

$$\boldsymbol{m}_{\text{at}} = g_{\text{L}} \mu_{\text{B}} S \boldsymbol{u} . \tag{5.11}$$

$\boldsymbol{u}$ is a unit vector pointing along the direction of the magnetic moment and S is the total spin quantum number. This formulation is particularly useful in numerical simulations, since the magnetization can be represented by a unit vector.

Using the simplifications described above together with Eq. 5.10 yields

$$\frac{\partial \boldsymbol{m}_{\text{at}}}{\partial \boldsymbol{t}} = -\gamma \boldsymbol{m}_{\text{at}} \times \boldsymbol{H}_{\text{eff}} . \tag{5.12}$$

Here, γ is the gyromagnetic ratio ($\gamma = \mu_0 \tilde{\gamma} = g_{\text{L}} 1.105 \cdot 10^5 \text{m/As}$, cp. section 6.1.1) and $\boldsymbol{H}_{\text{eff}}$ denotes an effective field acting on the magnetic moment. Eq. 5.12 describes an undamped precessional motion of a magnetic moment around the direction of the effective field. Unfortunately, no changes of the direction of the magnetization can be achieved by describing a system with this equation. In other words, the change of the magnetization direction has to be modeled by a phenomenological damping term. Gilbert proposed an additional damping term of the form

$$\frac{\alpha}{|\boldsymbol{m}_{\text{at}}|} \boldsymbol{m}_{\text{at}} \times \frac{d\boldsymbol{m}_{\text{at}}}{dt} . \tag{5.13}$$

Combining Eq. 5.12 and Eq. 5.13 yields the Gilbert equation

$$\frac{d\boldsymbol{m}_{\text{at}}}{dt} = -\gamma \boldsymbol{m}_{\text{at}} \times \boldsymbol{H}_{\text{eff}} + \frac{\alpha}{|\boldsymbol{m}_{\text{at}}|} \boldsymbol{m}_{\text{at}} \times \frac{d\boldsymbol{m}_{\text{at}}}{dt} \tag{5.14}$$

Multiplying this equation by $\boldsymbol{m}_{\text{at}}$ from left delivers $\boldsymbol{m}_{\text{at}} \cdot (d\boldsymbol{m}_{\text{at}}/dt) = 0$, which is equivalent to $d\boldsymbol{m}_{\text{at}}^2/dt = 0$. That is to say, the length of the magnetization does not change, only the direction is affected by Eq. 5.14. A schematic plot displaying the nature of the Gilbert equation is given in Fig. 5.1.

Unfortunately, Eq. 5.14 features a first order derivative on both sides of the equation. Multiplying $\boldsymbol{m}_{\text{at}} \times$ from left and using the identity $\boldsymbol{a} \times (\boldsymbol{b} \times \boldsymbol{c}) = \boldsymbol{b}(\boldsymbol{a} \cdot \boldsymbol{c}) - \boldsymbol{c}(\boldsymbol{a} \cdot \boldsymbol{b})$ gives

$$\boldsymbol{m}_{\text{at}} \times \frac{d\boldsymbol{m}_{\text{at}}}{dt} = -|\gamma| \boldsymbol{m}_{\text{at}} \times (\boldsymbol{m}_{\text{at}} \times \boldsymbol{H}_{\text{eff}}) - \alpha |\boldsymbol{m}_{\text{at}}| \frac{d\boldsymbol{m}_{\text{at}}}{dt} .$$

Substituting this result in the Gilbert equation leads to the Landau-Lifshitz-Gilbert equation:

$$\frac{d\boldsymbol{m}_{\mathrm{at}}}{dt} = -\frac{|\gamma|}{1+\alpha^2}\boldsymbol{m}_{\mathrm{at}} \times \boldsymbol{H}_{\mathrm{eff}} - \frac{\alpha|\gamma|}{1+\alpha^2}\frac{1}{|\boldsymbol{m}_{\mathrm{at}}|}\boldsymbol{m}_{\mathrm{at}} \times (\boldsymbol{m}_{\mathrm{at}} \times \boldsymbol{H}_{\mathrm{eff}}) \tag{5.15}$$

By integrating Eq. 5.15 the evolution of the magnetic moments can be calculated. The only unknown quantity remaining is the effective field $\boldsymbol{H}_{\mathrm{eff}}$. The effective field at an atom i can be obtained by the derivative of Gibbs' free energy in respect to the magnetic moment:

$$\boldsymbol{H}_{\mathrm{eff},\,i} = -\frac{1}{\mu_0}\frac{\partial E_{\mathrm{tot}}}{\partial \boldsymbol{m}_i}. \tag{5.16}$$

The different contributions to the total energy are described in the next chapter.

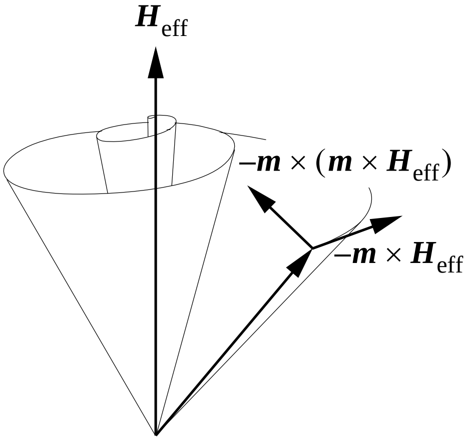
$\boldsymbol{H}_{\mathrm{eff}}$
$-\boldsymbol{m} \times (\boldsymbol{m} \times \boldsymbol{H}_{\mathrm{eff}})$
$-\boldsymbol{m} \times \boldsymbol{H}_{\mathrm{eff}}$

Figure 5.1: Motion of the magnetic moment in an effective field, described by the Landau-Lifshitz-Gilbert equation. (taken from Ref. [80]).

5.2.1 Energy Contributions in a Magnetic System

During an isothermal and isobaric change of a system, the Gibbs free energy E_{tot} is a minimum. The most relevant energy contributions in small magnetic systems are the exchange energy, the magnetocrystalline anisotropy, and the energy arising from an external field. Since the calculation of the strayfield energy is numerically very time consuming, it has been neglected in this work.

$$E_{\mathrm{tot}} = E_{\mathrm{ex}} + E_{\mathrm{ani}} + E_{\mathrm{ext}} \tag{5.17}$$

Exchange Energy

Heisenberg's model of exchange interaction is given by

$$E_{\mathrm{ex}} = -\sum_{i}\sum_{j \neq i} J_{ij}(\boldsymbol{r}_i - \boldsymbol{r}_j)\boldsymbol{u}_i \cdot \boldsymbol{u}_j . \tag{5.18}$$

$J_{ij}(\boldsymbol{r}_i - \boldsymbol{r}_j)$ denotes the exchange integral between spin i and spin j. Positive exchange values yield ferromagnetic ordering, whereas negative values of J_{ij} result in antiferromagnetic ordering.

In micromagnetic simulations with discretization length in the nanometer regime it is sufficient to account only for next neighbor interactions in Eq. 5.18. Indeed, exchange integrals often approach zero rapidly with increasing distance. Contributions of the exchange integral at distances larger than $r_{\mathrm{ex,max}}$ can therefore be neglected. That is to say, as long as the discretization length of a micromagnetic simulation is larger than $r_{\mathrm{ex,max}}$, the next neighbor approach is valid. In micromagnetic simulations the (minimum) discretization length is often determined by using the definition of the exchange length:

$$l_{\mathrm{ex}} = \sqrt{\frac{A}{K}} . \tag{5.19}$$

Here, A is the exchange constant and K is the anisotropy constant. Consequently, materials which exhibit a strong anisotropy (FePt) require small discretization lengths (e.g. 1 nm for FePt).

However, systems such as magnetic core-shell formations exhibit a typical size comparable to the exchange length. If described atomistically, the discretization length is naturally determined by the lattice constant, which is in general smaller than l_{ex}. Thus, describing exchange interactions on an atomic length scale by a next neighbor approach is not strictly valid.

Moreover, the exchange integral depends on the distance and orientation between atoms i and j. Micromagnetic simulations are performed on a discretized fixed grid. In combination with the next neighbor approach it is therefore possible to describe exchange interactions by an exchange *constant*. By contrast, in an atomistic simulation the positions of the atoms may be allowed to change due to thermal fluctuations. Ideally, the distance dependence of the exchange integral should be taken into account.

Unfortunately, the exchange integral $J_{ij}(\boldsymbol{r}_i - \boldsymbol{r}_j)$ can neither be obtained experimentally, nor is it easy to calculate J_{ij} as a function of distance. However, Bruno and co-workers have managed to calculate distance-dependent exchange parameters for Fe (bcc), Co and Ni (fcc). That is to say, the itinerant electron system is mapped onto an effective Heisenberg description of exchange interaction.

From the effective Heisenberg parameters J_{0j} quoted in Ref. [82] the spin stiffness constant can be calculated:

$$D_{\mathrm{sp}} = \frac{2\mu_{\mathrm{B}}}{3m_{\mathrm{at}}}\sum_{j} J_{0j} r_{0j}^2 . \tag{5.20}$$

Here, m_{at} is the magnetic moment per atom and μ_{B} denotes Bohr's magneton. The spin stiffness constant D_{sp} is related with the exchange constant A by the following relation [83]:

$$A = \frac{M_{\mathrm{s}} D_{\mathrm{sp}}}{2 g_{\mathrm{L}} \mu_{\mathrm{B}}} \tag{5.21}$$

In micromagnetic simulations it is the exchange constant A which is used as material parameter, therefore a direct comparison between experimental values of A and values obtained from the calculated exchange parameters J_{0j} is possible.

In case of Co and Ni, values of J_{0j} for 10 relevant distances are available, resulting in a summation of 176 atoms in case of a face centered cubic structure. If only the nearest neighbors are taken into account, the exchange energy of an atom is given by the interaction with the 12 next neighbors.

The values of the exchange parameters J_{0j} are given in dependence of both the direction and the distance between atom 0 and atom j. Hence, the formulation of a long-range exchange interaction has to take into account both the distance and the relative position for each atom. This would result in a function J_{ij}, delivering a value that depends on the relative position of atom i and atom j. Fortunately, the exchange parameters given by Bruno et al. are almost non-ambiguous with respect to the distance between atoms. That is to say, neighbor atoms at a given distance exhibit almost always the same value of J_{0j}. The positions $r_{0j} = (1.5; 1.5; 0)$ and $r_{0j} = (2; 0.5; 0.5)$ (in units of the lattice constant a_0) are the only exceptions. They are neighbors at the same distance but exhibit different exchange parameters. Since the value of the exchange parameter at this distance is only 50 times smaller than the most relevant contribution, it can be neglected. This simplification allows a description of J_{ij} as a function of distance rather than as a function of relative positions. Thus, J_{ij} can be estimated by a simple cubic spline approximation between the different quoted distances. The functional shape of this estimation as a function of distance for Co (fcc) is given in Fig. 5.2. It should be noted that J_{ij} turns negative at distances of about 5 Å and 6.5 Å, leading to a weak antiferromagnetic coupling. This feature will be missed if the exchange interaction is described by a nearest neighbor approximation only.

Discussion

The proposed method to describe long-range exchange interaction by simply connecting a few known points of the exchange integral was based on several assumptions:

The values of the exchange parameters were obtained by first principle calculations at T=0 K. The dependence of the exchange parameters on the temperature is not known. Therefore, the simulations are restricted to a low temperature regime ($T \ll T_{\mathrm{c}}$). Furthermore, the estimation of the functional shape by a simple cubic spline does not have any physical origin. Yet, this method allows for qualitative studies of effects arising from long-range exchange interaction in ultra-small magnetic systems.

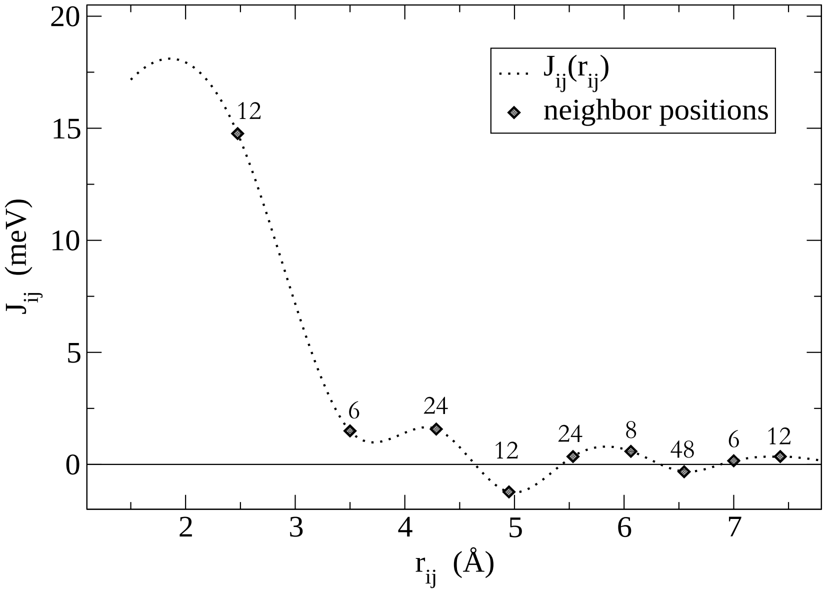

Figure 5.2: Estimated functional shape of J_{ij} as a function of the distance r_{ij} for Co. The symbols mark relevant neighbor distances, the numbers at the symbols represent the number of neighbors at the given distance.

Magnetocrystalline Anisotropy Energy

The magnetization in a ferromagnetic material can not be changed isotropically to arbitrary directions. Depending on the crystal structure and the considered material, the energy necessary to change the orientation of the magnetization depends on the direction with respect to the crystal axes. This effect is often illustrated by "easy directions" and "hard" directions. A common type of magnetocrystalline anisotropy energy is the cubic anisotropy, described by

$$E_{\mathrm{ani}} = K_0 V + K_1 V(\alpha_1^2\alpha_2^2 + \alpha_2^2\alpha_3^2 + \alpha_1^2\alpha_3^2) + K_2 V\alpha_1^2\alpha_2^2\alpha_3^2 . \tag{5.22}$$

Here, α_1, α_2 and α_3 are the directional cosines between the primitive lattice vectors and the magnetization. The dependence of the resulting easy and hard directions on the anisotropy constants K_0, K_1 and K_2 is given in detail in Ref. [81].

Since subsequent simulations are dealing exclusively with face-centered cubic Co which exhibits positive cubic anisotropy constants, the energy landscape for this situation is given in Fig. 5.3. The easy axes for fcc Co are aligned along the primitive cubic cells' crystal axes.

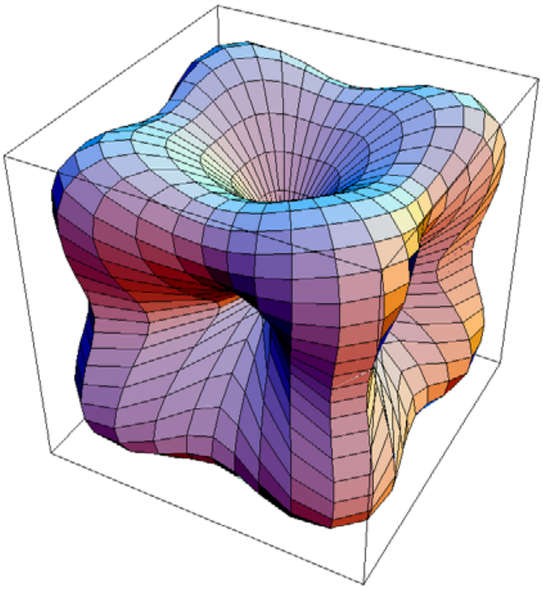

Figure 5.3: Energy landscape for a system exhibiting cubic anisotropy ($K_1 > 0$ and $K_2 > 0$). Easy directions are aligned along the [100], [010] and [001] direction.

In standard micromagnetic simulations, the positions of the individual magnetic moments are fixed in space. By contrast, if the motion of the atoms in an atomistic simulation is included in a micromagnetic simulation, it is arguable whether the use of global anisotropy directions in form of three constant directions is still a valid way to model magnetocrystalline anisotropy. Therefore, depending on the neighborhood of each non-surface atom, local cubic anisotropy directions can be determined by a very simple approach: A local analysis of the according next neighbors delivers anisotropy axes depending on the vibration of the neighbors. For example, the local [100] direction usually points towards the z-direction. Looking up the two next neighbors next to this direction and connecting this positions yield a local cubic anisotropy direction which is then used as the local [100]-direction. The same is performed for the local [010] and [001] direction, respectively. Since the exact position of the next neighbors is changing each time step, also the local anisotropy directions have to be updated at every integration step. Of course, since the proposed approach depends directly on the mean dislocation of each neighbor atom, it only works well at low temperatures.

The formulation of the cubic anisotropy energy is strongly linked to the crystal axes and the periodicity of the crystal itself. Therefore, surface atoms can not be described by Eq. 5.22. Neél has introduced a model capable of describing the surface anisotropy [89]:

$$E_{\text{ani,surface}} = -\frac{K_s}{2}\sum_i \sum_{j \in nn_i} (\boldsymbol{u}_i \cdot \boldsymbol{e}_{ij})^2 \ . \tag{5.23}$$

In dependence on the sign of the surface anisotropy K_s, the magnetic moments on the surface exhibit an easy direction either in-plane or out-of-plane. e_{ij} is a unit vector between position i and j:

$$\boldsymbol{e}_{ij} = (\boldsymbol{r}_i - \boldsymbol{r}_j)/|\boldsymbol{r}_i - \boldsymbol{r}_j| \,. \tag{5.24}$$

n_i is the number of nearest neighbors at atom site i. The value of the surface anisotropy constant K_s can be much higher than the corresponding cubic anisotropy constants (up to 15 times K_1 at room temperature [70]).

Zeeman Energy

The energy arising from an external field is given by

$$E_{\text{ext}} = -\mu_0 g_L \mu_B S \sum_i (\boldsymbol{u}_i \cdot \boldsymbol{H}_{ext}) \,. \tag{5.25}$$

5.2.2 Thermal Effects

In order to account for thermal effects in a magnetic system, a stochastic thermal field is added to the effective field $\boldsymbol{H}_{\text{eff}}$, as proposed by Brown [84]. The additional thermal field results in the stochastic Landau-Lifshitz-Gilbert equation:

$$\frac{d\boldsymbol{m}_{\text{at}}}{dt} = -\frac{|\gamma|}{1+\alpha^2}\boldsymbol{m}_{\text{at}} \times (\boldsymbol{H}_{\text{eff}} + \boldsymbol{H}_{\text{th}}) - \frac{\alpha|\gamma|}{1+\alpha^2}\frac{1}{|\boldsymbol{m}_{\text{at}}|}\boldsymbol{m}_{\text{at}} \times (\boldsymbol{m}_{\text{at}} \times (\boldsymbol{H}_{\text{eff}} + \boldsymbol{H}_{\text{th}})) \tag{5.26}$$

The thermal field should now mimic the influence of elevated temperatures on the magnetic moments. In a magnetic system, there are a lot of independent stochastic sources which may contribute to thermal effects. Independent stochastic processes yield a Gaussian random process (central limit theorem, cp. Ref. [85]).

The thermal field is therefore defined by its mean value and its second moment:

$$\langle \boldsymbol{H}_{\text{th}}(t) \rangle = 0 \,, \tag{5.27}$$

$$\langle H_{\text{th}_i}(t), H_{\text{th}_j}(t') \rangle = 2D\delta_{ij}\delta(t-t') \,. \tag{5.28}$$

Considering the last equation, neither spatial nor temporal correlations of the thermal field are given. The strength of the thermal field can be derived from the Fokker-Planck equation [86].

$$D = \frac{\alpha k_{\text{B}} T}{|\gamma| |\boldsymbol{m}_{\text{at}}| \mu_0} \tag{5.29}$$

5.2.3 Integration Method

Effective numerical methods are available to solve ordinary differential equations such as Eq. 5.15. For example, CVODE is a free software package which is capable of integrating the Landau-Lifshitz-Gilbert equation [91].

Unfortunately, the introduction of a stochastic quantity requires to utilize different methods. Scholz has investigated numerical methods to solve the stochastic Landau-Lifshitz-Gilbert equation [87]. Based on his work, a Heun integration scheme has been implemented.

In order to have a standard form of a Langevin equation, stochastic and deterministic parts are separated:

$$\begin{aligned}\frac{d\boldsymbol{m}}{dt} = & -\frac{|\gamma|}{1+\alpha^2}\boldsymbol{m}\times\boldsymbol{H}_{\mathrm{eff}} - \frac{\alpha|\gamma|}{1+\alpha^2}\frac{1}{|\boldsymbol{m}_{\mathrm{at}}|}\boldsymbol{m}\times(\boldsymbol{m}_{\mathrm{at}}\times\boldsymbol{H}_{\mathrm{eff}}) \\ & -\frac{|\gamma|}{1+\alpha^2}\boldsymbol{m}_{\mathrm{at}}\times\boldsymbol{H}_{\mathrm{th}} - \frac{\alpha|\gamma|}{1+\alpha^2}\frac{1}{|\boldsymbol{m}_{\mathrm{at}}|}\boldsymbol{m}_{\mathrm{at}}\times(\boldsymbol{m}_{\mathrm{at}}\times\boldsymbol{H}_{\mathrm{th}})\end{aligned} \quad . \tag{5.30}$$

For better clarity, the abbreviation $\gamma' = \gamma/(1+\alpha^2)$ is used.

Defining

$$A_i(\boldsymbol{m}, t) = \left\{-|\gamma'|\boldsymbol{m}\times\boldsymbol{H}_{\mathrm{eff}} - \frac{|\gamma'|\alpha}{|\boldsymbol{m}_{\mathrm{at}}|}\boldsymbol{m}\times(\boldsymbol{m}\times\boldsymbol{H}_{\mathrm{eff}})\right\}_i \tag{5.31}$$

and

$$\begin{aligned}B_{ik}(\boldsymbol{m}, t) &= -|\gamma'|\varepsilon_{ijk}m_j - \frac{\alpha|\gamma'|}{|\boldsymbol{m}_{\mathrm{at}}|}\varepsilon_{ijn}m_j\varepsilon_{nmk}m_m \\ &= -|\gamma'|\varepsilon_{ijk}m_j - \frac{\alpha|\gamma'|}{|\boldsymbol{m}_{\mathrm{at}}|}(\delta_{im}\delta_{jk} - \delta_{ik}\delta_{jm})m_jm_m \\ &= -|\gamma'|\varepsilon_{ijk}m_j - \frac{\alpha|\gamma'|}{|\boldsymbol{m}_{\mathrm{at}}|}(m_im_k - \delta_{ik}\boldsymbol{m}^2)\end{aligned} \tag{5.32}$$

and using Einstein's summation convention and the antisymmetric unit tensor ε yields

$$\frac{dm_i}{dt} = A_i(\boldsymbol{m}, t) + B_{ik}(\boldsymbol{m}, t)\boldsymbol{H}_{\mathrm{th}_k}(t) \, . \tag{5.33}$$

Eq. 5.33 still represents the stochastic Landau-Lifshitz-Gilbert equation, written in its Langevin form with multiplicative noise.

The Heun integration scheme is a two-step method to solve for $m_i(t+\Delta t)$. The first step (predictor step) can be interpreted as a simple difference scheme:

$$\overline{m}_i = m_i(t) + A_i(\boldsymbol{m}, t)\Delta t + B_{ik}(\boldsymbol{m}, t)\Delta W_k(t) \tag{5.34}$$

with

$$\Delta W_k = \int_t^{t+\Delta t} H_{\mathrm{th}_i}(t')dt' . \tag{5.35}$$

The second step (corrector step) yields the magnetization at time step $t + \Delta t$

$$\begin{aligned} m_i(t+\Delta t) &= m_i(t) + \frac{1}{2}[A_i(\overline{\boldsymbol{m}}, t+\Delta t) + A_i(\overline{\boldsymbol{m}}, t)]\Delta t \\ &\quad + \frac{1}{2}[B_{ik}(\overline{\boldsymbol{m}}, t+\Delta t) + B_{ik}(\overline{\boldsymbol{m}}, t)]\Delta W_k \end{aligned} . \tag{5.36}$$

Further details about the integration of the stochastic Landau-Lifshitz-Gilbert equation can be found in Ref. [86] and [87].

5.3 The Model System

The focus of this chapter lies on magnetic properties of nanoclusters. Unfortunately, experimental data of single atomic clusters are rare. Most publications are dealing with an assembly of thousands of clusters. As a consequence, the measured results are averaged values. However, some features of the measured nanoclusters can be extracted easily. The shape of Co clusters and their typical size can be determined by means of high resolution electron microscopy. Moreover, Jamet and co-workers developed a sophisticated measurement technique to extract magnetic properties of a single Co cluster [70].

Experimentally, the crystal structure of nanoparticles depends on both the diameter and the preparation procedure. CoAg clusters, prepared by using laser vaporization with a gas phase condensation source [low energy cluster beam deposition (LEBCD)] were found to exhibit a core in the fcc (β) crystal phase. By contrast, a size-dependent crystal structure distribution was found in synthesized Co particles by means of dc sputtering ranging from pure β-Co (2nm) to a nearly pure hcp (α)-Co structure (4 nm).

The surface of such small systems is of special interest when considering the effective magnetic anisotropy of such particles. Both the distribution of the facets on the surface and the crystalline phase distribution have a strong influence on the magnetic anisotropy. More information about the crystal structure of nanoparticles can be found in chapter 4.

One of the most interesting features of nanoclusters is their high surface-to-volume ratio. Thus, magnetic modeling of such systems should be focussed on effects attributed to the surface. For example, the formulation of the magnetocrystalline anisotropy on the surface is different from the core of a nanocluster. Moreover, due to its dependence on the neighborhood, the exchange energy at the surface is expected to be different as compared to the core. The morphology of the cluster is therefore a key feature in magnetic simulations of nanoclusters.

In order to investigate the influence of surface related effects, a model system consisting of 1289 Co atoms (3.2 nm diameter) in its fcc crystal phase is used. According to experimental findings and molecular dynamics simulations, the nanocluster exhibits the shape of a truncated octahedron. In this morphology, 482 atoms form the surface. Fig. 5.4 depicts the geometry of this cluster. It should be noted, that all following simulation results refer to this model geometry.

Although both molecular dynamics simulations and experimental measurements showed the possibility of partially irregular faceting, a perfectly faceted particle has been chosen to investigate the magnetic features. Irregular faceting of a nanocluster would introduce additional symmetry breaking on the surfaces, which makes the interpretation of results dependent on the specific geometry investigated. Therefore, using a perfect truncated octahedron allows for attributing effects to a well-defined morphology.

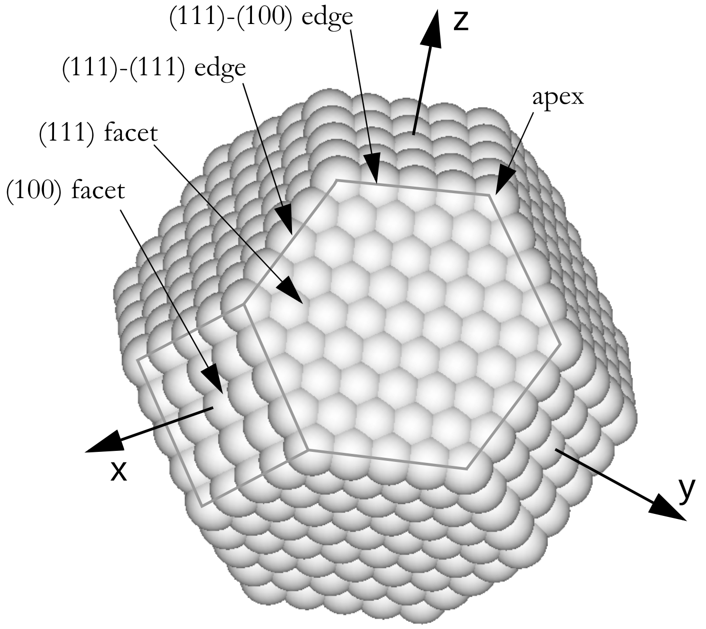

Facts and Figures:

- 482 surface atoms
- 8 (111)-facets
- 6 (100)-facets
- 24 apex positions
- 54 atoms on a (100)-surface (excluding edges)
- 296 atoms on a (111)-surface (excluding edges)
- 36 atoms form a (111)-(111) edge
- 72 atoms form a (100)-(111) edge

Figure 5.4: 1289 Co atoms forming a truncated octahedron. The surface-to-volume ratio is 482:807. Whereas in bulk materials this ratio can often be neglected, here the properties of the system are mainly determined by surface effects.

In order to investigate the influence of vibrational modes of the atoms in the nanocluster on the magnetic system, each atomic position is equipped with a magnetic moment. An important fact of the implementation of the combined model is that different contributions can be easily switched on and off, allowing to identify relevant contributions of a specific effect.

Following parameters were used, unless otherwise noted: At each Co position a magnetic moment with $m_{\mathrm{at}} = 1.6\ \mu_B$ is positioned. This leads to a spontaneous magnetic polarization of $J_s = 1.74$ T. The anisotropy constants of non-surface atoms are $K_1 = 7 \cdot 10^5$ J/m³ and K_2 $1.8 \cdot 10^5$ J/m³ (taken from Ref. [83], low temperature values). In case of a short range exchange interaction, an exchange constant of $A = 1 \cdot 10^{-12}$ J/m has been used. The value of the surface anisotropy constant was taken from [70] $K_s = -15 \cdot 10^6$ J/m³. All the quoted values refer to bulk Cobalt. Since material constants for nanoparticles are not available, using bulk material parameters is a good starting point. Finally, for efficiency reasons the damping constant α has been set to unity. The motion of the atoms was simulated by means of molecular dynamics (cp. chapter 2), the embedded atom potential for Cobalt has been taken from Ref. [33].

5.4 Surface Anisotropy in Nanoclusters

5.4.1 A First Test

In order to get a feeling whether the combination of two models which are only weakly coupled can deliver reasonable results, a simple approach to test for possible effects arising from the surface anisotropy has been calculated in collaboration with Richard Evans and Roy Chantrell from the University of York.

In this first test, two atomic configurations were used to calculate the effective anisotropy energy landscape. The first snapshot represents the model system as depicted in Fig. 5.4, the second snapshot was taken after a molecular dynamics simulation performed at 25K (5x10^5 integration steps). The morphology of the cluster did not change during the equilibrium process.

For non-surface atoms a simple uniaxial magnetic anisotropy was assumed.

$$E_{\mathrm{ani}}^{\mathrm{core}} = -K_c(\boldsymbol{u}_i \cdot \boldsymbol{e}_z)^2 \tag{5.37}$$

Here, K_c is the magnitude of the core uniaxial magnetocrystalline anisotropy, $\boldsymbol{u}_i$ is a unit vector pointing along the magnetic moment and $\boldsymbol{e}_z$ is the unit vector along the z-axis. The surface anisotropy was simulated assuming the Néel model applied to an atomistic spin system with Heisenberg-type exchange (nearest neighbor model). The value of K_s was about 15 times larger than K_c.

The energy landscape of the particles was calculated using the Lagrangian multiplier technique [90]. The method essentially involves adding a corrective field into the spin Hamiltonian to constrain the net magnetization of the overall spin system to lie along an arbitrary direction. The spin system is then allowed to relax to a minimum energy state and the energy of the magnetic configuration is calculated. The average spin direction is mapped onto spherical polar coordinates and the energy calculated for angles of θ (core easy axis) and φ (rotation) giving the energy surface of the nanoparticle. In a uniaxial case the minima in the energy surface will be at $\theta = 0°$ and $\theta = 180°$. Changes in the crystal arrangement and the spin configuration will in general give a more complex energy surface, often with different maxima. The energy barrier for a magnetic reversal can be calculated from the energy surface by taking the minimum energy path between two minima, thus giving an indication of the magnetic stability of the particle.

Results and Discussion

The energy surface plot of a truncated octahedron particle cut from a bulk crystal without any further annealing is shown in Fig. 5.5. It can be seen that the particle has an overall uniaxial anisotropy, but with additional features near the energy maximum. Correlating these features with the geometry of the particle reveals that the square facets correspond to local minima, while the edges of the hexagonal planes correspond to local maxima. This leads to a minimum energy path with the magnetization moving along the edges of the particle.

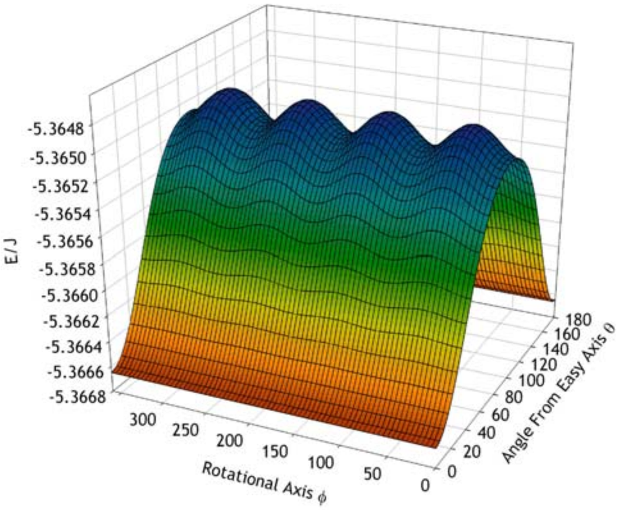

Figure 5.5: Energy landscape of a perfectly truncated Co octahedron without annealing (static system). The system shows an overall uniaxial anisotropy with minor deviations coming from the facets of the particle.

A similar energy surface plot of the simulated annealed particle is shown in Fig. 5.6. Here, the energy surface is highly asymmetric, arising from the deviation of the atoms from their mean position. This also leads to an increase in the effective energy barrier in the annealed case of about 10% compared with the particle cut from a bulk crystal with a static structure. The energy barrier increases from 2.80 $k_\mathrm{B}T$ to 3.11 $k_\mathrm{B}T$ at a temperature of 298 K.

Since only a single snapshot at an elevated temperature has been used to determine the energy landscape, the increase of the energy barrier with increasing fluctuations of the atoms can not be claimed as a general rule. However, this first test revealed a strong influence of the surface anisotropy on the magnetic behavior.

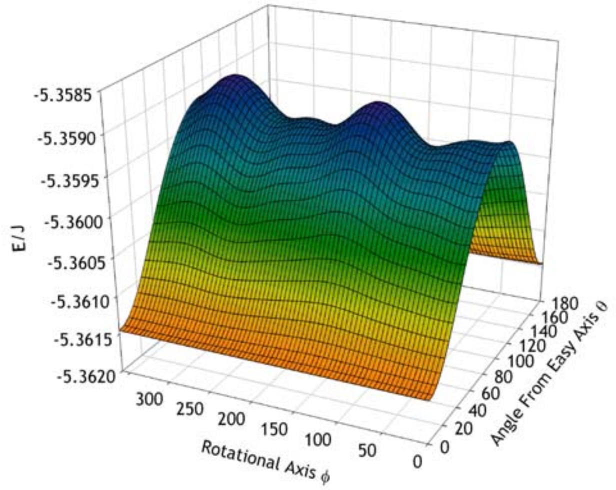

Figure 5.6: Energy surface for a simulated annealed core of a CoAg system.

5.4.2 Surface Anisotropy and Saturation Polarization J_S

In order to understand the influence of the surface anisotropy, the dependence of the saturation polarization J_S with respect to the value of K_S has been investigated. The sign of K_S determines whether the effective anisotropy direction on the surface lies in-plane (positive value of K_S) or out-of-plane (negative value of K_S). Therefore, the saturation magnetization depends on the surface anisotropy. Fig. 5.7 shows the two different magnetic configurations at $T = 0$ K. The direction of all moments was set to z-direction initially. The magnetic system was then equilibrated at zero field. Depending on the sign of the surface anisotropy constant, magnetic moments on the facets of the cluster show a pronounced non-uniform behavior. The inhomogeneities arise from the surface anisotropy. Since the individual atoms are exchange-coupled, also non-surface atoms are affected. Thus, the common assumption that small nanoparticles can be described by a homogenous magnetization is not strictly valid.

Chen and co-workers investigated Co nanoparticles prepared by a microemulsion method (average diameter 3.3 nm) [92]. They found out that the particles could not be saturated entirely, even at an external field of $B_{\text{ext}} = 5.5$ T (measurements were performed at $T = 2$ K). Assuming a non-homogenous distribution of magnetic moments, inhomogenities arising from the surface anisotropy allow for a further increase of the saturation magnetization when applying strong fields. An external field results in a more homogenous magnetization within the cluster.

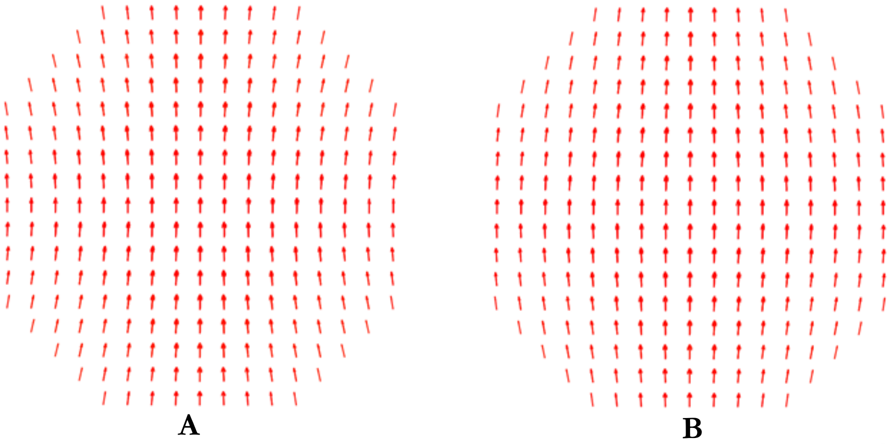

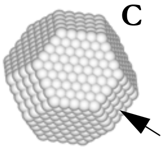

Figure 5.7: Equilibrium magnetic configuration in dependence of the value of the surface anisotropy constant K_S at T=0 K. (A) shows the configuration simulated with K_S=-15 MJ/m^3. (B) was calculated with K_S=15 MJ/m^3. Negative values of K_S lead to surface moments preferring an out-of-plane direction whereas positive values yield an in-plane surface anisotropy.
(C) indicates the point of view (along the y axis)

To illustrate this behavior, the z-component M_z of the total magnetization is given as a function of K_S in Fig. 5.8. Both positive and negative values of the surface anisotropy constant yield a decrease of M_z due to the non-uniform magnetic moments at the surface of the cluster.

However, surface anisotropy alone can not explain the observed inhomogenities of the magnetic configuration. It is the specific faceting which allows for a pronounced out-of-plane behavior of surface magnetic moments.

Additionally, the same simulation has been performed at non-zero temperatures (T=50 K). The temperature introduces fluctuating atomic positions. Since the Neél model relates the surface energy with the relative positions of neighboring atoms, an implicit coupling between the motion of the atoms and the magnetic system can be expected. In order to investigate this feature exclusively, temperature effects have been switched off in the magnetic part of the simulation. That is to say, the thermal field has not been taken into account in the integration of the Landau-Lifshitz-Gilbert equation. In contrast to zero temperature simulations, there is no well-defined equilibrium configuration. Thus, the results have been averaged over 10^5 integration steps.

The introduction of fluctuations of the atomic positions results in a further decrease of the z-component of the magnetization. This feature is a direct consequence of the Neél model: Energetically, the most favorable state of a surface atom can be achieved when all neighbors of this atom lie on a plane (apart from neighbor atoms beneath the surface). This lowest energy configuration is disrupted by the motion of the atoms. Consequently, the surface magnetic moments fluctuate, yielding a lower magnetization in z-direction.

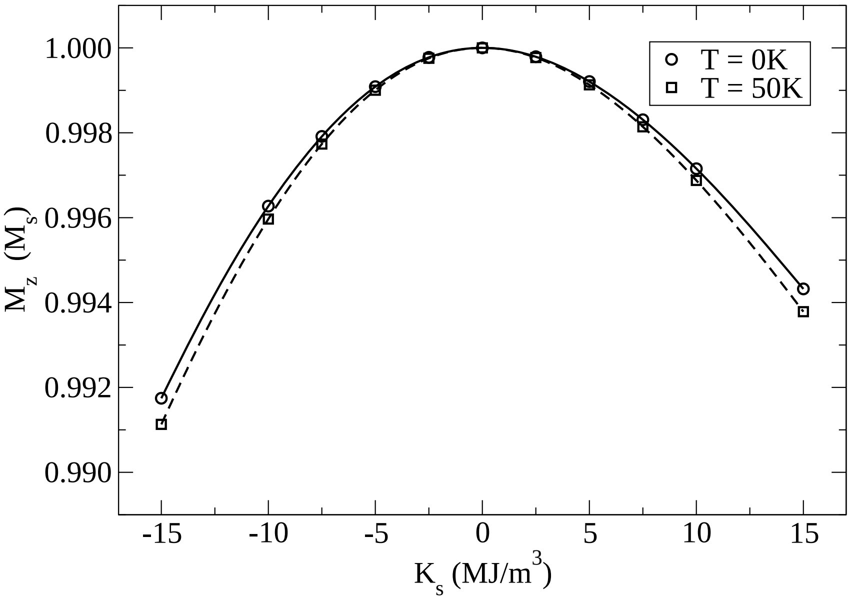

Figure 5.8: Magnetization M_z as a function of the surface anisotropy constant K_s. The surface anisotropy introduces a inhomogenous magnetic configuration resulting in a decrease of M_z. Furthermore, the effect of implicit coupling between the vibrations of the surface atoms at elevated temperatures is depicted (dashed line).

5.4.3 Anisotropy in Nanoclusters and its Impact on the Coercive Field H_c

In a nanocluster two main anisotropy contributions exist: the surface anisotropy and the magnetocrystalline anisotropy of non-surface atoms. In addition to a high surface-to-volume ratio the surface anisotropy yields a coercive field mainly determined by the surface anisotropy.

Fig. 5.9 shows one side of a hysteresis loop for the standard model at $T = 0$ K. Whereas a simulation with a surface anisotropy constant of $K_s = -15$ MJ/m³ delivers a coercive field of about $\mu_0 H_{c,\,\mathrm{dyn}} = 1.13$ T, a calculation with neglected surface anisotropy shows only $\mu_0 H_{c,\,\mathrm{dyn}} = 0.55$ T. That is to say, the effective anisotropy is significantly increased by the surface energy. It should be noted that the external field was changed rapidly in order to decrease the required CPU time. Fast changing external fields lead to an increase in the coercive field. Therefore, the quoted values of the coercive field do not correspond to values gathered from experiments.

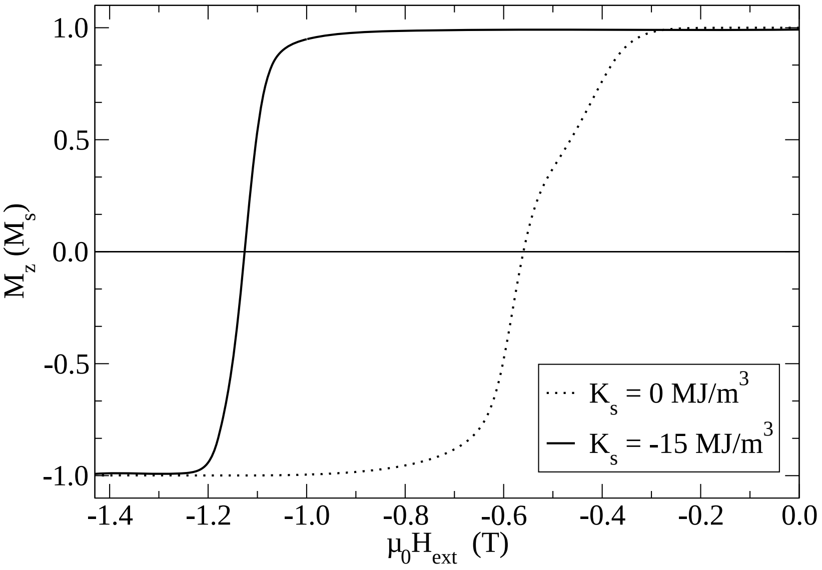

Figure 5.9: Dependence of the dynamic coercive field on the surface anisotropy constant. Contributions arising from the surface anisotropy are primarily determining the dynamic coercive field.

A similar increase of the coercive field with surface anisotropy was found in micromagnetic simulations of small magnetic particles by Zhang and co-workers [93,94]. In contrast to the simulations of Zhang, the combined molecular dynamics and magnetization dynamics simulations presented here include the motion of the surface atoms with time.

The model describing surface anisotropy implicitly couples the motion of the atoms with the magnetic model, introducing additional fluctuations into the magnetic model. In addition to surface effects, a method defining the local cubic anisotropy axes within the particle core has been introduced. This leads to a change of the local anisotropy direction with time which accounts for the motion of non-surface atoms. To study the implicit coupling between magnetic and atomic models, the simulation has been repeated at an elevated temperature (100 K). The thermal field has again been switched off to account exclusively for effects attributable to fluctuations arising from the motion of the atoms.

Fig. 5.10 shows the simulated demagnetization curve for both, a simulation including the introduced anisotropy fluctuations and a calculation with fixed anisotropy axes. Although the introduced fluctuations reduce the dynamic coercive field, the effect is rather small. A decrease in $\mu_0 H_{c,\mathrm{dyn}}$ from 1.13 T to 1.12 T can be observed.

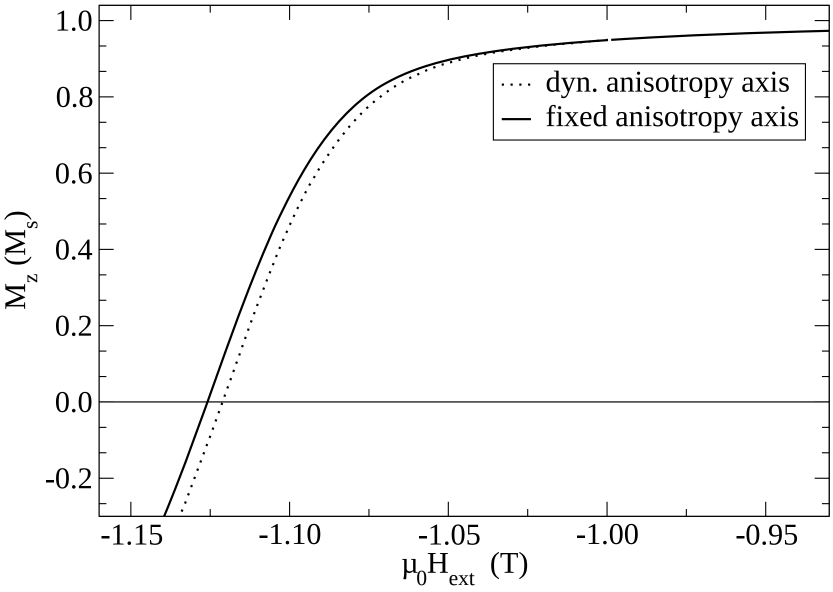

Figure 5.10: Dynamic coercive field in dependence of fluctuating local anisotropy axes. The introduction of magnetic fluctuation introduces only minor changes of the coercive field.

5.5 Influence of Long-Range Exchange on H_c

As proposed in section 5.2.1, a long-range exchange formulation has been introduced to the magnetic model. In the long range exchange formulation not only nearest neighbor atoms but all atoms within a certain radius contribute to the exchange energy of a specific atom. Within the short-range exchange formulation only the contribution of next neighbors is added to the exchange energy of an atom. The coordination number of surface atoms is smaller than the coordination number of atoms in the core. Thus, for the surface atoms the exchange energy is smaller than for all the other atoms. All but the surface atoms have a coordination number 12 in a face-centered cubic crystal. However, if more than the next nearest neighbors contribute to the exchange energy of an atom, surface effects are not only seen in the outermost shell of atoms but are extended to atoms at inner shells. With long range exchange interactions, surface atoms have a significantly different exchange energy than atoms in the core. A similar but smaller difference in exchange energy will be seen between atoms in the second shell and atoms in the core. The number and relative location of neighbors that contribute to exchange energy for an atom in the second shell is different from those of an atom in the core. Considering a long range exchange formulation, much more atoms show a different exchange energy as compared to a site far away from the surface. In order to make the short-range exchange formulation and the long-range exchange formulation comparable, the two models yield the same exchange energy for fully coordinated sites.

Fig. 5.11 depicts site-dependent exchange energies. The exchange energy per atom is shown in a plane of the model system for both, the short-range exchange model and the long-range exchange formulation. As expected, sites on the surface exhibit a lower exchange energy compared to atoms within the particles. For the short-range exchange formulation only the atoms in the outermost shell show a smaller exchange energy. In contrast, for the long-range exchange formulation the reduction of the exchange energy at the surface extends over more than one shell of atoms.

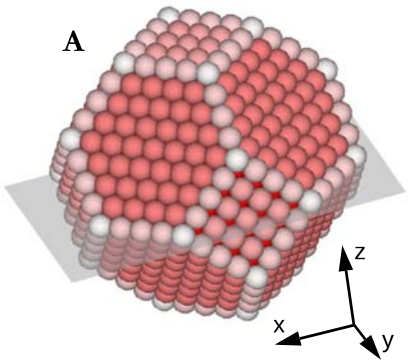

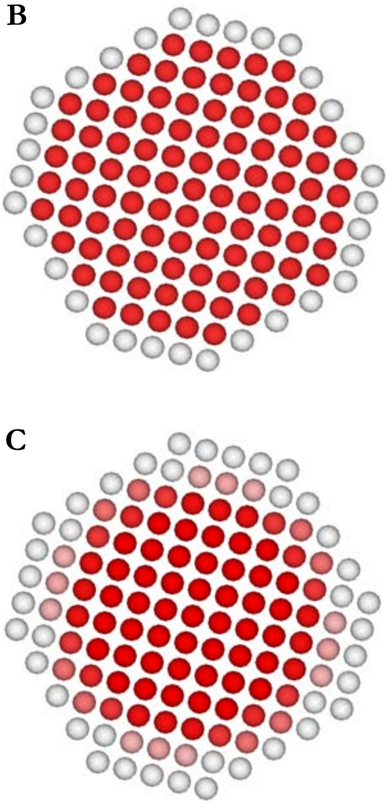

Figure 5.11: Spatially resolved exchange energy for both: short-range exchange and long-range exchange interactions. The spheres represent positions of magnetic moments in the simulation. They are color coded with respect to the exchange energy. Red spheres indicate high exchange coupling, whereas grey spheres represent weakly coupled moments.
(A) depicts the simulation geometry and a section plane. (B) shows short-range exchange interaction and (C) represents a section plane modeled with a long-range exchange formulation.
It should be noted that the pictures (B) and (C) were contrast enhanced to visualize the relevant features.

To answer the question whether differences in the formulation of exchange energy yield any effect on the coercive field, a hysteresis loop has been simulated ($T = 0$ K). Fig. 5.12 shows the second quadrant of this hysteresis loop. Whereas a short-range exchange formulation exhibits a dynamic coercive field of $H_c = 1.55$ T, the long-range exchange model shows $H_c = 1.3$ T. The long-range exchange formulation leads to a non-uniform exchange energy density near the surface of the particle. Once a surface atom becomes reversed, the reversed nucleus can more easily expand into the core of the particle which lowers the coercive field.

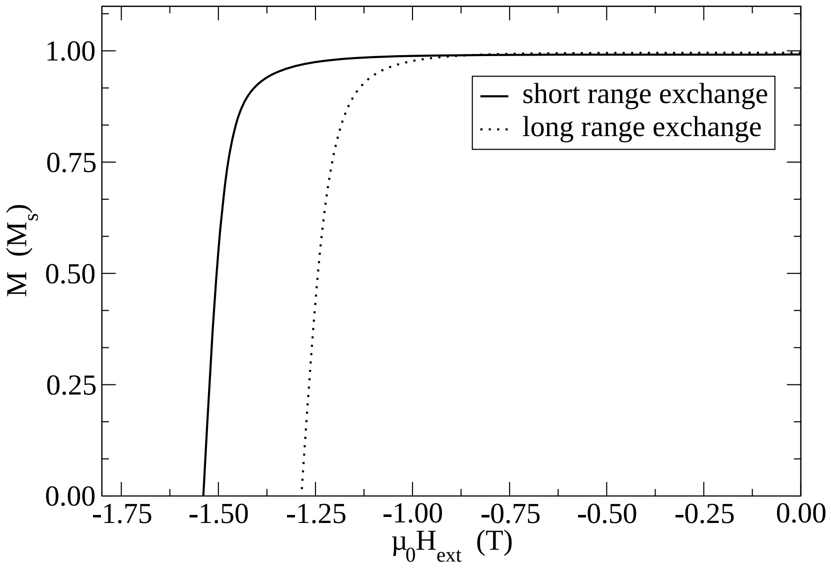

Figure 5.12: Second quadrant of a hysteresis loop simulation. The external field has been changed with a fast rate of 2.5 T/ns, yielding a higher coercive field than expected from experiments. The dashed line refers to a long-range exchange model, as introduced in section 5.2.1.

5.6 Thermal Effects

It has been demonstrated that long-range exchange and surface anisotropy described by the Neél model implicitly couples the motion of the atoms with the magnetic model. Therefore, this implicit coupling should also affect the saturation magnetization M_s in dependence on the temperature.
Fig. 5.13 depicts two different simulations exploring M_s as a function of the temperature. Again, the magnetic moments are set to the z-direction initially and M_s is determined at 17 different temperatures between $T = 0$ K and $T = 150$ K. To distinguish between thermal effects based on the thermal field H_{th} and effects introduced from the vibration of the individual atom, the magnetization has been additionally calculated with the motion of the atoms being suppressed. Moreover, Fig. 5.13 shows a fit to Bloch's $T^{3/2}$-law:

$$\frac{M_s(0) - M_s(T)}{M_s(0)} \propto (k_{\mathrm{B}}T)^{3/2} \tag{5.38}$$

Bloch's law is well reproduced by both simulations. Due to the additional fluctuations introduced by the motion of the atoms, a stronger decrease in the saturation magnetization occurs. The additional fluctuations are directly linked with the mean atomic displacement. The atomic displacements are in turn linked with the temperature of the system. Thus, the decrease of the saturation magnetization with respect to the simulations performed with fixed atomic positions can be attributed to crystalline vibrations. At $T = 150$ K the implicit introduction of fluctuations yields a decrease of about 10% of M_s as compared to a simulation on fixed atomic positions

.

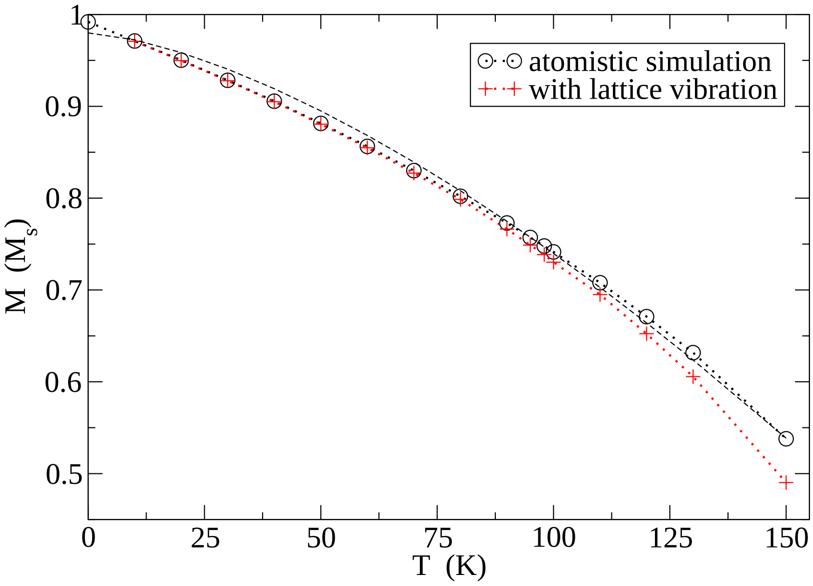

Figure 5.13: Saturation magnetization as a function of temperature. The dotted line corresponds to a fit to the Bloch law ($T^{3/2}$). Whereas black symbols represent the saturation magnetization gathered from a simulation with fixed positions of the individual magnetic moments, the red symbols are results from a simulation including the lattice vibration.

5.7 Summary and Outlook

Combining molecular dynamics simulation with magnetic modeling techniques allows for direct investigations of magnetic features influenced and determined by lattice vibrations. By including the motion of the atoms the crystalline configuration changes. Consequently, the effective anisotropy is affected. Moreover, due to the specific morphology of magnetic nanoclusters, exchange interactions should be modeled by an adequate long-range formulation. It has been shown that the motion of the atoms can change magnetic nanoparticles.

Phonons and magnons are thermodynamic systems which are influencing each other. For example, a crystal can be heated up by simply applying appropriate magnetic oscillating fields. On the other hand, heating a system thermally influences the magnetic state. Thus, energy can be exchanged between the phonon system and the magnon system allowing for an equilibrium situation between both systems. The approach used in this work does not strictly follow this thermodynamical point of view, the coupling between the motion of the atoms and the individual magnetic moments is introduced implicitly. Moreover, in its current formulation it is only a one-way coupling, i.e. magnons are not influencing phonons. Therefore, a future challenge might be the formulation of a coupled system allowing to interchange energy in both directions.

APPENDIX

6.1 Scaling Properties and Reducing Units

The considered physical quantities in molecular dynamics simulations are either extremely small (length scales) or very large (pressures), therefore it is a good idea to scale specific quantities to numerically reasonable numbers. This scaling process often reduces the units of the physical quantities to dimensionless numbers. Although scaling of quantities and reducing of units looks like a trivial task, it can be more complicated than it seems. Therefore, a detailed discussion about this issue is given in this chapter. Both, the equations necessary to calculate the motion of the atoms and the equations describing the evolution of the magnetic moments will be discussed. Moreover, often used physical constants are introduced.

6.1.1 Physical Constants

The following physical constants appear in conversion schemes and were taken from Ref. [95]:

$$k_{\mathrm{B}} = 1.380\,650\,3 \cdot 10^{-23}\frac{\mathrm{J}}{\mathrm{K}}$$

$$m_{\mathrm{u}} = 1.660\,540\,1 \cdot 10^{-27}\mathrm{kg}\,,$$

where k_{B} represents Boltzmann's constant and m_{u} is the atomic unit mass. Energies are often given in eV, which is the energy an electron gains or looses when moving through an electrical potential of 1V.

$$1\mathrm{eV} = 1.602\,176\,53 \cdot 10^{-19}\mathrm{J}\,.$$

Bohr's magneton is defined as

$$\mu_B = \frac{q_e \hbar}{2m_e} = 9.274\,006 \cdot 10^{-24} \mathrm{Am}^2 .$$

It represents the magnetic moment of an electron. q_e denotes the charge of the electron and m_e is its mass. $\hbar$ is Planck's constant divided by 2π.

$$q_e = 1.602\,176 \cdot 10^{-19} \mathrm{C}$$

$$\hbar = 1.054\,571\,68 \cdot 10^{-34} \mathrm{Js}$$

$$m_e = 9.109\,382\,6 \cdot 10^{-31} \mathrm{kg}$$

In SI units, magnetic fields are given in A/m. However, it is more convenient to specify fields after multiplying μ_0, leading to the unit $\mathrm{T} = \mathrm{kg}/(\mathrm{s}^2\mathrm{A})$.

$$\mu_0 = 4\pi \cdot 10^{-7} \frac{\mathrm{kgm}}{\mathrm{A}^2\mathrm{s}^2} .$$

Another constant often used in magnetic calculations is the Landé g-factor of an electron and the gyromagnetic ratio γ:

$$g_L = -2.0023$$

$$\gamma = \frac{\mu_B g_L \mu_0}{\hbar} = 2.212\,740 \cdot 10^5 \frac{\mathrm{m}}{\mathrm{As}} .$$

6.1.2 Scaling Equations for Molecular Dynamics Calculations

Typical time steps in molecular dynamics simulations are in the 10^{-15} s regime, thus the physical time is scaled via

$$t^* = k_t t = \sqrt{\frac{1\mathrm{eV}}{m_u A_{\mathrm{rel}}}} \cdot \frac{1}{10^{-10}\mathrm{m}} t . \tag{6.1}$$

Here, A_{rel} denotes the relative atomic mass. Since the scaling law contains $m_u A_{\mathrm{rel}}$, different masses result in different scaling factors. When dealing with alloys, k_t should be chosen to get the smallest time step Δt. Since k_t has the physical SI unit s^{-1}, t^* is dimensionless.

The masses used in MD simulations are also reduced and rescaled by

$$m^* = k_m m = m \frac{1}{m_u A_{\mathrm{rel}}} . \tag{6.2}$$

Again, k_m has the unit kg^{-1} yielding a dimensionless mass m^*. Finally, physical distances are transformed by the following relation:

$$\boldsymbol{x}^* = k_x \boldsymbol{x} = \frac{1}{10^{-10}\mathrm{m}} \boldsymbol{x} . \tag{6.3}$$

In order to get conversion rules for derived units, such as forces, energies and pressures, the Kirschner-method [96] is introduced: First, the equation expressing the quantity of interest is written in the desired unit. Each quantity is followed by a subscript in square brackets that gives the actual units. For example, the conversion factor for the force is obtained as follows:

$$\begin{aligned} F_{[\mathrm{N}]} &= m_{[\mathrm{kg}]}\frac{\mathrm{d}^2}{\mathrm{d}t_{[\mathrm{s}]}}\boldsymbol{x}(t_{[\mathrm{s}]}) = \frac{1}{k_{m[\mathrm{kg}^{-1}]}}\frac{1}{k_{\boldsymbol{x}[\mathrm{m}^{-1}]}}m^*_{[1]}\frac{\mathrm{d}^2}{\mathrm{d}t^2_{[\mathrm{s}]}}\boldsymbol{x}^*(t^*_{[1]}(t_{[\mathrm{s}]})) = \\ &\frac{1}{k_{m[\mathrm{kg}^{-1}]}}\frac{1}{k_{\boldsymbol{x}[\mathrm{m}^{-1}]}}m^*_{[1]}\left(\frac{\mathrm{d}t^*}{\mathrm{d}t}\right)^2\frac{\mathrm{d}^2}{\mathrm{d}t^{*2}_{[1]}}\boldsymbol{x}^*(t^*_{[1]}) = \frac{k_t^2}{k_m k_{\boldsymbol{x}}}m^*\frac{\mathrm{d}^2}{\mathrm{d}t^{*2}}\boldsymbol{x}^*(t^*) = \frac{1}{k_{F[\mathrm{N}^{-1}]}}m^*\boldsymbol{a}^* \end{aligned} \quad . \tag{6.4}$$

Applying this method on the kinetic energy yields:

$$\begin{aligned} E_{kin[\mathrm{J}]} &= \frac{1}{2}m_{[\mathrm{kg}]}\left(\frac{\mathrm{d}}{\mathrm{d}t_{[\mathrm{s}]}}\boldsymbol{x}(t_{[\mathrm{s}]})\right)^2 = \\ &\frac{k^2_{t[\mathrm{s}^{-2}]}}{2k^2_{\boldsymbol{x}[\mathrm{m}^{-2}]}k_{m[\mathrm{kg}^{-1}]}}\left(\frac{\mathrm{d}}{\mathrm{d}t^*_{[1]}}\boldsymbol{x}^*(t^*_{[1]})\right)^2 = \frac{1}{k_{E[\mathrm{J}^{-1}]}}\frac{1}{2}m^*\boldsymbol{v}^{*2} \end{aligned} \quad . \tag{6.5}$$

Since the temperature in molecular dynamics is derived from the mean-square velocities, this relation is used to determine the prefactor to get the temperature in Kelvin from the numeric calculations. The derivation is performed only for one particle which is, considered physically, pointless. Without loss of generality, the following equation is valid to obtain the right prescaling factor for the numerical temperature:

$$\begin{aligned} \frac{m\langle \boldsymbol{v}^2\rangle}{2}_{[\mathrm{J}]} &= \frac{3}{2}k_{B[\mathrm{J/K}]}T_{[\mathrm{K}]} \\ T_{[\mathrm{K}]} &= \frac{2}{3}\left(\frac{1}{k_B}\frac{k_t^2}{k_{\boldsymbol{x}}^2 k_m}\right)_{[\mathrm{K}]}\frac{1}{2}m^*\boldsymbol{v}^* = \frac{1}{3}\frac{1}{k_{T[\mathrm{K}^{-1}]}}m^*\boldsymbol{v}^* \end{aligned} \tag{6.6}$$

It should be pointed out that $1/k_T = (1\mathrm{eV})/k_\mathrm{B}$. This relation is often found to be the starting point in scaling laws. Here it was derived naturally by first scaling the basic units and then getting expressions for derived quantities.

Another important value in molecular dynamics is the pressure p:

$$p_{[\mathrm{Pa}]} = \frac{F_{[\mathrm{N}]}}{A_{[\mathrm{m}^2]}} = \frac{(1/k_F)F^*}{(1/k_{\boldsymbol{x}})^2A^*} = \frac{k_{\boldsymbol{x}}^2}{k_F}p^* = \frac{k_t^2k_{\boldsymbol{x}}}{k_m}p^* \tag{6.7}$$

Due to the fact that calculating forces in molecular dynamic simulation is always linked with building the gradient of potentials, the units of the potentials have to be investigated further. Conventional embedded atom potentials are likely to be given in eV instead of J. Typically Å (10^{-10} m) is used as length unit. As long as one uses the three scaling laws (Eq. 6.1, Eq. 6.2 and Eq. 6.3), the numerical values stemming from tabulated potentials (eV, Å) are correct. Changing one of the introduced scaling schemes yields an additional scaling factor before solving Newton's equations.

6.1.3 Scaling of the Landau-Lifshitz-Gilbert Equation

The Landau-Lifshitz-Gilbert equation can be written as

$$\frac{d\boldsymbol{m}_{\mathrm{at}}}{dt} = -\frac{|\gamma|}{1+\alpha^2}\boldsymbol{m}_{\mathrm{at}} \times \boldsymbol{H}_{\mathrm{eff}} - \frac{\alpha|\gamma|}{1+\alpha^2}\frac{1}{\boldsymbol{m}_{\mathrm{at}}}\boldsymbol{m}_{\mathrm{at}} \times (\boldsymbol{m}_{\mathrm{at}} \times \boldsymbol{H}_{\mathrm{eff}}).$$

$\boldsymbol{m}_{\mathrm{at}}$ denotes the magnetization in Am^2, $\boldsymbol{H}_{\mathrm{eff}}$ is the effective field in $\mathrm{A/m}$, γ is the gyromagnetic ratio in $\mathrm{m/As}$. α represents the phenomenological damping term.

In this work, each atom is equipped with a magnetic moment

$$\boldsymbol{m}_{\mathrm{at}} = g_{\mathrm{L}}\mu_{\mathrm{B}}S\boldsymbol{u}.$$

Here, $\boldsymbol{u}$ is a unit-vector pointing along the direction of the local magnetization. The constant S is adjusted to get comparable values for the saturation magnetization M_s (in $\mathrm{A/m}$):

$$M_s = \frac{m_{\mathrm{at}}}{V_{\mathrm{at}}},$$

where V_{at} is the volume per atom. In the case of face centered cubic crystals, V_{at} can be calculated via the lattice constant a:

$$V_{\mathrm{at}} = \frac{a^3}{4},$$

since each primitive cell comprises 4 atoms.

The Landau-Lifshitz-Gilbert equation can now be reformulated by taking into account magnetic fields given in T and magnetizations represented by unit-vectors:

$$\frac{d\boldsymbol{u}}{dt} = [-\boldsymbol{u} \times \boldsymbol{B}_{\mathrm{eff}} - \alpha\boldsymbol{u} \times (\boldsymbol{u} \times \boldsymbol{B}_{\mathrm{eff}})]\left(\frac{|\gamma|}{1+\alpha^2}\frac{1}{\mu_0}\right).$$

with

$$\boldsymbol{B}_{\mathrm{eff}} = \mu_0\boldsymbol{H}_{\mathrm{eff}}.$$

6.2 Potential Parameters

In this work, several different published potential functions were used. Although every author claims to have published a well-tested set of parameters, a verification of the asserted quality is highly recommended. In the ideal case, the verification procedure should be conducted with two different MD-codes to make sure that the potential delivers right results. This method is also very useful when developing a new molecular dynamics code.

If an alternative computer program is not available, there are still possibilities to locate bugs and to generate intermediate results with a new code. Apart from obvious problems like exploding clusters of atoms (wrong sign at the force calculation), some effective tricks have been developed to decide whether a problem has its origin in a faulty code or if it can be attributed to the potential itself.

It might sound ridiculous, but the first test being performed should be a plot of the potentials. A smooth curve is expected for all three functions (electronic density, pair potential and embedding function). In this context, the work of Zhou et al. [97] should be mentioned, where the given potentials for Pt and Ag (and probably other elements) exhibit points of discontinuities. Thus it is not recommended to use those potentials.

Plotting the pair potential $\phi(r)$ and the density function $\rho(r)$ delivers another important feature: The value of the cut-off radius can be chosen easily. In most cases, it is the electronic density which requires a reasonable cut-off radius. Both functions should exhibit small values (zero) at the cut-off distance. Some authors specify the mean electronic density $\bar{\rho}$ an atom experiences when in an equilibrated structure. Setting up a low-temperature simulation and monitoring the mean electron density should deliver exactly the specified number. Since the electronic density per atom is directly dependent on the cut-off radius, this method can be used to check if the cut-off radius has been chosen adequately. Obviously, too small values of $\bar{\rho}$ indicate a too small value of r_{cut}. Since lower electronic densities deliver a wrong embedding energy for that structure, one consequence of wrong electronic densities is to find wrong sublimation energies. If the cut-off radius has been chosen correctly and still the mean electronic density per atom does not match the quoted value, monitoring the number of neighbors per atom can help: Choosing consciously a wrong value for the cut-off radius between the first and the second nearest neighbor in a structure should deliver 12 nearest neighbors per atom for fcc-structures and 8 nearest neighbors for bcc structures. If these numbers are not found, the problem might be in the geometry part of the code.

Knowing the number of neighbors and their respective distances can also be helpful to verify a potential. By simply using graphs of $\rho(r)$, $F(\rho)$ and $\phi(r)$, the sublimation energy can be calculated manually via looking up the respective energy values.

Some of the potentials used are given hereinafter as a set of parameters and as plottings.

6.2.1 The Original Approach

Daw and Baskes, the inventors of the embedding atom method, published potentials for Nickel and Palladium [30]. Still, authors publishing potentials today are using their method to specify the different function by using knots of either natural or clamped splines [98,99]. For instance, Foiles and coworkers published potentials for Cu, Ag, Au, Ni, Pd and Pt [102], Meyer et al. published potentials for Fe and Ni [104]. The electronic density function is calculated using ab-inito data from Clementi et al. [101]. Although better first-principle calculations are available today, the accuracy of this data is still sufficient, since the fitting process necessary to obtain the embedding energy function and the pair potential function is much more imprecise than an ab-initio calculation can ever be.

Representative data to construct the pair potential, the electron density function and the embedding function are given in Table 6.1-6.3. Additionally, plottings of the functions from different authors are depicted in Fig. 6.1-6.3. The theory to construct the necessary functions is given in section 3.1.1.

Table 6.1: Effective charge function for Nickel. The function is given as a set of spline knots. Here, a clamped spline function is used (i.e. the first derivative of the function is specified). The first values (second row) refer to Daw and Baskes [30], the second set (fifth row) refer to Ref. [103].

r [Å]	$Z_{\mathrm{Ni}}(r)$ [a.u.] Daw and Baskes [30]	$Z'_{\mathrm{Ni}}(r)$	r [Å]	$Z_{\mathrm{Ni}}(r)$ [a.u.] K. Kadau [103]	$Z'_{\mathrm{Ni}}(r)$
0.0	28.0	0.0	0.0	28.0	0.0
1.5136	5.054		2.112	0.9874	
2.2880	0.294		2.4992	0.1596	
2.4992	0.137		2.992	0.0	0.0
2.9920	0.0	0.0			

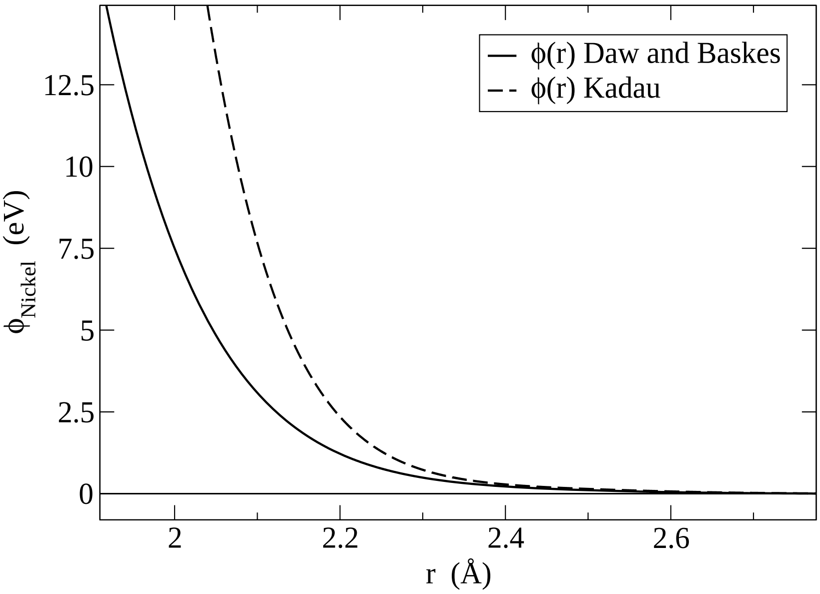

Figure 6.1: Comparison between different pair potential functions published by Daw and Baskes and Kai Kadau, respectively. It should be noted that both functions rapidly approach zero (between first [2.49Å] and second nearest neighbors [3.52Å]).

Table 6.2: Embedding function $F_{\mathrm{Ni}}(\rho)$. Again, the function is given as a set of spline knots. Contrary to the effective charge function, the spline given below is a natural spline with vanishing second derivatives at the first and the last knot. Values larger than $\rho = 0.065665$ Å^{-3} result in a linear extrapolation of the last gradient at this value.

ρ [Å^{-3}]	$F_{\mathrm{Ni}}(\rho)$ [eV] Daw and Baskes [30]	ρ [Å^{-3}]	$F_{\mathrm{Ni}}(\rho)$ [eV] K. Kadau [103]	$F''_{\mathrm{Ni}}(\rho)$
0.0	0.0	0.0	0.0	0.0
0.014275	-3.586	0.014126643	-3.6666553	
0.028550	-5.148	0.028253286	-5.38909894	
0.057100	-3.407	0.056506572	-3.61087316	
0.065665	0.0	0.064982557	0.0	0.0

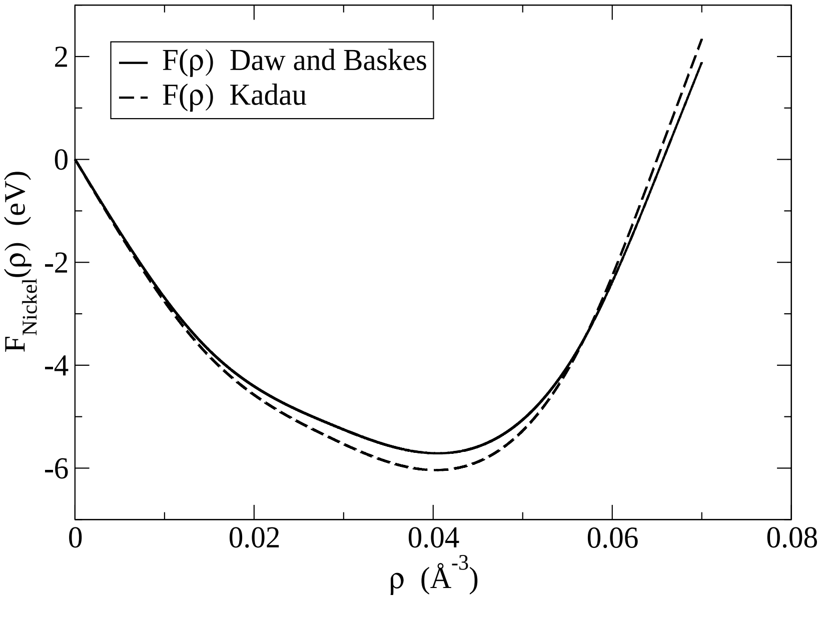

Figure 6.2: Embedding function $F(\rho)$ for Nickel. Since the pair potential for this category of potentials is entirely repulsive, the embedding function exhibits a pronounced attractive part. The mean electronic density,

$$\rho_i^h = \sum_{\text{neighbors}} \rho(r_{ij})$$

for an equilibrated system is given in [103] to be $\overline{\rho_{KK}} = 0.028253$. Daw and Baskes [30] were using $\overline{\rho_{DB}} = 0.02855$.

Table 6.3: Parameters to calculate the electronic density of Nickel (taken from [30] and [18]).

i	n_i	ξ_i [Å^{-1}] Daw and Baskes [30]	ξ_i [Å^{-1}] Kai Kadau [103]	C_i
4s				
1	1	54.88885	54.87049	-0.00389
2	1	38.48431	38.47144	-0.02991
3	2	27.42703	27.41786	-0.03189
4	2	20.88204	20.87506	0.15289
5	3	10.95707	10.95341	-0.20048
6	3	7.319580	7.31714	-0.05423
7	4	3.926500	3.92519	0.49292
8	4	2.152890	2.15217	0.61875
3d				
1	3	12.67582	12.67158	0.4212
2	3	5.43253	5.43072	0.70658

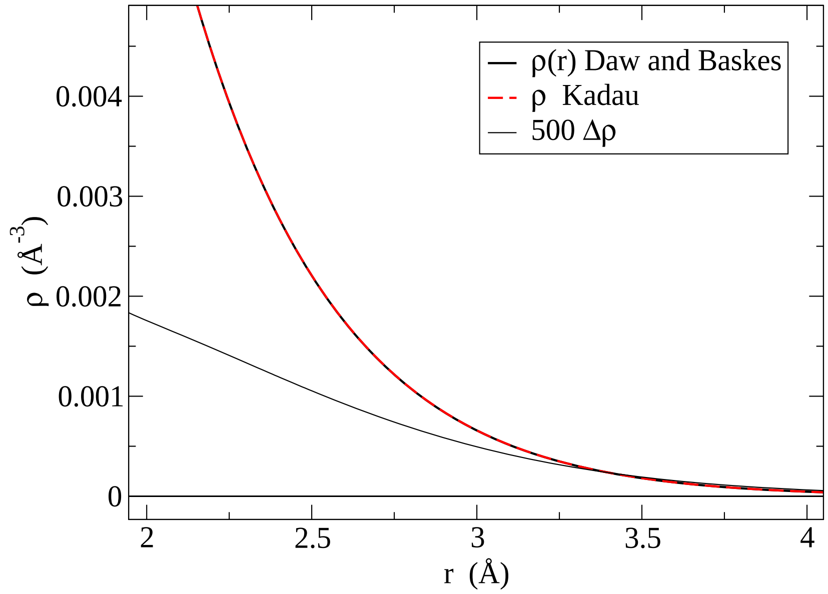

Figure 6.3: Electronic density function $F(\rho)$. Although in Ref. [103] better ab-initio values have been used, the difference between both functions is minimal. As described in the text, testing this function whether it can produce $\bar{\rho}$ is simple. A face centered cubic crystal has 12 nearest neighbors at $a_0/(\sqrt{2})$ (about 2.5Å for Ni) and 6 second nearest neighbors at a_0 (3.52Å for Ni). Looking up ρ at these distances and multiplying ρ with the according number of neighbors yields: $12 \cdot 0.002 + 6 \cdot 0.0003 = 0.0258$, which is close to the expected $\bar{\rho}$.

6.2.2 Zhou Potential

Zhou and co-workers developed a comprehensive set of potential function parameters (cp. Sect. 3.1.2). Since the presented potentials are normalized, they are suited for the simulation of alloys. Some selected parameter sets are given below.

Table 6.4: Potential parameters of selected elements. Parameters of the same form for Cu, Pd, Al, Pb, Mo, Ta, W, Mg, Ti and Zr can be found in Ref. [41].

	Ag	Au	Co	Fe	Ni	Pt
r_e	2.891814	2.885034	2.505979	2.481987	2.488746	2.771916
f_e	1.106232	1.529021	1.975299	1.885957	2.007018	2.336509
ρ_e	15.539255	21.319637	27.206789	20.041463	27.984706	34.108882
α	7.944536	8.086176	8.679625	9.818270	8.029633	7.079952
β	4.237086	4.312627	4.629134	5.236411	4.282471	3.775974
A	0.266074	0.230728	0.421378	0.392811	0.439664	0.449644
B	0.386272	0.336695	0.640107	0.646243	0.632771	0.593713
κ	0.425351	0.420755	0.500000	0.170306	0.413436	0.413484
F_{n0}	0.850703	0.841511	1.000000	0.340613	0.826873	0.826967
F_{n1}	-1.729619	-2.930281	-2.541799	-2.534992	-2.693996	-4.099542
F_{n2}	-0.221025	-0.554034	-0.219415	-0.059605	-0.066073	-0.754764
F_{n3}	0.541558	1.489437	0.733381	0.193065	0.170482	1.766503
λ	-0.967036	-0.886809	-1.589003	-2.282322	-2.457442	-1.578274
F_0	-1.750000	-2.980000	-2.560000	-2.540000	-2.700000	-4.170000
F_1	0.000000	0.000000	0.000000	0.000000	0.000000	0.000000
F_2	0.983967	2.283863	0.705845	0.200269	0.282257	3.474733
F_3	0.520904	0.494127	-0.687140	-0.148770	0.102879	2.288323
η	1.149461	1.286960	0.694608	0.391750	0.509860	1.393490
F_e	-1.751274	-2.981365	-2.559307	-2.539945	-2.700493	-4.174332

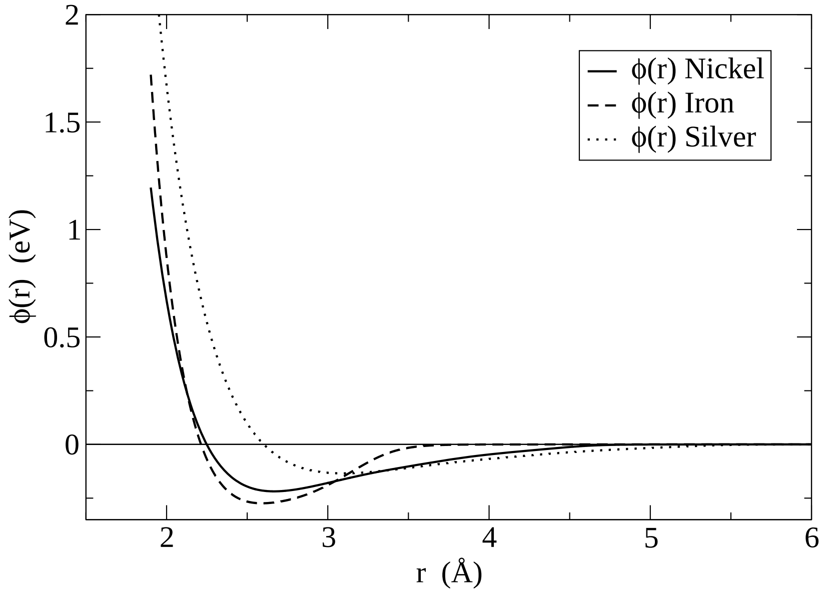

Figure 6.4: Pair potential function $\phi(r)$ for Ni, Fe and Ag. In contrast to the potentials discussed in the last chapter, $\phi(r)$ exhibits also attractive parts, which is due to the fact that these potentials are normalized (cp. Eq. 3.15). Due to their special parameterized construction, the potential functions automatically approach zero within the cut-off radius.

Fig. 6.4 and Fig. 6.5 show examples of the pair potential functions for Ni, Fe and Ag and their respective embedding energy function $F(\rho)$.

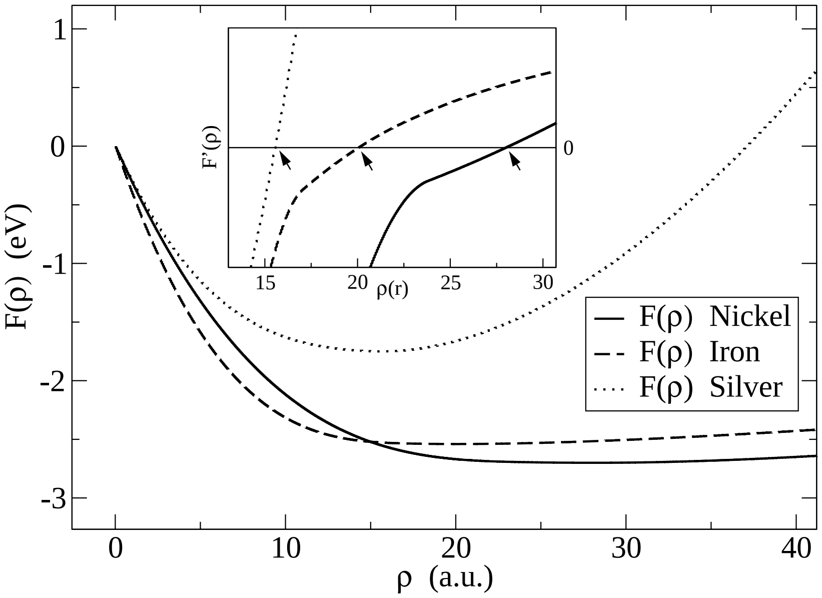

Figure 6.5: Embedding functions for Ni, Fe and Ag. The inset shows the first derivative of the according embedding functions. Due to the normalization rule, the first derivative vanishes at $\rho_{Ni} = 27.985$, $\rho_{Fe} = 20.041$ and $\rho_{Ag} = 15.539$ (cp. Table 6.4).

Fig. 6.6 depicts different electron density functions and ρ_{host} as it is experienced by Ag in a distance of 1 Å in a fcc bulk structure.

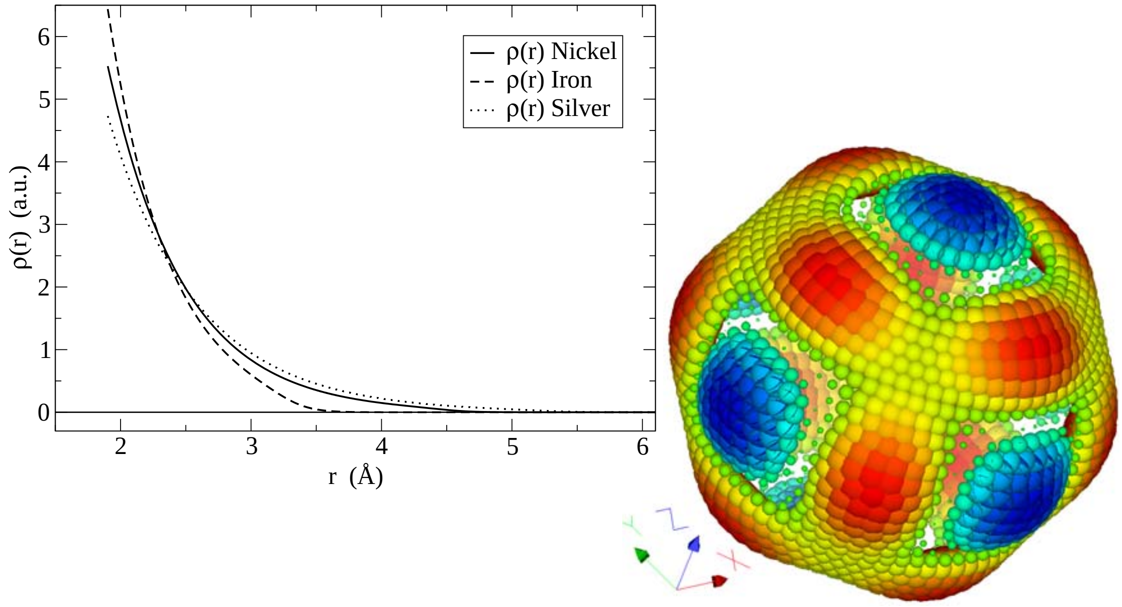

Figure 6.6: Left: Electron density function for Ni, Fe and Ag, respectively. Since they are constructed in a similar way as the pair potential function, $\rho(r)$ approaches zero within the cut-off radius.
Right: Distribution of the superimposed electron density around a Ag atom in a fcc bulk structure. The electron density function has been evaluated in a radial distance of 1 Å from the (not depicted) Ag center atom. Red areas represent a high electron density, whereas blue areas depict regions with a low density. It should be noted that, although the underlying atomic electron density functions are radial symmetric, the superposition of these atomic functions reflects the underlying face centered cubic structure.

6.3 A Short Guide to FMD

It is beyond the scope of this thesis to discuss and present all the written software tools used. Anyhow, this chapter should provide enough information to start a molecular dynamics simulation using `FMD`, which was used to calculate all the presented results. `FMD` and further necessary tools are described in a general way rather than discussing the specific source code.
A typical workflow for a molecular dynamics simulations comprises

- Parameter and geometry setup
- Simulation of the desired system
- Analysis of the results

6.3.1 The Parameter File

All parameters for a molecular dynamics simulation can be adjusted by providing an initialization file as a parameter to `FMD`. Values in this file are specified in the following way:

```
l_x = 7.046
```

Comments are allowed and are defined by a preceding “#”.

The initialization file consists of three blocks of data: general parameters for the simulation (e.g. time step Δt), configurational data for each atom (e.g. mass, type) and a description of the external quantities being changed during a simulation run. The latter is specified by using the character “>”. A typical configuration to simulate a (very fast) hysteresis loop is given as example:

```
#> t[ps] Hx Hy Hz [T] T [K] newlog nroffld nroflogentr
>    0   0  0   -2.8  293    1      10       1000
>   10   0  0   -2.8  293
>   20   0  0   -2.8  293    1      10       1000
>   40   0  0   0     293
>   60   0  0   2.8   293    1      10       1000
>   80   0  0   2.8   293
>  100   0  0   2.8   293
```

The first column represents a point in time, the next three columns are used to describe the external field $\boldsymbol{H}(t)$ acting on the system and the last column provides information about the desired temperature T as a function of time. The next three columns are optional and allow detailed adjustments of the amount of data being produced by `FMD`. `newlog` is a flag indicating that a new LOG file should be created. Every `nroffld` lines in the LOG file, the complete configuration (including a frame in a XYZ[1]-file and a FLD/DAT[2] combination in case of magnetic simulations) will be written. `nroflogentr` specifies the number of lines of the actual LOG file. In the example above, three different LOG files are produced, each containing 1000 entries. During the processing of each section, 100 snapshots (spins, positions) will be produced. Fig. 6.7 is a graphical representation of the example given above. Values between declared points in time are interpolated linearly. The according C-Code providing the necessary interface to get the information given in the parameter file, is explained in detail in Ref. [63].

---

[1] XYZ-files can be displayed using either VMD [60] or MDL® Chime [61].

[2] FLD/DAT combinations represent vector informations (i.e. the spin-system) and can be visualized with MicroAVS® [62].

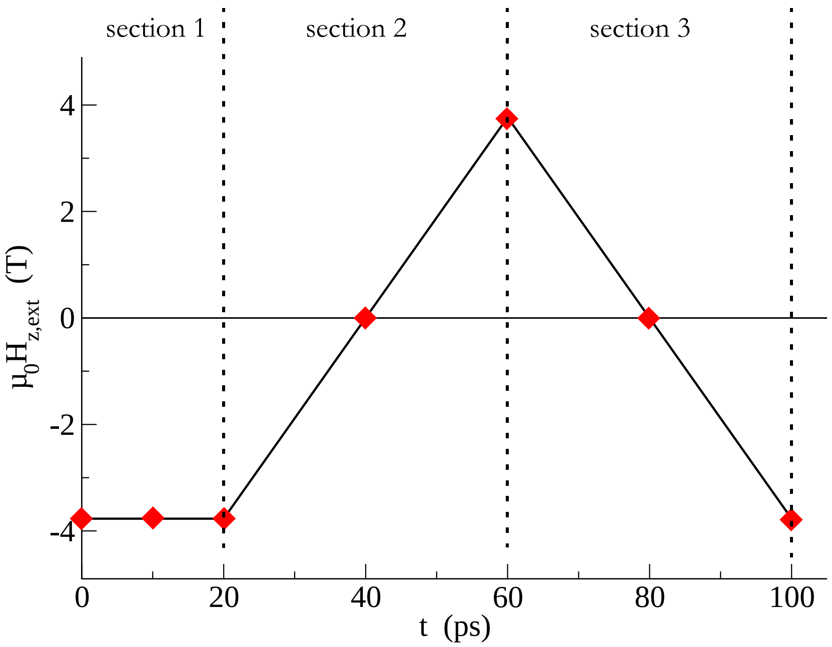

Figure 6.7: Visualization of the control mechanism of physical quantities. In this example, three sections are defined. Each red diamond represents a line in the descriptive section of the parameter file. Within each section, the number of complete snapshots can be controlled by the values of `nroffld`. The values between two diamonds are interpolated by `FMD`.

It is possible to enable or disable the logging of quantities in the parameter file by specifying the respective `LOG_` switches.

```
LOG_SCALEV = 1
LOG_TACT = 0
LOG_TAVR = 1
```

Here, the actual value of the velocity scaling mechanism and the average temperature will be logged, whereas the actual temperature is excluded. A line in the LOG file always starts with the actual time (column 1) followed by the specified quantities in the LOG file. The most important quantities are: `LOG_TACT` (actual temperature), `LOG_PACT` (actual pressure), `LOG_EPHI`, `LOG_EEMB`, `LOG_EKIN`, `LOG_EPOT`, `LOG_ETOT` (energies), `LOG_EEXT` (extended total energy of the Nosé-Hoover thermostat). `LOG_RHOMEAN` can be used to analyze the mean electron density per atom and `LOG_NR_NN` is used to get the mean number of neighbors being used for the given cut-off radius. A complete list of possible entries in the LOG file can be found in the file `md.h`.

The desired initial geometry and specific information for each atom (e.g. initial spin direction) can also be specified in the parameter file. Each atom starts with the character “p” and a subsequent number. As an example, a system with four Nickel atoms at a temperature of 10K is given below.

```
#nr   x   y   z    vx        vy        vz        FxFyFz SxSySz fx type
p1 = 4.4 6.1 6.1  2.3e-02  9.2e-04 -1.3e-02  0 0 0  0 0 1  0  28
p2 = 6.1 4.4 6.1  3.5e-02 -4.0e-02  1.5e-02  0 0 0  0 0 1  0  28
p3 = 6.1 6.1 4.4  2.9e-02  4.1e-02  3.5e-02  0 0 0  0 0 1  0  28
p4 = 4.4 4.4 4.4 -1.9e-02  2.5e-03 -2.0e-02  0 0 0  0 0 1  0  28
```

The first three columns specify the positions of the individual atoms in Å, the next three values are the according velocity in internal units, the forces are set to zero in this example. The initial spin direction is set to the z-direction. `fx` is a flag to fix an atom in space, i.e. it is excluded from the position update process and is especially useful to fix a cluster in space during the equilibrium process. It should be noted that fixing atoms in space severely harms thermodynamic laws. It can also be used to model a surface at T=0K. The last column denotes the material used, in the example above it is Nickel (atomic number 28). After processing the parameter file, `FMD` tries to find potential files for each specified material. In the example above, `Ni.pfi` will be opened, i.e. potential files always consist of the short chemical name of the material with the extension `.pfi`. If more than one material is specified, `FMD` automatically calculates the necessary alloy potentials internally. Potential files are simple text files holding the three potential functions and their respective derivatives. The `pfi` format used with `FMD` is very similar to the `POCO pfi` format described in Ref. [64].

In addition to the specific XYZ - and FLD/DAT- files, a complete system configuration is written as CFG file. The format used in this file type is identical with the format used in the parameter file to specify the system’s geometry. Therefore, a simulation can be resumed by copying the according snapshot to the parameter file.

The information about the atoms’ geometry are read into a linked cell scheme. The cell size can be specified with the parameters `l_x`, `l_y`, `l_z`. The number of cells used in the simulation is given by the values `nc_x`, `nc_y`, `nc_z`. Therefore, the volume of the simulation box equals

$$V_{box} = l_x l_y l_z nc_x nc_y nc_z . \tag{6.8}$$

The positions of the atoms have to lie within this volume. The given geometry can be changed by special scaling values, specified by `scale_geom_x`, `scale_geom_y` and `scale_geom_z` affecting the positions and the volume of each cell of the linked cell geometry. This feature is useful to perform a range of simulations at different system volumes.

Initial configurations can be created automatically by gen_config.

```
gen_config CTYPE=FCC LATA=3.85 STYPE=BULK TEMP=100 NX=3 NY=3 NZ=3
               CELL=7.7 ATOMS=Fe:53;Pt:47 NROFAT=864 OUTPUT=FePt.cfg
```

Here, a fcc bulk system with a lattice constant a =3.85 Å is specified. `STYPE` allows to change from a bulk structure to a cluster simulation. This is achieved by adding enough empty cells on the boundaries of the simulation geometry to oppress the minimum image convention code. In other words, the distances between atoms on the surface of the simulations are too big to fulfill the periodic boundary condition. `TEMP` can be used to specify the initial temperature of the simulation[1], `NX`, `NY`, `NZ` refer to the linked cell scheme. `CELL` denotes the size of a single cell. `ATOMS` specifies the different types of materials used. Here an $Fe_{53}Pt_{47}$ alloy is set up. The atoms are distributed randomly on the fcc lattice. `NROFAT` specifies the total number of atoms of the simulation and `OUTPUT` denotes the name of the CFG file to be written. This file can be copied directly to the parameter file. Additionally, a XYZ file is written to control the output of `gen_config` (config.xyz). Due to the fact that the parameters of `gen_config` allows ambiguous combinations (e.g. `NROFAT` depends on the specified size of the simulation box and on `STYPE`), the generated configuration should also be double-checked by opening config.xyz with an appropriate visualization program. Invoking `gen_config` without parameters displays a complete list of possible parameters.

6.3.2 Starting a Simulation

After reading the parameter file, the simulation process is invoked by starting `FMD` with the file containing all information as parameter. Fig. 6.8 shows a simplified flow diagram of the simulation code.

---

[1] not implemented yet

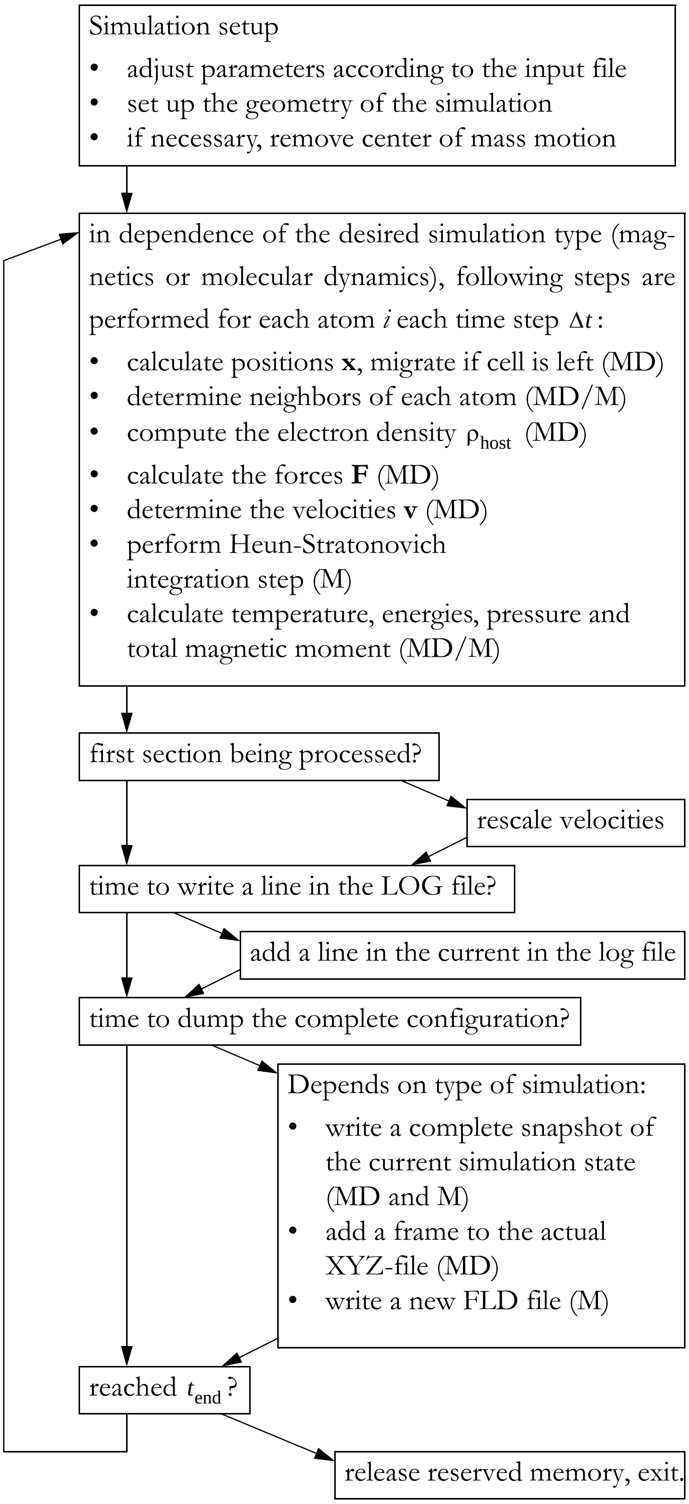
Simulation setup
adjust parameters according to the input file
set up the geometry of the simulation
if necessary, remove center of mass motion
in dependence of the desired simulation type (magnetics or molecular dynamics), following steps are performed for each atom i each time step Δt:
calculate positions x, migrate if cell is left (MD)
determine neighbors of each atom (MD/M)
compute the electron density ρhost (MD)
calculate the forces F (MD)
determine the velocities v (MD)
perform Heun-Stratonovich integration step (M)
calculate temperature, energies, pressure and total magnetic moment (MD/M)
first section being processed?
rescale velocities
time to write a line in the LOG file?
add a line in the current in the log file
time to dump the complete configuration?
Depends on type of simulation:
write a complete snapshot of the current simulation state (MD and M)
add a frame to the actual XYZ-file (MD)
write a new FLD file (M)
reached tend ?
release reserved memory, exit.

Figure 6.8: Flow diagram of the simulation core of `FMD`.

6.3.3 Analysis of Simulation Results

Standard analysis of molecular dynamics results comprises plotting desired LOG-entries as a function of time. XMGrace is a well-suited tool for this purpose [100]. More complex visualization tasks can be performed with MDL® Chime [61] or VMD [60]. However, although many tools are available to visualize simulation results, there is almost no software available to analyze geometry data. For example, no code could be found to detect crystal planes within an arbitrarily orientated structure. Therefore, an analysis library was written to perform specific post-processing tasks. Additionally, a graphical frontend was designed, combining some of the most frequently used tasks. Fig. 6.9 shows a screen-shot of GeoToolbox, which provides easy access to some of the features of the written analysis library. GeoToolbox can be used to determine the relative orientation of a cluster with respect to the z-axis. The detection of crystal planes and their relative position is also possible. That is to say, a determination of fractional crystal structures within an arbitrary configuration of atoms is possible. The methods used are described in a general way in section 4.4.3.

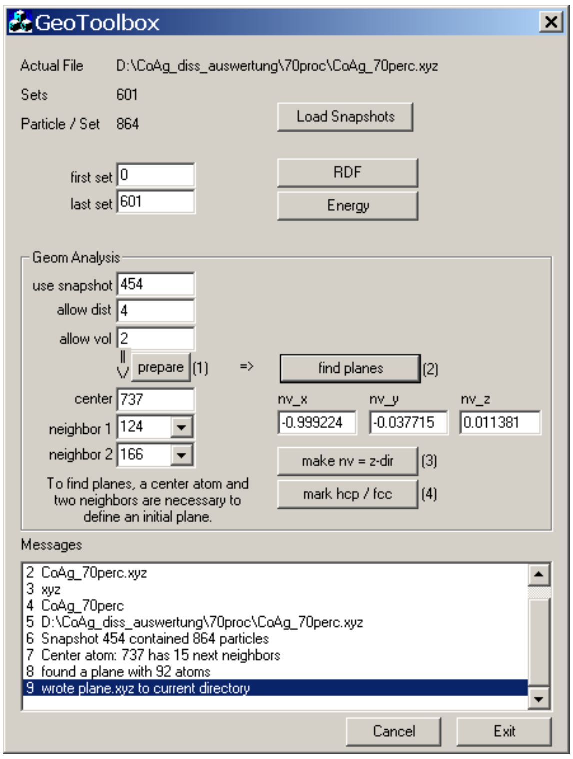

Actual File D:\CoAg_diss_auswertung\70proc\CoAg_70perc.xyz
Sets 601
Particle / Set 864
first set 0
last set 601
use snapshot 454
allow dist 4
allow vol 2
center 737
neighbor 1 124
neighbor 2 166
nv_x -0.999224
nv_y -0.037715
nv_z 0.011381

To find planes, a center atom and two neighbors are necessary to define an initial plane.

```
2 CoAg_70perc.xyz
3 xyz
4 CoAg_70perc
5 D:\CoAg_diss_auswertung\70proc\CoAg_70perc.xyz
6 Snapshot 454 contained 864 particles
7 Center atom: 737 has 15 next neighbors
8 found a plane with 92 atoms
9 wrote plane.xyz to current directory
```

Figure 6.9: Graphical User Interface for the post-processing library. GeoToolbox is capable of reading XYZ files. It displays the number of snapshots of the specified file. The radial distribution function and potential energies of the according snapshots can be calculated easily. Moreover, an automated plane-detection was implemented. Starting from the center atom and two other neighbors of the center atom, the tool tries to find a crystal structure within the given assembly of atoms. A Voronoi tesselation is performed to get the neighborhood of each atom.
If the structure could be determined by finding individual crystal planes, the normal vector of these planes can be used to transform this normal vector to point to the z-direction. Finally, in case of a structure with a faulty stacking order (fcc and hcp), GeoToolbox can identify individual planes as fcc planes or hcp planes, depending on their neighboring planes.

After loading the dedicated XYZ file holding snapshots of the atoms' position, an individual snapshot can be selected (in the example above, snapshot number 454 was selected). By using the "prepare"-function, the atom closest to the center of the aggregate atoms is determined. Two neighboring atoms of this center atom are necessary to detect the according plane the center atom belongs to. Two parameters have to be adjusted for this purpose: a maximum distance between detectable crystal planes and a maximum volume. To decide whether an atom is a member of a dedicated plane, the maximum volume declares the upper bound for the volume defined by four atoms (i.e. the three initial atoms and the atom to test). After the detection of the first plane, neighboring planes are searched parallel to the first plane. GeoToolbox tries to assign each individual atom to a crystal plane which lies parallel to the first found plane. That is to say, multiple twinned particles can not be analyzed in this way.

Finally, the normal vector (perpendicular to the initial plane) is used to rotate the configuration in a way that the detected crystal planes are parallel to the xy-plane of the coordinate system.

Additionally, GeoToolbox is capable of determining the stacking order of mixed fcc/hcp structures, presumed to have a (111) plane as initial plane. The neighboring planes of the investigated crystal planes are mapped onto each other (i.e. mirrored on the plane to be determined). If the neighboring planes match, an ABA ordering exists, if no matching can be achieved, an ABC ordering is detected. In terms of crystal structures, an ABA stacking ordering represents a hcp plane whereas an ABC ordering indicates a fcc plane.

LIST OF FIGURES

Figure 2.1: Temperature distribution for a velocity scaling scheme and the Nosé-Hoover method. Whereas the Nosé-Hoover scheme reproduces the canonical distribution well, the velocity scaling scheme does not reproduce the desired distribution. (simulated system: Ag, 100 atoms, total number of integration steps: 2×10^6, $Q=10^6$, desired temperature: 1500K) 21

Figure 2.2: Lennard-Jones potential for $\sigma = 1$ and $\varepsilon = 1$. Note that on the abscissa the potential approaches zero rapidly. This legitimates the usage of a cut-off radius. 23

Figure 2.3: Method to test, whether a used potential is conservative or not. The blue spheres represent a configuration of atoms at fixed postitions whereas the red sphere follows a closed loop. Integrating the calculated forces along the closed loop should yield zero work when reaching the initial position again. State 1, 5 and 9 clearly show that no work has been done on a closed loop, which indicates that the potential function is conservative. The graph below depicts three different closed loops through the configuration of the blue spheres generating the potential landscape. An embedded atom potential for Co was used for this calculation.. 27

Figure 2.4: Linked-cell geometry (two-dimensional). The left picture represents a 7x5 cell geometry. Each cell has to have at least a side length of r_{cut}. Thus, only neighboring cells have to be considered while finding relevant atoms. On the right, the minimum image convention is depicted, i.e. an atom in the corner cell interacts with cells from the opposite border. Each cell has 8 (2D) and 26 (3D) neighbor cells, respectively. 28

Figure 2.5: Comparison between an algorithm using the linked-cells method and the neighbor list algorithm. The linked-cells computation time per particle is independent on the total number of particles simulated. When performing calculations with only some hundreds of atoms involved, the neighbor list algorithm is faster due to additional overhead computation. The unit on the ordinate represents a measure between reality and simulation: Unity would represent a real-time capability of a simulation in a one-processor per particle approach. 29

Figure 3.1: Four different crystal structures for the elements Nickel (A), Iron (B), Cobalt (C) and the alloy Iron-Platinum (D). The arrows indicate the lattice constant a and c.
At room temperature, Ni appears in the face-centered cubic structure (space group: Fm3m, Pearson symbol: cF4, Strukturbericht designation: A1), Fe can be found in the body-centered cubic structure (Im3m, cI2, A2), Co appears in hexagonal closed-packed form (P6$_3$/mmc, hP2, A3) and one of the possibilities for FePt is a face-centered tetragonal structure (P4/mmm, tP2, L1$_0$). 38

Figure 3.2: Comparison of the functional shape of for three different potentials for Nickel (cp. section 6.2). Each symbol represents a NVT-MD simulation at a given volume and a constant temperature (10K). The inset shows the relevant scope of volumes where the pressure vanishes. Whereas the differences around V_0 between the three different potentials are comparably small, at smaller volumes (higher pressures) a significant discrepancy can be observed. 39

Figure 3.3: Lattice constant as a function of the temperature for Nickel. In general, the potential proposed by Zhou et al. reproduces the experimental findings best. Anyhow, compared to experimental data, all three simulations tend to overestimate the lattice constant. The experimental data have been taken from Ref. [46]. 41

Figure 3.4: Energy per atom in dependence of the volume of the system. The temperature in these simulations was T=10 K. Again, three different potentials were used. The dashed lines are fitting curves correspond to Eq. 3.34. 44

Figure 3.5: Sublimation energy of Ni for different potentials as a function of the temperature. E_s depends linearly on the temperature. 46

Figure 3.6: Phase diagram of FePt, taken from Ref. [50]. 47

Figure 3.7: Atomic configuration for Fe$_{50}$Pt$_{50}$ in the disordered fcc phase (A) and the ordered face-centered tetragonal phase (B). The yellow spheres represent Iron, whereas the blue spheres depict Platinum. 48

Figure 4.1: Development of the storage density for hard-disk and solid-state memory. Today, hard disks with 100 GBit/in^2 are produced. The ambition of an areal storage density of 1 TB/in^2 requires the use of novel materials and recording techniques (image taken from www.hgst.com). 51

Figure 4.2: Radial distribution function for the crystal structure hcp (Co) and fcc (Ni) at a temperature of T=10 K (N=4000). Additionally, $g(r)$ for Ni was plotted at an elevated temperature (T=293K). In the low-temperature case, the relative position of atoms is well defined, whereas the peaks are broadened at higher temperatures, indicating stronger fluctuations of the positions. The resulting functional shape of the radial distribution function is specific to the underlying crystal structure. Thus, $g(r)$ can be used to determine the crystal structure of a simulation. 54

Figure 4.3: Voronoi tesselation of randomly distributed points in two dimensions. Points sharing an edge are neighbors per definition. Therefore, position A and B are not neighbors because they do not share a common edge. 55

Figure 4.4: Snapshots taken during the simulation of the formation of a Co$_{65}$Ag$_{35}$ cluster, consisting of 864 atoms in total. (A) depicts the initial configuration with Co and Ag atoms randomly distributed on a fcc grid. (B,C) are snapshots at T=1100 K and 600 K, respectively. (D) displays the final configuration. 57

Figure 4.5: Atomic concentration of a CoAg cluster, measured from the center. A sharp transition between the Co core and the Ag shell occurs at 1.2 nm from the center. The inset on the right shows a $Co_{70}Ag_{30}$ cluster sliced along a (111)-plane. 58

Figure 4.6: Calculated radial distribution function of the core of a $Co_{75}Ag_{25}$ cluster at 100K. Compared to the RDF of fcc Co, two additional peaks at 4.1 Å and 4.8 Å arise (see arrows). This is a clear indication for partial hcp stacking in the core. 59

Figure 4.7: Left: Stacking order of the Co core (without the Ag shell) of a $Co_{70}Ag_{30}$ cluster. Right: The arrow indicates the line of sight with respect to the depiction on the left side. Whereas each plane A, B and C itself are perfect (111)-planes, the vertical stacking order does neither follow the fcc-stacking ABC nor does it follow a plain hcp-stacking AB. 60

Figure 4.8: Exploded view of a CoAg cluster. Silver spheres represent Ag, purple spheres are Co atoms. Additionally, the center plane of the structure is depicted (without Ag). The individual planes are (111) planes, which only exhibit occasional in-plane stacking faults. 61

Figure 5.1: Motion of the magnetic moment in an effective field, described by the Landau-Lifshitz-Gilbert equation. (taken from Ref. [80]). 66

Figure 5.2: Estimated functional shape of J_{ij} as a function of the distance r_{ij} for Co. The symbols mark relevant neighbor distances, the numbers at the symbols represent the number of neighbors at the given distance. 69

Figure 5.3: Energy landscape for a system exhibiting cubic anisotropy ($K_1 > 0$ and $K_2 > 0$). Easy directions are aligned along the [100], [010] and [001] direction. 70

Figure 5.4: 1289 Co atoms forming a truncated octahedron. The surface-to-volume ratio is 482:807. Whereas in bulk materials this ratio can often be neglected, here the properties of the system are mainly determined by surface effects. 74

Figure 5.5: Energy landscape of a perfectly truncated Co octahedron without annealing (static system). The system shows an overall uniaxial anisotropy with minor deviations coming from the facets of the particle. 76

Figure 5.6: Energy surface for a simulated annealed core of a CoAg system. 77

Figure 5.7: Equilibrium magnetic configuration in dependence of the value of the surface anisotropy constant at $T = 0$ K. (A) shows the configuration simulated with $K_s = -15$ MJ/m³. (B) was calculated with $K_s = 15$ MJ/m³. Negative values of K_s lead to surface moments preferring an out-of-plane direction whereas positive values yield an in-plane surface anisotropy.
(C) indicates the point of view (along the y axis) 78

Figure 5.8: Magnetization M_z as a function of the surface anisotropy constant K_s. The surface anisotropy introduces a inhomogenous magnetic configuration resulting in a decrease of M_z. Furthermore, the effect of implicit coupling between the vibrations of the surface atoms at elevated temperatures is depicted (dashed line). 79

Figure 5.9: Dependence of the dynamic coercive field on the surface anisotropy constant. Contributions arising from the surface anisotropy are primarily determining the dynamic coercive field. 80

Figure 5.10: Dynamic coercive field in dependence of fluctuating local anisotropy axes. The introduction of magnetic fluctuation introduces only minor changes of the coercive field. 81

Figure 5.11: Spatially resolved exchange energy for both: short-range exchange and long-range exchange interactions. The spheres represent positions of magnetic moments in the simulation. They are color coded with respect to the exchange energy. Red spheres indicate high exchange coupling, whereas grey spheres represent weakly coupled moments. (A) depicts the simulation geometry and a section plane. (B) shows short-range exchange interaction and (C) represents a section plane modeled with a long-range exchange formulation. It should be noted that the pictures (B) and (C) were contrast enhanced to visualize the relevant features. 82

Figure 5.12: Second quadrant of a hysteresis loop simulation. The external field has been changed with a fast rate of 2.5 T/ns, yielding a higher coercive field than expected from experiments. The dashed line refers to a long-range exchange model, as introduced in section 5.2.1. 83

Figure 5.13: Saturation magnetization as a function of temperature. The dotted line corresponds to a fit to the Bloch law ($T^{3/2}$). Whereas black symbols represent the saturation magnetization gathered from a simulation with fixed positions of the individual magnetic moments, the red symbols are results from a simulation including the lattice vibration. 84

Figure 6.1: Comparison between different pair potential functions published by Daw and Baskes and Kai Kadau, respectively. It should be noted that both functions rapidly approach zero (between first [2.49Å] and second nearest neighbors [3.52Å]). 91

Figure 6.2: Embedding function $F(\rho)$ for Nickel. Since the pair potential for this category of potentials is entirely repulsive, the embedding function exhibits a pronounced attractive part. The mean electronic density,

$$\rho_i^h = \sum_{\text{neighbors}} \rho(r_{ij})$$

for an equilibrated system is given in [103] to be $\overline{\rho_{KK}} = 0.028253$.
Daw and Baskes [30] were using $\overline{\rho_{DB}} = 0.02855$. 92

Figure 6.3: Electronic density function $F(\rho)$. Although in Ref. [103] better ab-initio values have been used, the difference between both functions is minimal. As described in the text, testing this function whether it can produce $\bar{\rho}$ is simple. A face centered cubic crystal has 12 nearest neighbors at $a_0/(\sqrt{2})$ (about 2.5Å for Ni) and 6 second nearest neighbors at a_0 (3.52Å for Ni). Looking up ρ at these distances and multiplying ρ with the according number of neighbors yields: $12 \cdot 0.002 + 6 \cdot 0.0003 = 0.0258$, which is close to the expected $\bar{\rho}$. 93

Figure 6.4: Pair potential function $\phi(r)$ for Ni, Fe and Ag. In contrast to the potentials discussed in the last chapter, $\phi(r)$ exhibits also attractive parts, which is due to the fact that these potentials are normalized (cp. Eq. 3.15). Due to their special parameterized construction, the potential functions automatically approach zero within the cut-off radius. 95

Figure 6.5: Embedding functions for Ni, Fe and Ag. The inset shows the first derivative of the according embedding functions. Due to the normalization rule, the first derivative vanishes at $\rho_{\mathrm{Ni}} = 27.985$, $\rho_{\mathrm{Fe}} = 20.041$ and $\rho_{\mathrm{Ag}} = 15.539$ (cp. Table 6.4). 95

Figure 6.6: Left: Electron density function for Ni, Fe and Ag, respectively. Since they are constructed in a similar way as the pair potential function, $\rho(r)$ approaches zero within the cut-off radius.
Right: Distribution of the superimposed electron density around a Ag atom in a fcc bulk structure. The electron density function has been evaluated in a radial distance of 1 Å from the (not depicted) Ag center atom. Red areas represent a high electron density, whereas blue areas depict regions with a low density. It should be noted that, although the underlying atomic electron density functions are radial symmetric, the superposition of these atomic functions reflects the underlying face centered cubic structure. 96

Figure 6.7: Visualization of the control mechanism of physical quantities. In this example, three sections are defined. Each red diamond represents a line in the descriptive section of the parameter file. Within each section, the number of complete snapshots can be controlled by the values of `nroffld`. The values between two diamonds are interpolated by `FMD`. 98

Figure 6.8: Flow diagram of the simulation core of FMD 101

Figure 6.9: Graphical User Interface for the post-processing library. GeoToolbox is capable of reading XYZ files. It displays the number of snapshots of the specified file. The radial distribution function and potential energies of the according snapshots can be calculated easily. Moreover, an automated plane-detection was implemented. Starting from the center atom and two other neighbors of the center atom, the tool tries to find a crystal structure within the given assembly of atoms. A Voronoi tesselation is performed to get the neighborhood of each atom.
If the structure could be determined by finding individual crystal planes, the normal vector of these planes can be used to transform this normal vector to point to the z-direction. Finally, in case of a structure with a faulty stacking order (fcc and hcp), GeoToolbox can identify individual planes as fcc planes or hcp planes, depending on their neighboring planes. 102

LIST OF TABLES

Table 3.1: Equilibrium lattice constants for various elements in different crystal structures. The potentials used for these calculations are given in section 6.2.2. The values used for fitting are well reproduced. 40

Table 3.2: Experimental and simulated linear thermal expansion coefficient for Nickel 42

Table 3.3: Simulated and experimental bulk moduli for various elements (potentials taken from [38]). The second value for Ni* was calculated using the proposed potential by Daw and Baskes and exhibits a strong deviation as compared to experimental values. 44

Table 3.4: Comparison between simulated sublimation energies and experimental results (potentials taken from [38]). Ni* denotes an alternative potential (cp. Tab. 3.3). 45

Table 3.5: Comparison of the experimental value of the heat capacity C_P for Nickel with the results obtained from different published embedded atom method potentials (cp. section 6.2) 46

Table 3.6: Comparison between experimental equilibrium lattice constants and simulation results for $Fe_{50}Pt_{50}$. The value indicating the tetragonality for the fct phase agrees well with experiments... 48

Table 3.7: Sublimation energies for Fe and Pt in a fcc disordered alloy and a fct configuration. Although Fe exhibits a lower sublimation energy in the disordered phase, the mean sublimation energy per atom in the fct phase is lower compared to the fcc phase. 49

Table 6.1: Effective charge function for Nickel. The function is given as a set of spline knots. Here, a clamped spline function is used (i.e. the first derivative of the function is specified). The first values (second row) refer to Daw and Baskes [28], the second set (fifth row) refer to Ref. [103]. 91

Table 6.2: Embedding function $F_{\mathrm{Ni}}()$. Again, the function is given as a set of spline knots. Contrary to the effective charge function, the spline given below is a natural spline with vanishing second derivatives at the first and the last knot. Values larger than Å^{-3} result in a linear extrapolation of the last gradient at this value. 92

Table 6.3: Parameters to calculate the electronic density of Nickel (taken from [28] and [16]). 93

Table 6.4: Potential parameters of selected elements. Parameters of the same form for Cu, Pd, Al, Pb, Mo, Ta, W, Mg, Ti and Zr can be found in Ref. [39]. 94

REFERENCES

[1] D.M. Weller, A. Folks, L. Best, M. E. Best, W. Lee, M.F. Toney, M. Schwickert, J.U. Thiele, M.F. Doerner, "High K_u materials approach to 100 Gbits/in^2", IEEE Transactions on Magnetics 36 (1), 10-15 (2000).

[2] T.J. Klemmer, N. Shukla, C. Liu, X.W. Wu, E.B. Svedberg, O. Mryasov, R.W. Chantrell, D. Weller, M. Tanase, and D.E. Laughlin, "Structural studies of $L1_0$ FePt nanoparticles", Appl. Phys. Lett. 81 (12), 2220-2222 (2002).

[3] D. Weller and T. McDaniel, "Media for extremely high density recording", in Advanced Magnetic Nanostructures, David Sellmyer, Ralph Skomski (eds), Springer, pp 295-324 (2006).

[4] D.L. Lesite-Pelecky, V. Labhasetwar, and R. H. Kraus Jr, "Nanobiomagnetics", in Advanced Magnetic Nanostructures, David Sellmyer, Ralph Skomski (eds), Springer, pp 461-490 (2006).

[5] ParaDyn - Embedded Atom Method Molecular Dynamics,
http://www.cs.sandia.gov/~sjplimp/download.html#pd - last visit Oct. 22nd, 2006.

[6] OOPSE - The Object-Orientated Parallel Simulation Engine
http://www.oopse.org - last visit Oct. 22nd, 2006.

[7] MOLDY - A general purpose molecular dynamics simulation program
http://www.earth.ox.ac.uk/~keithr/moldy.html, last visit Oct. 22nd, 2006.

[8] H.N.G. Wadley, X. Zhou, and R.A. Johnson, "Atomic Assembly of Giant Magnetoresistive Multilayers", Materials Research Society Symposium Proceedings Series 672, O4.1.1-O4.1.14 (2001).

[9] O.N. Mryasov, U. Nowak, K.Y. Guslienko, and R.W. Chantrell, "Temperature-dependent magnetic properties of FePt: Effective spin Hamiltonian model", Europhys. Lett. 69 (5), 805-811 (2005).

[10] U. Nowak, O.N. Mryasov, R. Wieser, K. Guslienko, and R.W. Chantrell, "Spin dynamics of magnetic nanoparticles: Beyond Brown's theory", Physical Review B, 72 (17), 172410 (2005).

[11] F. Dorfbauer, R. Evans, M. Kirschner, O. Chubykalo-Fesenko, R.W. Chantrell, and T. Schrefl, "Effects of Surface Anisotropy on the energy barrier in Cobalt-Silver Core-Shell nanoparticles", accepted for publication in J. Mag. Mag. Mat., (2006).

[12] B.J. Alder and T.E. Wainwright, "Phase Transition for a Hard Sphere System", J. Chem. Phys., 27 (5), 1208f (1957).

[13] A. Rahman, "Correlations in the Motion of Atoms in Liquid Argon", Phys. Rev. 136 (2A), A405 LP - A411 (1964).

[14] L. Verlet, "Computer "Experiments" on Classical Fluids. I. Thermodynamical Properties of Lennard-Jones Molecules", Phys. Rev. 159 (1), 98 LP - 103 (1967).

[15] R.D. Skeel, G. Zhang, and T. Schlick, "A Family of Symplectic Integrators: Stability, Accuracy, and Molecular Dynamics Applications", SIAM J. Sci. Comput. 18, 203-222 (1997).

[16] M.P. Allen and D.J. Tildesley, "Computer Simulation of Liquids", Claredon, Oxford, (1987).

[17] D. Frenkel and B. Smit, "Understanding Molecular Simulation - From Algorithms to Applications", Academic Press, (1996).

[18] M. Griebel, S. Knapek, G. Zumbusch, and A. Caglar, "Numerische Simulation in der Moleküldynamik", Springer Verlag, (2003).

[19] F. Ercolessi, "A molecular dynamics primer", http://www.ud.infn.it/~ercolessi/md/md.pdf - last visit Aug. 23rd, 2006.

[20] H.J.C. Berendsen, J.P.M. Postma, W.F. van Gunsteren, A. DiNola, and J.R. Haak, "Molecular dynamics with coupling to an external bath", J. Chem. Phys. 81 (8), 3684-3690 (1984).

[21] S. Nosé, "A unified formulation of the constant temperature molecular dynamics methods", J. Chem. Phys. 81 (1), 511-519 (1984).

[22] S.D. Bond, B.J. Leimkuhler, and B.B. Laird, "The Nosé-Poincaré Method for Constant Temperature Molecular Dynamics", Journal of Computational Physics 151, 114-134 (1999).

[23] W.G. Hoover, "Canonical dynamics: Equilibrium phase-space distributions", Phys. Rev. A J1 - PRA 31 (3), 1695 LP - 1697 (1985).

[24] B.L. Holian, A.J. De Groot, W.G. Hoover, and C.G. Hoover, "Time-reversible equilibrium and nonequilibrium isothermal-isobaric simulations with centered-difference Stoermer algorithms", Phys. Rev. A J1 - PRA 41 (8), 4552 LP - 4553 (1990).

[25] S. Jang and G.A. Voth, "Simple reversible molecular dynamics algorithms for Nosé-Hoover chain dynamics", J. Chem. Phys. 107 (22), 9514-9526 (1997).

[26] S. Nosé, "An Improved Symplectic Integrator for Nosé-Poincaré Thermostat", Journal of the Physical Society of Japan 70 (1), 75-77 (2001).

[27] D.J. Leimkuhler and C.R. Sweet, "The Canonical Ensemble via Symplectic Integrators using Nosé and Nosé-Poincaré chains", Journal of Chemical Physics 121 (1), 108-116 (2004).

[28] J.E. Lennard-Jones, "Cohesion", Proceedings of the Physical Society 43 (5), 461-482 (1931).

[29] F. Ercolessi, M. Parinello, and E. Tosatti, "Simulation of gold in the glue model", Phil. Mag. A 58, (213-226) (1988).

[30] M.S. Daw and M.I. Baskes, "Embedded-atom method: Derivation and application to impurities, surfaces, and other defects in metals", Phys. Rev. B 29, 6443-6453 (1984).

[31] M.S. Daw and M.I. Baskes, "Semiempirical, Quantum Mechanical Calculation of Hydrogen Embrittlement in Metals", Phys. Rev. Lett. 50, 1285-1288 (1983).

[32] M.J. Stott and E. Zaremba, "Quasiatoms: An approach to atoms in nonuniform electronic systems", Phys. Rev. B 22, 1564-1583 (1980).

[33] H.N.G. Wadley, X.W. Zhou, R.A. Johnson, M. Neurock, "Mechanisms, models and methods of vapor deposition", Prog. Mat. Sci 46, 329-377 (2001).

[34] R.A. Johnson, "Analytic Nearest-Neighbor Model for Fcc Metals", Physical Review B 37 (8), 3924-3931 (1988).

[35] G. Grochola, S. Russo, I.K. Snook, I. Yarovsky, "The Embedded Atom Method for Prediction of Properties of Metals and Alloys", The Broken Hill Proprietary Company Ltd., BHPR/R/1999/006.

[36] A.A. Abrahamson, "Repulsive Interaction Potentials between Rare-Gas Atoms. Heteronuclear Two-Center Systems", Physical Review 133 (4A), A990 LP - A1004 (1964).

[37] A.A. Abrahamson, "Born-Mayer-Type Interatomic Potential for Neutral Ground-State Atoms with Z=2 to Z=105", Physical Review 178 (1), 76 LP - 79 (1969).

[38] R.R. Zope and Y. Mishin, "Interatomic potentials for atomistic simulations of the Ti-Al system", Phys. Rev. B 68, 24102 (2003).

[39] R.A. Johnson, "Alloy models with the embedded-atom method", Phys. Rev. B 39, 12554 (1989).

[40] X.W. Zhou and H.N.G. Wadley, "Atomistic simulation of AlOx magnetic tunnel junction growth", Phys. Rev. B 71, 054418 (2005).

[41] X.W. Zhou, H.N.G. Wadley, R.A. Johnson, D.J. Larson, N. Tabat, A. Cerezo, A.K. Petford-Long, G.D.W. Smith, P.H. Clifton, R.L. Martens, and T.F. Kelly, "Atomic scale structure of sputtered metal multilayers", Acta Mater 49 (19), 4005-4015 (2001).

[42] W. Zou, H.N.G. Wadley, X.W. Zhou, R.A. Johnson, and D. Brownell, "Surfactant-mediated growth of giant magnetoresistance multilayers", Physical Review B 64 (17), 174418 (2001).

[43] J.R. Morris and K.M. Ho, "Calculating Accurate Free Energies of Solids Directly from Simulations", Physical Review Letters 74 (6), 940 - 943 (1995).

[44] S.M. Foiles and J.B. Adams, "Thermodynamic properties of fcc transition metals as calculated with the embedded-atom method", Phys. Rev. B 40, 5909 (1989).

[45] M.S. Daw and R.D. Hatcher, "Application of the embedded atom method to phonons in transition metals", Solid State Communications 56 (8), 697-699 (1985).

[46] http://cst-www.nrl.navy.mil/lattice/ - last visit: Aug. 28th, 2006.

[47] M.I. Aroyo, J.M. Perez-Mato, C. Capillas, E. Kroumova, S. Ivantchev, G. Madariaga, A. Kirov, and H. Wondratschek. "Bilbao Crystallographic Server I: Databases and crystallographic computing programs". Zeitschrift für Kristallographie, 221 (1), 15-27 (2006).

[48] P. Villars and L.D. Calvert, "Pearson's Handbook of Crystallographic Data for Intermetallic Phases", 2nd Edition, ASM International, Materials Park, Ohio, (1991).

[49] F.C. Nix and D. MacNair, "The Thermal Expansion of Pure Metals: Copper, Gold, Aluminum, Nickel, and Iron", Physical Review 60 (8), 597 LP - 605 (1941).

[50] http://en.wikipedia.org/wiki/Birch-Murnaghan_equation_of_state/
last visit: Aug. 28th, 2006.

[51] E. Ziambaras and E. Schröder, "Theory for structure and bulk modulus determination", Phys. Rev. B 68, 064112 (2003).

[52] S.H. Whang, Q. Feng, and Y.Q. Gao, "Ordering, deformation and microstructure in $L1_0$ type FePt", Acta Mater. 46 (18), 6485-6495 (1998).

[53] S. Sun, C. Murray, D. Weller, L. Folks, and A. Moser, "Monodisperse FePt Nanoparticles and Ferromagnetic FePt Nanocrystal Superlattices", Science 287 (5460), 1989-1992 (2000).

[54] Y.K. Takahashi, T. Ohkubo, M. Ohnuma, and K. Hono, "Size effect on the ordering of FePt granular films", Journal of Applied Physics 93 (10), 7166-7168 (2003).

[55] S. Stappert, "FePt-Nanopartikel aus der Gasphase: Herstellung, Struktur und Magnetismus", Dissertation, Universität Duisburg/Essen (2003).

[56] Q. Sun, A.K. Kandalam, Q. Wang, P. Jena, Y. Kawazoe, and M. Marquez, "Effect of Au coating on the magnetic and structural properties of Fe nanoclusters for use in biomedical applications: A density-functional theory study", Phys. Rev. B 73, 134409 (2006).

[57] E.E. Carpenter, "Iron nanoparticles as potential magnetic carriers", Journal of Magnetism and Magnetic Materials 225 (1-2), 17-20 (2001).

[58] W.L. Zhou, E.E. Carpenter, J. Lin, A. Kumbhar, J. Sims, and C.J. O'Connor, "Nanostructures of gold coated iron core-shell nanoparticles and the nanobands assembled under magnetic field", The European Physical Journal D - Atomic, Molecular, Optical and Plasma Physics 16 (1), 289-292 (2001).

[59] S.M. Foiles, "Application of the Embedded-Atom Method to Liquid Transition-Metals", Physical Review B 32 (6), 3409-3415 (1985).

[60] W. Humphrey, A. Dalke, K. Schulten, "VMD - Visual Molecular Dynamics", J. Molec. Graphics, 14.1, 33-38 (1996).

[61] MDL® Chime - http://www.mdl.com/products/framework/chime/
last visit: Sept. 14th, 2005.

[62] MicroAVS®, an evaluation copy can be obtained from:
http://www.kgt.co.jp/feature/microavs/ - last visit Sept. 15th, 2005.

[63] F. Dorfbauer, "Micromagnetic Simulations of Exchange Biased Bilayers", Diploma thesis, Institute for Solid State Physics, Vienna University of Technology, (2004).

[64] G. Grochola, S.P. Russo, and I.K. Snook, "On fitting a gold embedded atom method potential using the force matching method", J. Chem. Phys. 123 (20), 204719-204717 (2005).
A description of the potential file format can be found on the Journal's web-server:
http://ftp.aip.org/epaps/journ_chem_phys/E-JCPSA6-123-707542/

[65] C.B. Barber, D.P. Dobkin, H.T. Huhdanpaa, "The Quickhull algorithm for convex hulls," ACM Trans. on Mathematical Software, 22(4):469-483, (1996).
http://www.qhull.org/ - last visit: Sept. 14th, 2005.

[66] B. O´Malley, "Crystallization in the Hard Sphere System", PhD thesis, Department of Applied Physics, Royal Melbourne Institute of Technology, (2001).

[67] B. O'Malley and I.K. Snook, "Crystal Nucleation in the Hard Sphere System", Physical Review Letters 90 (8), 085702-085704 (2003).

[68] V. Dupuis, L. Favre, S. Stanescu, J. Tuaillon-Combes, E. Bernstein, and A. Perez, "Magnetic assembled nanostructures from pure and mixed Co-based clusters", Journal of Physics: Condensed Matter 16, S2231-S2240 (2004).

[69] M. Jamet, V. Dupuis, P. Mélinon, G. Guiraud, A. Pérez, W. Wernsdorfer, A. Traverse, and B. Baguenard, "Structure and magnetism of well defined cobalt nanoparticles embedded in a niobium matrix", Physical Review B 62 (1), 493 LP - 499 (2000).

[70] M. Jamet, W. Wernsdorfer, C. Thirion, D. Mailly, V. Dupuis, P. Mélinon, and A. Pérez, "Magnetic Anisotropy of a Single Cobalt Nanocluster", Phys. Rev. Lett. 86, 4676-4679 (2001).

[71] J.L. Rousset, F.J. Cadete Santos Aires, B.R. Sekhar, P. Mélinon, B. Prevel, and M. Pellarin, "Comparative X-ray Photoemission Spectroscopy Study of Au, Ni, and AuNi Clusters Produced by Laser Vaporization of Bulk Metals", Journal of Physical Chemistry B 104, 5430 (2000).

[72] B. Lu, T. Klemmer, K. Wierman, G. Ju, D. Weller, A.G. Roy, D.E. Laughlin, C. Chang, and R. Ranjan, "Study of stacking faults in Co-alloy perpendicular media", Journal of Applied Physics 91 (10), 8025-8027 (2002).

[73] K.W. Wierman, T.J. Klemmer, B. Lu, G. Ju, K.J. Howard, A.G. Roy, and D.E. Laughlin, "Ru_xCr_{1-x}/Ta underlayer for Co-alloy perpendicular magnetic recording", Journal of Applied Physics 91 (10), 8031-8033 (2002).

[74] T. Klemmer, B. Lu, G. Ju, O. Mryasoc, R. Chantrell, "Stacking faults in perpendicular media; The relationsship to anisotropy dispersion", Conference contribution, private communication with R. Chantrell (2006).

[75] G. Wulff, "Zur Frage der Geschwindigkeit des Wachstums und der Auflösung von Krystallflächen", Zeitschrift für Krystallographie und Mineralogie, 34, 449-530 (1901).

[76] C. Herring, "Some Theorems on the Free Energies of Crystal Surfaces", Physical Review 82 (1), 87 LP - 93 (1951).

[77] S. Ino, "Epitaxial Growth of Metals on Rocksalt Faces Cleaved in Vacuum. II. Orientation and Structure of Gold Particles Formed in Ultrahigh Vacuum", J. Phys. Soc. Jap. 21, 346-362 (1966).

[78] S. Ino and S. Ogawa, "Multiply Twinned Particles at Earlier Stages of Gold Film Formation on Alkalihalide Crystals", J. Phys. Soc. Jap. 22, 1365-1374 (1967).

[79] P. Mohn, "Magnetism in the Solid State, An Introduction.", Springer Verlag, (2002).

[80] M. Kirschner, "Exchange Bias in Ferro-/Antiferromagnetic Bilayers", Diploma Thesis, Institute for Solid State Physics, Vienna University of Technology, (2003).

[81] G. Bertotti, "Hysteresis in Magnetism", Academic Press Series in Electromagnetism, (1998).

[82] P. Bruno, V. Drchal, J. Kudrnovský, M. Pajda, and I. Turek, "Ab initio calculations of exchange interactions, spin-wave stiffness constants, and Curie temperatures of Fe, Co, and Ni", Physical Review B 64 (17), 174402 (2001).

[83] H. Kronmüller and M. Fähnle, "Micromagnetism and the Microstructure of Ferromagnetic Solids", Cambridge University Press, (2003).

[84] W. F. Brown, Jr., "Thermal Fluctuations of a Single-Domain Particle", Phys. Rev. 130, 1677-1686, (1963).

[85] W.T. Coffey, Yu. P. Kalmykov, J.T. Waldron, "The Langevin Equation", Singapore: World Scientific Publishing, (1996).

[86] M. Kirschner, "Coarse-graining in Micromagnetics", PhD thesis, Institute for Solid State Physics, Vienna University of Technology, (2006).

[87] W. Scholz, "Micromagnetic Simulation of Thermally Activated Switching in Fine Particles", Diploma Thesis, Institute for Solid State Physics, Vienna University of Technology, (1999).

[88] F. Dorfbauer, T. Schrefl, M. Kirschner, G. Hrkac, D. Suess, O. Ertl, and J. Fidler, "Nanostructure calculation of CoAg core-shell clusters", Journal of Applied Physics 99, 08G706 (2006).

[89] L. Neél, J. Phys Radium 15, 376, (1954).

[90] D. Garanin and H. Kachkachi, "Surface Contribution to the Anisotropy of Magnetic Nanoparticles", Phys. Rev. Lett. 90, 065504, (2003).

[91] S.D. Cohen and A.C. Hindmarsh, "CVODE, A Stiff/Nonstiff ODE Solver in C", Computers in Physics, 10(2), 1996, pp 138-143 (1995).

[92] J.P. Chen, C.M. Sorensen, K.J. Klabunde, and G.C. Hadjipanayis, "Magnetic properties of nanophase cobalt particles synthesized in inversed micelles", Journal of Applied Physics 76 (10), 6316-6318 (1994).

[93] K. Zhang and D.R. Fredkin, "Surface anisotropy of a fine γ-Fe_2O_3 particle", J. Appl. Phys. 79 (8), 5762 (1996).

[94] K. Zhang and D.R. Fredkin, "Effects of partial surface anisotropy on a fine magnetic particle", J. Appl. Phys. 85, 6187 (1999).

[95] http://physics.nist.gov/constants/ - last visit: Sept. 20th, 2005.

[96] private communication with M. Kirschner.

[97] X.W. Zhou, R.A. Johnson, and H.N.G. Wadley, "Misfit-energy-increasing dislocations in vapor-deposited CoFe/NiFe multilayers", Physical Review B 69 (14), (2004).

[98] W.H. Press, S.A. Teukolsky, W.T. Vetterling and B.P. Flannery, "Numerical Recipes in C - The Art of Scientific Computing", Second Edition, Cambridge University Press, (2004).

[99] http://www.arndt-bruenner.de/mathe/scripts/kubspline.htm#rechner/
last visit Aug. 15th, 2006.

[100] XMGrace is available for various operating systems at:
http://plasma-gate.weizmann.ac.il/Grace/ - last visit Aug. 15th, 2006.

[101] E. Clementi and C. Roetti, "Roothaan-Hartree-Fock Atomic Wavefunctions: Basis Functions and Their Coefficients for Ground and Certain Excited States of Neutral and Ionized Atoms, Z <= 54", Atomic Data and Nuclear Data Tables", Vol. 14, 177 (1974).

[102] S.M. Foiles, M.I. Baskes, and M.S. Daw, "Embedded-atom-method functions for the fcc metals Cu, Ag, Au, Ni, Pd, Pt, and their alloys", Phys. Rev. B 33 (12), 7983 (1986).

[103] K. Kadau, "Molekulardynamik-Simulationen von strukturellen Phasenumwandlungen in Festkörpern, Nanopartikeln und ultradünnen Filmen", Dissertation, Universität Duisburg, Fachbereich Physik - Technologie (2001).

[104] R. Meyer and P. Entel, "Martensite-austenite transition and phonon dispersion curves of $Fe_{1-x}Ni_x$ studied by molecular-dynamics simulations", Phys. Rev. B. 57 (1998).

PRESENTATIONS AND PUBLICATIONS

10.1 Publications

[1] F. Dorfbauer, T. Schrefl, M. Kirschner, G. Hrkac, D. Suess, O. Ertl, and J. Fidler, "Nanostructure calculation of CoAg core-shell clusters", Journal of Applied Physics 99, 08G706, (2006).

[2] F. Dorfbauer, R. Evans, M. Kirschner, O. Chubykalo-Fesenko, R.W. Chantrell, and T. Schrefl, "Effects of Surface Anisotropy on the energy barrier in Cobalt-Silver Core-Shell nanoparticles", accepted for publication in J. Mag. Mat. Mag., (2006).

[3] R. Evans, U. Nowak, F. Dorfbauer, T. Schrefl, O. Mryasov, R.W. Chantrell, and G. Grochola, "The influence of Shape and Structure on the Curie temperature of Fe and Co nanoparticles", Journal of Applied Physics 99, 08G703, (2006).

[4] M. Kirschner, T. Schrefl, G. Hrkac, F. Dorfbauer, D. Suess, and J. Fidler, "Relaxation times and cell size in nonzero-temperature micromagnetics", Physics B: condensed Matter 372, 277-281, (2006).

[5] O. Ertl, G. Hrkac, D. Suess, M. Kirschner, F. Dorfbauer, J. Fidler, and T. Schrefl, "Multiscale micromagnetic simulation of GMR read heads", J. Applied Phys., 99 08S303, (2006).

[6] G. Hrkac, M. Kirschner, F. Dorfbauer, D. Suess, O. Ertl, and J. Fidler, "Influence of eddy currents on the effective damping parameter", J. Appl. Phys. 99, 08B902, (2006).

[7] D. Suess, K. Porath, T. Schrefl, F. Dorfbauer, M. Kirschner, and J. Fidler, "Lateral Exchange Spring Media", IEEE Trans. Magn., (2006) in press.

[8] D. Suess, T. Schrefl, R. Dittrich, M. Kirschner, F. Dorfbauer, G. Hrkac, and J. Fidler, "Exchange spring recording media for areal densities up to 10 Tbit/in^2", Journal of Magnetism and Magnetic Materials, vol. 290, 551-554 (2005).

[9] D. Suess, T. Schrefl, S. Fahler, M. Kirschner, G. Hrkac, F. Dorfbauer, and J. Fidler, "Exchange spring media for perpendicular recording", Applied Physics Letters, 87, Art. No. 012504, (2005).

[10] G. Hrkac, M. Kirschner, F. Dorfbauer, D. Suess, O. Ertl, J. Fidler, and T. Schrefl, "Three-dimensional micromagnetic finite element simulations including eddy currents,", Journal of Applied Physics, vol. 97, Art. No. 10E311, (2005).

[11] M. Kirschner, T. Schrefl, F. Dorfbauer, G. Hrkac, S. Suess, and J. Fidler, "Cell size corrections for nonzero-temperature micromagnetics", Journal of Applied Physics, vol. 97, Art. No. 10E301, (2005).

[12] F. Dorfbauer, T. Schrefl, D. Suess, M. Kirschner, G. Hrkac, and J. Fidler, "Pulsed inductive microwave magnetometer response calculated for IrMn/FeNi bilayers", European Physical Journal B, vol. 45, 267-271, (2005).

[13] F. Dorfbauer, D. Suess, J. McCord, M. Kirschner, T. Schrefl, and J. Fidler, "Micromagnetic simulation of asymmetric magnetization reversal in exchange biased bilayers", Journal of Magnetism and Magnetic Materials, vol. 290, pp. 754-757, (2005).

[14] R. Dittrich, T. Schrefl, M. Kirschner, D. Suess, G. Hrkac, F. Dorfbauer, O. Ertl, and J. Fidler, "Thermally induced vortex nucleation in permalloy elements", IEEE Transactions on Magnetics, vol. 41, 3592-3594, (2005).

[15] D. Suess, T. Schrefl, M. Kirschner, G. Hrkac, F. Dorfbauer, O. Ertl, and J. Fidler, "Optimization of exchange spring perpendicular recording media", IEEE Transactions on Magnetics, vol. 41, 3166-3168, (2005).

[16] G. Hrkac, T. Schrefl, O. Ertl, D. Suess, M. Kirschner, F. Dorfbauer, and J. Fidler, "Influence of eddy current on magnetization processes in submicrometer permalloy structures", IEEE Transactions on Magnetics, vol. 41, 3097-3099 (2005).

[17] T. Schrefl, M.E. Schabes, D. Suess, O. Ertl, M. Kirschner, F. Dorfbauer, G. Hrkac, and J. Fidler, "Partitioning of the perpendicular write field into head and SUL contributions", IEEE Transactions on Magnetics, vol. 41, 3064-3066 (2005).

[18] R. Evans, F. Dorfbauer, O. Mryasov, O. Chubykalo-Fesenko, T. Schrefl, and R.W. Chantrell, "The Effects of Surface Coating on the Structural and Magnetic Properties of CoAg Core-Shell Nanoparticles", submitted to J. Appl. Phys. (2006).

10.2 Talks

[1] F. Dorfbauer (invited), "Magnetic Modeling of Nanoparticles", University of Konstanz, Germany, November 9th, 2006.

[2] F. Dorfbauer, "Molecular Dynamics Simulations using the Embedded Atom Method", University of York, UK, January 25th, 2006.

[3] F. Dorfbauer, "Nanostructure Calculation of CoAg core-shell clusters", 50th Annual Conference on Magnetism and Magnetic Materials, San Jose CA, USA, November 1st, 2005.

[4] F. Dorfbauer, "Micromagnetic Simulation of Asymmetric Magnetization Reversal in Exchange Biased Bilayers", Joint European Magnetic Symposia, Dresden/Germany, September 5-10, 2004.

[5] F. Dorfbauer, "Pulsed Inductive Microwave Magnetometer Response calculated for IrMn/FeNi bilayers", Ultrabias Summer School 2004, Anglet/France, September 12-16, 2004.

[6] F. Dorfbauer, "Eigenschaften von anti- und ferromagnetischen dünnen Schichten in GMR-Leseköpfen moderner Festplatten", TU Dresden, January 27, 2004.

[7] F. Dorfbauer, "Micromagnetic Simulations of exchange biased bilayers, Royal Melbourne Institute of Technology", July 15, 2004.

[8] F. Dorfbauer und M. Kirschner, "Vom Magnetkompass zum Terrabitspeicher - Simulation magnetischer Datenspeicherung", Scienceweek, Wien, Mai 2004.

10.3 Selected Poster Presentations

[1] F. Dorfbauer, R. Evans, M. Kirschner, O. Chubykalo-Fesenko, R.W. Chantrell, and T. Schrefl, "Effects of Surface Anisotropy on the energy barrier in Cobalt-Silver Core-Shell nanoparticles", Joint European Magnetic Symposia, Donostia - San Sebastian, Spain, June 2006.

[2] F. Dorfbauer, M. Kirschner, T. Schrefl, D. Suess, G. Hrkac, O. Ertl, and J. Fidler, "Analysis of Partially Disordered Nanoparticles", Nanomagnetism and Spintronics - Spring School, Cargese, Corsica, June 2005.

[3] F. Dorfbauer, M. Kirschner, D. Suess, T. Schrefl, J. Fidler, and J.N. Chapman, "Micromagnetic calculations of exchange biased IrMn/NiFe bilayers", Ultrabias Summer School 2004, Anglet/France, September 12-16, 2004.

[4] M. Kirschner, F. Dorfbauer, G. Hrkac, O. Ertl, P. Speckmayr, T. Schrefl, and D. Suess, "Vom Magnetkompass zum Terrabitspeicher - Simulation magnetischer Datenspeicherung", Scienceweek, Wien, 8.-16. Mai 2004.

[5] M. Schmid, G. Kresse, F. Dorfbauer, D. Payer, V. Bus, J. Redinger, and P. Varga, "When reactive metals become noble: site-selective adsorption of CO on alloys", Symp. on Surface Science 2004 (3S-04), St. Christoph, 2004.

[6] M. Schmid, D. Payer, F. Dorfbauer, G. Kresse, and P. Varga, "CO-Adsorption auf Legierungsoberflächen - oder: sind Co, Fe und Cr Edelmetalle?", ÖPG-Haupttagung Leoben, 2002.

CURRICULUM VITAE

Florian Dorfbauer
Gentzgasse 72/2/14
1180 Wien
Tel.: ++43 650 25 633 25
E-Mail: Florian.Dorfbauer@aon.at

Personal

Date of birth	April 7th, 1977
Place of birth	Steyr, Austria
Nationality	Austria

Education

Since Summer 2004	PhD in Computational Physics
2001-2004	Study of Physics at the Vienna University of Technology Graduated with excellence.
1998-2001	Study of Physics at the University of Linz
1991-1996	HTL Steyr, High school focussed on electronics and informatics. Graduated with excellence.
1983-1991	Elementary School in Perg

Research Visits

May 2006	University of York, UK Research visit at Prof. R. Chantrell's group
January 2006	University of York, UK Collaboration with R. Evans and Prof. R. Chantrell
July - December 2004	Royal Melbourne Institute of Technology / Australia Research visit at the group of Prof. Ian Snook
February 2004	Institut für Festkörperphysik und Werkstoffkunde / Dresden Research visit at the group of Dr. R. Schäfer

Professional Experience

Since 2005	Freelance employment as solution provider in the field of data security and autonomous backup-servers for SMBs.
Since 2001	Freelance employment for various artists in the area of sound recording, mixing, mastering and production.
2001-2004	DICE Danube Integrated Circuit Engineering / Linz, a subdivision of Infineon AG, Software development
2000-2003	Rudolf Luger Professional Audio Systems / Bad Zell Freelance work as front-of-house sound engineer
Summer 2000	Steyr Daimler Puch R&D Audio Engineering Center / Steyr software development; internship
1999-2001	ACP - All Computer Products / Linz Gathered experience in computer network maintenance
1998-1999	Conducted the EU-supported youth project 'Grenzgänge'
Since 1997	Kulturinitiative Sound-Haufen / Perg Chairman of a non-profit organisation dealing with the technical support for young musicians mainly.
1997-1998	Monte Video Filmproduktion / Linz Worked as assistant cameraman and assistant executive producer.
1996-1997	Civil service at the Austrian Red Cross
Summer 1996	Katholische Arbeiterjugend / Graz database development
1991-1996	Synthesa Chemie and Elektro Ebner / Perg Various internships at local companies in Upper Austria

Software Experience and Programming Skills

C, C++, Assembler, MS Office, Adobe Products, Steinberg Products, Linux, Java, HTML, PHP, SQL, VVVV, 3D Studio MAX